

City Research Online

City St George's, University of London

Citation: Talboys, E. (2021). On the aerodynamic and aeroacoustic effect of passive trailing edge flaplets. (Unpublished Doctoral thesis, City, University of London)

This is the accepted version of the paper.

This version of the publication may differ from the final published version. To cite this item please consult the publisher's version.

Permanent repository link: https://openaccess.city.ac.uk/id/eprint/27145/

Copyright and Reuse: Copyright and Moral Rights remain with the author(s) and/or copyright holders. Copies of full items can be used for personal research or study, educational, or not-for-profit purposes without prior permission or charge, unless otherwise indicated, provided that the authors, title and full bibliographic details are credited, a hyperlink and/or URL is given for the original metadata page and the content is not changed in any way. For full details of reuse please refer to City Research Online policy.

City Research Online: http://openaccess.city.ac.uk/ publications@citystgeorges.ac.uk

On the aerodynamic and aeroacoustic effect of passive trailing edge flaplets.



Edward Talboys

School of Mathematics, Computer Science & Engineering

City, University of London

Submitted in part fulfilment of the degree of

Doctor of Philosophy

22nd November 2021

Contents

List of Figures vii

List of Tables xiii

Acknowledgements xv

Declaration xvii

Summary xix

Nomenclature xxi

Acronyms xxv

1 Introduction 1

1.1 Introduction . . . 1
1.1.1 Aerofoil self-noise mechanisms . . . 5
1.1.1.1 Turbulent boundary layer noise. . . . 5
1.1.1.2 Laminar boundary layer noise. . . . 5
1.1.1.3 Separation noise. . . . 6
1.1.1.4 Trailing edge bluntness noise. . . . 6
1.1.1.5 Tip vortex noise. . . . 6
1.2 Thesis structure . . . 6

2 Paper 1: Upstream shear-layer stabilisation via self-oscillating trailing edge flaplets 9

2.1 Introduction . . . 10
2.2 Experimental Set-Up . . . 12
2.2.1 Velocity Field Measurements . . . 14
2.2.2 Flap Motion Tracking . . . 15
2.3 Results . . . 15
2.3.1 Flaplet response to step input . . . 15
2.3.2 Flow Field . . . 17

2.3.3 Flaplet Motion . . . 25
2.4 Conclusion . . . 27
2.5 Critical analysis . . . 28
2.5.1 Overview and study contributions . . . 28
2.5.2 Limitations of the working hypothesis . . . 29
2.5.3 Other aerofoil profiles . . . 30
2.5.4 Mechanical coupling of flaplets . . . 30
2.5.5 Tracking of flaplets . . . 32
2.5.6 Chordwise sensitivity . . . 33
2.5.7 Uncertainty of the High-Speed PIV measurements . . . 34
2.5.8 Future work . . . 35
2.5.8.1 Piezoelectric flaplets . . . 35
2.5.8.2 Additional measurements . . . 36

3 Paper 2: An aeroacoustic investigation into the effect of self-oscillating trailing edge flaplets 39

3.1 Introduction . . . 40
3.2 Experimental Arrangement . . . 43
3.3 Results . . . 47
3.3.1 Theoretical Comparison . . . 47
3.3.2 Single Microphone Measurements . . . 49
3.3.3 Linear stability analysis . . . 52
3.3.4 Overall sound pressure level measurements . . . 54
3.3.5 Aerodynamic force measurements . . . 56
3.3.6 Hot wire anemometry . . . 57
3.4 Conclusion . . . 60
3.5 Critical analysis . . . 61
3.5.1 Overview and study contributions . . . 61
3.5.2 Open jet considerations . . . 62
3.5.3 Calibration of measurement systems . . . 63
3.5.3.1 Microphone array . . . 63
3.5.3.2 Hot wire anemometery . . . 64
3.5.3.3 Force balance . . . 66
3.5.4 Simulation for lift and drag coefficients . . . 67
3.5.5 Background noise . . . 68
3.5.6 N-factor sensitivity . . . 69
3.5.7 Separation bubble prediction . . . 70
3.5.8 Future work . . . 70

4 Paper 3: A parametric study of the effect of self-oscillating trailing-edge flaplets on aerofoil self-noise **73**

4.1 Introduction . . . 74
4.2 Experimental Arrangement and Measurement Techniques . . . 79
4.2.1 Wind Tunnel . . . 79
4.2.2 Aerofoil . . . 80
4.2.3 Acoustic Measurements . . . 80
4.2.4 Constant Temperature Anemometry . . . 81
4.2.5 Laser Displacement Measurements . . . 82
4.3 Results . . . 82
4.3.1 Static Flaplet Response . . . 82
4.3.2 Tonal Noise . . . 84
4.3.3 Acoustic, Hot Wire Anemometry and Vibration Results . . . 87
4.3.3.1 Variation in Flaplet Length . . . 88
4.3.3.2 Variation in Flaplet Width . . . 100
4.3.3.3 Variation in Flaplet Inter-Spacing . . . 108
4.4 Conclusion . . . 114
4.5 Critical analysis . . . 117
4.5.1 Overview and study contributions . . . 117
4.5.2 Model Vibration . . . 117
4.5.3 Beamforming Considerations . . . 120
4.5.3.1 Beamforming models . . . 120
4.5.3.2 DAMAS considerations . . . 125
4.5.3.3 Open jet corrections . . . 128
4.5.4 Carbon fibre flaplets . . . 129
4.5.5 Flaplet porosity as a metric . . . 133
4.5.6 Targeting certain Strouhal number noise reduction . . . 134
4.5.7 Other considerations . . . 134
4.5.7.1 How representative are the flaplets to the feather? . . . 134
4.5.7.2 What would happen if the flaplets were other geometries? . . . 135
4.5.7.3 Are the tested Reynolds numbers representative? . . . 136
4.5.7.4 What if flexible strings were used instead of flaplets? 136
4.5.7.5 Would the flaplets be able to prevent stall? . . . 137
4.5.8 Future work . . . 137

5 Conclusion **139**

5.1 Conclusion . . . 139
5.2 Thesis novelty . . . 140
5.3 New literature . . . 141
5.4 Future Work . . . 142

Appendices

A Uncertainty analysis **145**

A.1 Hot wire anemometery 145
A.2 Force balance 147
A.3 Microphone array 148

References **151**

List of Figures

1.1 Indicating the three main mechanisms for Owl silent flight proposed by Graham (1934). Close up images are taken from Jaworski and Peake (2013). Image of Barn Owl (*Tyto alba*) is "**Silent hunter**" by **photophilde** and is licensed under **CC BY-SA 2.0**. 2

2.1 Experimental Set-Up 13
2.2 Response of a singular flaplet to a step input. 16
2.3 Q-Criterion for case 100-10-F. Time spacing in between each image is: $\Delta t^* = \Delta t \cdot U_\infty / c = 0.055$ 18
2.4 v' POD mode comparison for the case 150-10-F. 20
2.5 Spectral analysis of the v' component from the velocity probe, $4^{\text{th}}v'$ POD mode and $2^{\text{nd}}v'$ POD mode at Re_c = 150,000 and at α = 10°. a-b-c: Baseline case. d-e-f: Flaplet case 21
2.6 Sketch of the flaplets in either synchronous or anti-synchronous motion, looking from a downstream view of the trailing-edge. 25
2.7 Neighbouring flaplet motion 26
2.8 ANSYS simulation of flaplet motion 32
2.9 Flaplet tracking, (a) is the raw image and (b) is the enhanced image with the three tracked flaplets indicated with a white dot. 33
2.10 Chordwise sensitivity of the shear-layer stabilisation effect. 34
2.11 A working demonstrator model of the piezoelectric flaplet and the comparison of the FFT response with a laser displacement sensor. . . . 37
2.12 Convergence of 'mode energy' for the 1^{st} POD mode for the case 150-10-P. 37

3.1 Experimental set-up 44
3.2 Contours of normalised third octave band SPL across the Reynolds number range studied at $\alpha_g = 0°$. The contours are normalised by their respective maximum SPL. The --- shows the $\sim Re_c^{1.5}$ trend line observed by Paterson et al. (1972) 48
3.3 Comparison of the third octave sound pressure level ($\text{SPL}_{1/3}$) at Re_c = 300,000 between experimental result and the BPM prediction model. Where the BPM model is the summation of the laminar boundary layer (LBL) noise, both the pressure and suction side turbulent boundary layer (TBL) noise and the turbulent inflow noise. 49

3.4 Single microphone measurements for each Reynolds number case, are spaced with 30dB increments for clarity. Each of the angles stated are the geometric angles of attack. For each angle and Reynolds number there are three test cases: a baseline case with no flaplets (—), the case where the flaplets are affixed to the pressure side (—) and when the flaplets are affixed onto the suction side (—). 50

3.5 Comparison of previous literatures and the present study in the tonal noise envelope for the NACA 0012 aerofoil as proposed by Lowson, Fiddes and Nash (1994). The angle of attack (α^*) is corrected using the BPM empirical correction for the open jet wind tunnel results. Neither the direct numerical simulation (DNS) or closed wind tunnel angles have been adjusted. □ Paterson et al. (1972); ◇ Lowson, Fiddes and Nash (1994); + Desquesnes, Terracol and Sagaut (2007); ▽ Inasawa, Ninomiya and Asai (2013); ○ Chong, Joseph and Kingan (2013); △ Pröbsting, Serpieri and Scarano (2014); ☆ Arcondoulis et al. (2018); × Present (tonal) and × Present (non-tonal) 52

3.6 The spatial growth rate on the pressure side of the aerofoil at different chordwise positions (x/c) against the frequency at which they occur. (---) Indicates the frequency where the tonal peak (f_n) is observed in the experiment, see Fig. 3.4b. 54

3.7 Overall sound pressure levels for the reference cases and the flaplet, pressure side mounted, cases. ΔOSPL has been plotted on the second axis to yield a clear indication of the difference at each Reynolds number. The zero line on the ΔOSPL axis is shown as (---). Reference (—), flaplets pressure side mounted (—) and flaplets suction side mounted (—). ○ Indicates the ΔOSPL of the pressure side mounted flaplets and △ indicates the ΔOSPL of the suction side mounted flaplets. 55

3.8 Normalised lift and drag measurements for all cases, where the shading of the colours indicates the Reynolds number. A lighter shade indicates a lower Reynolds number and the darker shade indicates the higher Reynolds number cases. 57

3.9 Hot wire anemometer results of the streamwise component (u) for the case at Re_c = 243,000 and α_g = 10°. The shaded area in Fig. 3.9a is a graphical representation of the reference aerofoil orientation with respect to the profile measurements. 58

3.10 Fluctuating streamwise velocity turbulence spectra (Φ_{uu}), normalised with Φ_0 = 1 m^2/s, behind the trailing edge for the untripped case at Re_c = 243,000 and α_g = 10° 60

3.11 Calibration of the measurement systems; **(a)** calibration of the microphone array, **(b)** calibration of the hot wire anemometer, **(c)** calibration of the force balance. 63
3.12 Hot wire anemometer 4^{th} order polynomial fit for each of the wire on the X wire probe. 65
3.13 XFLR Simulation looking at lift and drag coefficients for different flaplet positions on the aerofoil at $Re_c = 350,000$. 67
3.14 Single microphone vs CleanSC beamformed acoustic spectra at $Re_c = 94,000$ and $\alpha_g = 20°$. 69
3.15 Linear stability analysis N-factor sensitivity at $Re_c = 243,000$ and $\alpha_g = 10°$. 69
3.16 Skin friction coefficient on the pressure side of the aerofoil across the whole chord, at $Re_c = 243,000$ and $\alpha_g = 10°$. Where the red line indicates where the skin friction coefficient is negative. 70

4.1 Overview of experimental set-up. 79
4.2 Response of the flaplets to a step input, normalised with the stating position (y_0) and the time is normalised by the measured Eigen frequency ($t^* = t \cdot \omega_n$, t is the time in seconds, ω_n is the observed Eigen frequency in Hz). 83
4.3 Far field narrow-band sound pressure level spectra $re\ 20\mu$Pa for the reference (plain) aerofoil, focusing on the tonal noise produced at $\alpha_g = 10°$. Each of the spectra are spaced with 50 dB from each other for clarity. The frequency has been scaled with the local scaling factor of $U_\infty^{0.8}$. . . 85
4.4 Tonal peaks (solid) and fringe frequencies (hollow) for each Reynolds number at $\alpha_g = 10°$. Global and local trend lines from Paterson et al. (1972) are also indicated. 86
4.5 Flow visualisation comparing the pressure side of the aerofoil for the reference aerofoil (left) and the baseline flaplets (right), at $Re_c = 350,000$ and $\alpha_g = 10°$. The flow direction is indicated in the bottom left of the image. 87
4.6 1/3 Octave band acoustic spectra for variation in length. Each of the spectra are spaced with 35 dB from each other for clarity. 88
4.7 ΔL_p contours for variation in length, with the zone of maximum reduction indicated. 90
4.8 2D sound maps as the length is varied, at Re_c=350,000 and $\alpha_g = 10°$. (a–d) shows the frequency band, f_c=1 kHz and (e–h) shows the frequency band, f_c = 8 kHz. (- - -) indicates the jet nozzle, (**- - -**) indicates the aerofoil, (——) indicates the interrogation region for acoustic spectra. 92
4.9 OSPL, denoted as L_{pt}, and Delta OSPL, ΔL_{pt}, for variation in flaplet length. 94

4.10 Mean and RMS wake profiles of the streamwise velocity component at $Re_c = 200,000$ for variation in length. 96
4.11 Fluctuating vertical velocity component, v', turbulence spectra (Φ_{vv}) normalised with a nominal $\Phi_0 = 1$ m^2/s at the peak RMS point in wake profiles at $\alpha_g = 15°$ and $Re_c = 200,000$ for variation in length. 97
4.12 Spectra of the laser displacement measurements, (Φ_{yy}) normalised with a nominal $\Phi_1 = 1$ m^{2}s at $\alpha_g = 0°$ for variation in length. 98
4.13 Normalised flapping frequency, with the respective Eigen frequency f_1, as Reynolds number increases at $\alpha_g = 0°$ for variation in length. 100
4.14 1/3 Octave band acoustic spectra for variation in width. Each of the spectra are spaced with 35 dB from each other for clarity. 101
4.15 ΔL_p contours for variation in width, with the zone of maximum reduction indicated. 102
4.16 2D sound maps as the width is varied, at Re_c=350,000 and $\alpha_g = 10°$. (a–d) shows the frequency band, f_c=1 kHz and (e–h) shows the frequency band, $f_c = 8$ kHz. (- - -) indicates the jet nozzle, (- - -) indicates the aerofoil, (——) indicates the interrogation region for acoustic spectra. 103
4.17 OSPL, denoted as L_{pt}, and Delta OSPL, ΔL_{pt}, for variation flaplet in width. 103
4.18 Mean and RMS wake profiles of the streamwise velocity component at $Re_c = 200,000$ for variation in width. 104
4.19 Fluctuating vertical velocity component, v', turbulence spectra (Φ_{vv}) normalised with a nominal $\Phi_0 = 1$ m^2/s at the peak RMS point in wake profiles at $\alpha_g = 15°$ and $Re_c = 200,000$ for variation in width. 105
4.20 Spectra of the laser displacement measurements, (Φ_{yy}) normalised with a nominal $\Phi_1 = 1$ m^{2}s at $\alpha_g = 0°$ for variation in width. 107
4.21 Normalised flapping frequency, with the respective Eigen frequency f_1, as Reynolds number increases at $\alpha_g = 0°$ for variation in width. 108
4.22 1/3 Octave band acoustic spectra for variation in inter-spacing. Each of the spectra are spaced with 35 dB from each other for clarity. 109
4.23 ΔL_p contours for variation in space, with the zone of maximum reduction indicated. 110
4.24 2D sound maps as the inter-spacing is varied, at Re_c=350,000 and $\alpha_g = 10°$. (a–d) shows the frequency band, f_c=1 kHz and (e–h) shows the frequency band, $f_c = 8$ kHz. (- - -) indicates the jet nozzle, (- - -) indicates the aerofoil, (——) indicates the interrogation region for acoustic spectra. 110
4.25 OSPL, denoted as L_{pt}, and Delta OSPL, ΔL_{pt}, for variation flaplet inter-spacing. 111
4.26 Mean and RMS wake profiles of the streamwise velocity component at $Re_c = 200,000$ for variation in inter-spacing. 112

4.27 Fluctuating vertical velocity component, v', turbulence spectra (Φ_{vv}) normalised with a nominal $\Phi_0 = 1$ m^2/s, measured at the peak RMS point in wake profiles at $\alpha_g = 15^\circ$ and $Re_c = 200,000$ for variation in inter-spacing. Each spectrum is spaced by 10 dB for each other for clarity. 112
4.28 Spectra of the laser displacement measurements, (Φ_{yy}) normalised with a nominal $\Phi_1 = 1$ m^{2}s at $\alpha_g = 0^\circ$ for variation in inter-spacing. 113
4.29 Normalised flapping frequency, with the respective Eigen frequency f_1, as Reynolds number increases at $\alpha_g = 0^\circ$ for variation in inter-spacing. 114
4.30 Comparison of the reference aerofoil vibration (a), the flaplets vibration (b) and the RMS of the vibrations (c) at $\alpha_g = 0^\circ$. 118
4.31 Comparison of the reference aerofoil vibration (a), the flaplets vibration (b) and the RMS of the vibrations (c) at $\alpha_g = 10^\circ$. 119
4.32 Comparison of different beamforming models for the reference aerofoil at $Re_c = 300,000$ and at $\alpha_g = 10^\circ$. 121
4.33 Comparison of sound maps produced by different beamforming algorithms at the third octave band, $f_c = 8$ kHz. 124
4.34 Comparison of the amount of iterations used for the DAMAS beamforming model for the reference aerofoil at $Re_c = 300,000$ and at $\alpha_g = 10^\circ$. . 125
4.35 Comparison of fine (0.01 m) and a coarse (0.02 m) beamforming grid spacing 126
4.36 Diagram showing the effect of how the shear layer refracts the acoustic ray from a noise source in the core jet. This figure is adapted from Fig. 1.22 in Allen et al. (2002). 127
4.37 Comparison of the baseline flaplets at Re_c=350,000 and $\alpha_g = 10^\circ$, with and without the shear layer corrections applied. 128
4.38 Comparison of the baseline flaplets vibration (a), the carbon fibre flaplets vibration (b) and the RMS of the vibrations (c) at $\alpha_g = 0^\circ$. 130
4.39 1/3 Octave band acoustic spectra for flaplets of different thickness and material. Each of the spectra are spaced with 35 dB from each other for clarity. 131
4.40 ΔL_p contours for flaplets of different thickness and material, with the zone of maximum reduction indicated. 132
4.41 Flaplet porosity against Overall Sound Pressure Level at $Re_c = 500,000$ and at $\alpha_g = 0^\circ$. 134
4.42 Average Strouhal number (St_c^*) of the reduced sections in Figure 4.7 against the length of the flaplet normalised with the chord length. . . . 135

List of Tables

2.1 TR-PIV parameters used for the two different Re_c 14
2.2 Test matrix nomenclature 16
2.3 Flaplet dynamics and material properties 17
2.4 Spectra results, Strouhal number and boundary layer quantities. 23
2.5 Flaplet motion synchronisation probabilities 26

3.1 Flaplet Dimension and Material Properties 45
3.2 Average ΔOSPL for each of the geometric angles of attack (α_g). A placement of 'P' indicates that the flaplets are affixed to the pressure side and 'S' indicates a suction side placement. 56
3.3 Hot wire anemometery calibration coefficients. 65
3.4 Comparison of the set input wind tunnel velocity and the measured velocity, after the calibration and resolution of each component. 66

4.1 Geometric specifications and naming convention for the tested flaplet cases. The thickness of each flaplet configuration was constant at 0.18 mm. 82
4.2 Experimental Eigen frequencies, finite element analysis predictions of the 1st bending ($f_{1^{st}B}$), 1st torsion ($f_{1^{st}T}$) and 2nd bending ($f_{2^{nd}B}$) bending modes and an estimation of the flutter frequency using Eqn. (4.1) from Xin et al. (2017) 83

A.1 Hot wire anemometery uncertainty, where the input data are; U = 19.7 m/s, V = 10 V, n = 24 bit, $\partial U/\partial V$ = 15.35 ms^{-1}/V and $\theta = 3°$. 147
A.2 Force balance calibration uncertainty. 148
A.3 Microphone calibration uncertainty. 149

Acknowledgements

First and foremost I would like to thank my supervisor Prof. Christoph Brücker for his unwavering support, guidance and friendship throughout my entire PhD. I would also extend my sincere thanks to Dr. Thomas Geyer, who welcomed me, so graciously, to Brandenburg Institute of Technology - Cottbus and helped me immeasurably in understanding and interpreting the acoustic results.

I could not have completed this without the support of my fellow colleagues and friends. A thank-you goes to Ale, Carlo, Isabella, Junxian, Marco, Mohamed, Muthu, Nick, Omar, Qianhui, Shane and Toby. Also thanks to all the staff, past and present at City who have helped me throughout my entire time at university; especially Roger Valsler, Jamshid Nouri, Chak Cheung and Youyou Yan. Not forgetting the 'City Brew' team - Chetan, Chris, Seb and Richard; thank-you for all fun we had in Bermondsey on Fridays and the endless conversations on everything from space to la cucaracha.

I would also like to thank my parents and brother for their support throughout my time at university and support when I needed it. Also to Spencer and Jack who have always helped and supported me - keeping me sane, either at the pub or at Cascades. Finally, I would like to thank my loving girlfriend Elizabeth for always being there for me over the past couple of years, words cannot even begin to convey my gratitude.

Declaration

I, Edward Talboys, declare that this thesis entitled *On the aerodynamic and aeroacoustic effect of passive trailing edge flaplets* and the work presented in the thesis are both my own, and have been generated by me as the result of my own original research. I grant powers of discretion to the University Librarian to allow the thesis to be copied in whole or in part without further reference to the author. This permission covers only single copies made for study purposes, subject to normal conditions of acknowledgements. I confirm that:

- this work was done wholly or mainly while in candidature for a research degree at this University;
- where I have consulted the published work of others, this is always clearly attributed;
- where I have quoted from the work of others, the source is always given. With the exception of such quotations, this thesis is entirely my own work;
- I have acknowledged all main sources of help;
- parts of this work have been published as Talboys and Brücker (2018), Talboys, Geyer and Brücker (2019a) and Talboys et al. (2021).

Signed:.....

Date:.....

Summary

A passive, bio-inspired solution for improving aerodynamic and aeroacoustic performance has been investigated for this thesis. The work was a series of experimental campaigns carried out on a NACA 0012 aerofoil, with passive trailing-edge flaplets. These flaplets are extended from the trailing edge, and are essentially cantilever elements that can freely oscillate in the flow. The thesis is split into three publications, where the first publication is an aerodynamic study and the latter two are aeroacoustic studies.

The first publication was a time-resolved particle image velocimetry (TR-PIV), focused on the rear part of the aerofoil. In this publication it was seen that when the flaplets were attached to the suction side of the aerofoil, non-linear instabilities in the shear-layer were damped. This is thought to be due to an upstream lock-in mechanism caused by the freely oscillating flaplets. These non-linear instabilities cause the shear-layer vortices to merge, therefore by damping these instabilities, the shear-layer rollers have a lower probability of merging. Hence, a thinner boundary layer and a predicted reduction in drag.

The first of the aeroacoustic studies was to investigate; firstly the effect of the flaplets on aerofoil self-noise and secondly whether there was any difference on the placement of them on the suction or the pressure side of the aerofoil. In both cases it was seen that there was a reduction in low frequency noise and an increase in high frequency noise. A reduction in tonal noise was also seen in both cases. However, it was almost completely eradicated for the case where the flaplets were attached to the suction side. This is thought to be due to the unintentional tripping of the boundary layer, caused by a small step created as the flaplets were attached to the aerofoil. As such there was no separation bubble on the suction side of the aerofoil, a necessary feature for aerofoil tonal noise.

The second aeroacoustic study was a comprehensive study, looking at changing different geometrical parameters of the flaplets and seeing what a change in length, width and inter-spacing has on the far field acoustic spectrum. What could be clearly seen was that there was a Strouhal number band of noise reduction, the same 'low frequency' noise reduction seen in the previous study, could be shifted by altering the length of the flaplets. The magnitude of this reduction band could also be increased with increased width and decreased with a smaller width flaplets. Another effect that was observed, was that as the flaplet inter-spacing was increased, the acoustic spectra trended back towards the original untreated trailing edge.

Nomenclature

Greek symbols

α	Angle of attack.
α_g	Geometric angle of attack.
α_k	Wavenumber at k^{th} vibration mode.
α_i	Complex wavenumber in streamline direction.
α^*	Adjusted angle of attack used in the BPM angle correction.
δ	Boundary layer thickness.
δ^*	Boundary layer displacement thickness.
ζ	Additional geometric factor used in the BPM angle correction.
λ_0	Shear-layer roll-up wavenumber.
ξ	Damping coefficient.
ρ	Air density.
ρ_f	Flaplet material density.
σ	Aerofoil chord to nozzle diameter factor used in the BPM angle correction.
ϕ	Phase delay.
Φ_0	Nominal value to normalise velocity turbulence spectra.
Φ_1	Nominal value to normalise displacement spectra.
Φ_{uu}	Turbulence spectra in the u' velocity component.
Φ_{vv}	Turbulence spectra in the v' velocity component.
Φ_{yy}	Displacement spectra in the y' direction.
ψ	Damping ratio.
ω_n	Natural frequency.
ω_d	Damped frequency.

Latin symbols

A . . . . . Cross sectional area of flaplet.

b . . . . . Flaplet tip displacement in y direction.

b_0 . . . . . Maximum flaplet tip displacement in y direction.

$\hat{b}$ . . . . . Normalised flaplet tip displacement with maximum tip displacement.

c . . . . . Aerofoil chord.

C_D . . . . . Drag coefficient.

C_L . . . . . Lift coefficient.

C_i . . . . . Hot wire calibration coefficients.

d . . . . . Flaplet inter-spacing distance.

D . . . . . Wind tunnel nozzle diameter.

E . . . . . Young's Modulus.

E_{vs} . . . . . Energy per unit mass associated with vortex shedding energy.

f . . . . . Frequency.

f_c . . . . . Centre frequency for octave bands.

f_f . . . . . Flutter frequency.

f_k . . . . . Eigen frequency at k^{th} vibrational mode.

f_0 . . . . . Shear-layer fundamental frequency.

$f_{0-1/2}$ . . . . . Shear-layer instability frequency.

f_{0c} . . . . . Calculated shear-layer fundamental frequency.

$f_{1^{st}B}$ . . . . . Flaplet first bending mode frequency.

$f_{2^{nd}B}$ . . . . . Flaplet second bending mode frequency.

$f_{1^{st}T}$ . . . . . Flaplet first torsional mode frequency.

$f_{2^{nd}T}$ . . . . . Flaplet second torsional mode frequency.

F_D . . . . . Drag force.

F_{D^*} . . . . . Normalised drag force.

F_L . . . . . Lift force.

F_{L^*} . . . . . Normalised lift force.

h . . . . . Flaplet thickness.

I . . . . . Area moment of inertia.

K	Non-dimensional bending stiffness.
L	Flaplet length.
L_p	Sound pressure level.
L_{pt}	Overall sound pressure level.
Re	Reynolds number.
Re_c	Chord based Reynolds number.
S_k	PIV particle stokes number.
St_c	Chord based Strouhal number.
St_0^*	Shear-layer Strouhal number.
t	Time.
t^*	Non-dimensional time.
u	x (streamwise) velocity component.
u'	Fluctuating streamwise velocity component.
u_{RMS}	RMS of the streamwise velocity.
U_{es}	Boundary layer edge velocity.
U_0	Shear-layer roller convection velocity.
U_∞	Free-stream velocity.
v	y (wall-normal) velocity component.
v'	Fluctuating wall-normal velocity component.
w	Flaplet width.
x	Chordwise / streamwise coordinate.
y	Wall-normal coordinate.
y'	Fluctuating flaplet tip displacement.
z	Spanwise coordinate.

Acronyms

2D . . . . . Two-dimensional.

3D . . . . . Three-dimensional.

BL . . . . . Boundary layer.

BPM . . . . . Brooks, Pope and Marcolini.

CTA . . . . . Constant temperature anemometer.

DNS . . . . . Direct numerical simulation.

DPIV . . . . . Digital particle image velocimetry.

FEA . . . . . Finite element analysis.

FFT . . . . . Fast Fourier Transform.

HS TR-PIV . . . High speed time resolved particle image velocimetry.

HWA . . . . . Hot wire anemometery.

LBL . . . . . Laminar boundary layer.

LED . . . . . Light emitting diode.

LSA . . . . . Linear stability analysis.

Nd:YLF . . . . . Neodymium-doped yttrium lithium fluoride.

OSPL . . . . . Overall sound pressure level.

PIV . . . . . Particle image velocimetry.

POD . . . . . Proper orthogonal decomposition.

PSF . . . . . Point spread function.

RANS . . . . . Reynolds Averaged Navier Stokes.

RMS . . . . . Root mean square.

SPL . . . . . Sound pressure level.

TBL . . . . . Turbulent boundary layer.

TE . . . . . Trailing edge.

T-S . . . . . Tollmien-Schlichting.

TR-PIV . . . . . Time resolved particle image velocimetry.

1 Introduction

Contents

1.1 Introduction **1**
1.1.1 Aerofoil self-noise mechanisms 5
1.2 Thesis structure **6**

1.1 Introduction

Engineers have been looking to nature for centuries to assist in the development of humankind. Whether that is looking to bees and their hives to assist in developing a high-strength low weight structure or looking at hydrophobic plant leaves to create water repellent surfaces. Aerodynamicists have also looked to nature to be inspired in their designs. Whether that is to increase aerodynamic performance or aeroacoustic performance, by looking to avian species, aquatic animals and even plants for these performance gains.

An example of looking to aquatic animals can be seen with the extensive research on leading edge undulations from the pectoral fin of a humpback whale. When attached to the leading edge of an aerofoil, they were observed to delay stall by re-energising of the boundary layer (Miklosovic et al., 2004). This bio-inspired technology has been trialled on wind turbines to see if this can be a viable method to increase the efficiency of

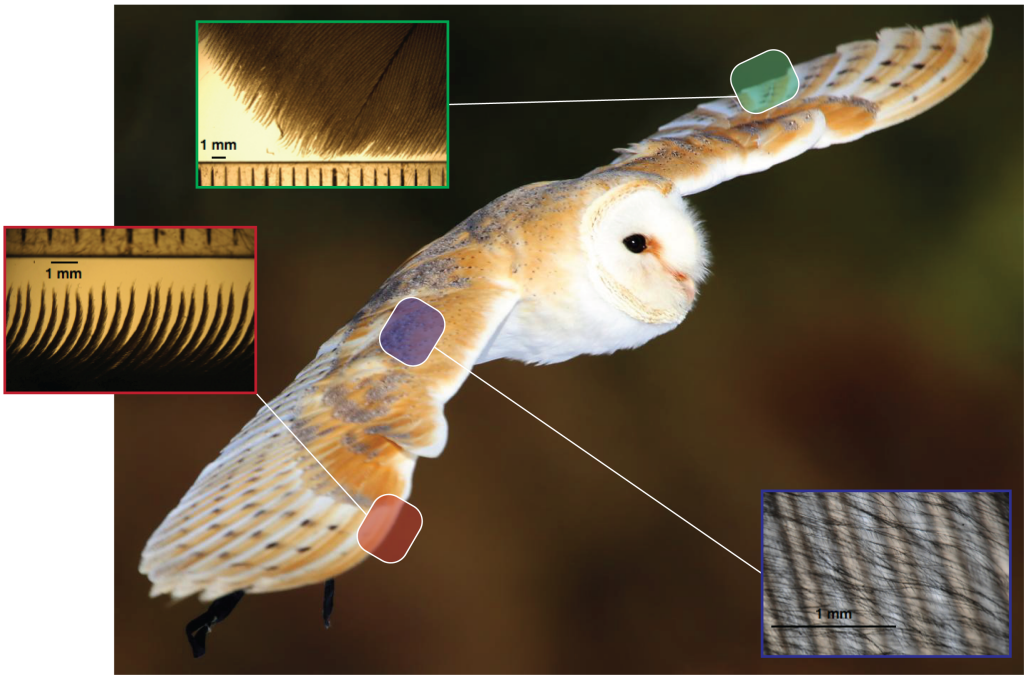


Figure 1.1: Indicating the three main mechanisms for Owl silent flight proposed by Graham (1934). Close up images are taken from Jaworski and Peake (2013). Image of Barn Owl (*Tyto alba*) is "**Silent hunter**" by **photophilde** and is licensed under **CC BY-SA 2.0**.

future wind turbines. Another example is the denticles that are found on a sharks skin. Denticles are microstructures on the surface of the sharks skin, and it has been seen that these microstructures can help reduce the drag on the body; with the additional benefit of increasing anti-fouling properties on the surface of a ships hull (Bhushan, 2012).

When looking to the plant world, the long flight time of the simple dandelion seed could be used for future light-weight parachute designs. The mechanics behind the dandelion seed flight was recently discovered by Cummins et al. (2018). They found that there was a separated vortex ring created above the pappus of the dandelion seed, due to the flow passing through the bristles. This separated vortex causes a suction effect allowing the seed to float and be dispersed by the wind over long distances.

The subject of this thesis is mimicking the feathers of birds, in particular those which are on the leeward edge of the barn owls wing. These feathers are inherently flexible and therefore to see what effect these flexible feathers have on the aerodynamic and acoustic performance was the origin of this thesis.

Graham (1934) was the first to look into the 'silent' flight of owls, and since then

significant amounts of research has been carried out to see if we can mimic the techniques the owls use for human applications. Graham (1934) proposed that the owls have three key features on their wings that allow this silent flying (fig.1.1). These are; leading edge combs-like fringes, soft downy upper surface and trailing edge fringes. The most pertinent for this project is the trailing edge fringes, however for completeness a short summary of the other two mechanisms and their benefits are given here also. For further details see the recent review article published by Jaworski and Peake (2020).

The first feature specific to owl feathers (only the primary feathers) is a leading edge comb, these are stiff comb-like fringes that protrude from the feathers which are situated on the leading edge of the birds wing. Lilley (1998) argued that the leading edge combs act as vortex generators for the oncoming flow. This could help to trip the boundary layer flow from laminar to turbulent, stabilising the flow along the upper surface of the wing and preventing laminar separation. The acoustics benefit have been seen to only be minor (Geyer et al., 2016; Geyer et al., 2017b), where the combs break up large turbulent eddies prior to them interacting with the leading edge, yielding a small low frequency reduction and a slight increase at high frequencies. They also have been seen to reduce the tip vortex noise of the owl. During my PhD, I also joined a research project looking into the importance of the curvature of the barbs of the leading edge comb. We found that they lead to a flow turning effect and possible laminar flow control. This work has recently been published in Muthuramalingam et al. (2020).

The second special feature is the 'downy upper surface', which Graham (1934) conclude is analogous to a porous surface. Many studies have been since carried out on porous aerofoils and trailing edges. As an example, a rather complete work of a SD7003 aerofoil with varying porosities has been carried out is published by Geyer, Sarradj and Fritzsche (2010), where they measured acoustic and aerodynamic effects. They concluded that a porous aerofoil can reduce the low-medium frequency noise by up to 10 dB, with a slight increase at higher frequencies. They also saw that as the aerofoil porosity increased the high frequency noise increase was also worsened. This is thought to be due to the surface roughness of the porous materials. The aerodynamic results for all porosities were worse then those of the reference (non-permeable) case,

and scaled with the level of porosity i.e. the least porous aerofoil had a slight reduction in lift and increase in drag and the most porous had the largest reduction in lift and decrease in drag compared to the reference aerofoil.

The third feature is the 'trailing edge fringes', which is where the current project takes its inspiration from. Many different alternative devices have been investigated from the basis of trailing edge fringes, whether they are serration or brush-like structures. Serrations is the most common and famous example, in part due to the commercialisation where they have been used on the nacelle of jet engines or on the trailing edge of wind turbine blades. As such they have had a large amount of research conducted on the modification. Oerlemans et al., 2009, found that when the serrations were added to a 94 m diameter wind turbine, the noise level was reduced in the low frequency range with an increase at higher frequencies. Importantly, this high frequency increase was only seen at the low wind speeds and was diminished at the higher wind speeds. The overall maximum noise reduction was in the order of 5 dBA at wind speeds of 10 m/s and the average reduction across all of the tested speeds was 3.2 dBA. Many different research groups have found that the serrations generally reduce the noise level, whether the serrations are added via a flat plate extended from the trailing edge, or via a saw-tooth pattern cut directly into the aerofoil body (Chong, Joseph and Gruber, 2013).

Herr and Dobrzynski (2005) and Herr (2007), investigated the effect of putting a brush-type extension on the trailing edge in a turbulent flow. Initially this was tested on a flat plate to purely ascertain any acoustic benefit and whether a scaling law could be developed for this extension type. Significant noise reduction in the order of 6 dB, can be seen in the range of frequencies of ~1 kHz – 6 kHz. They then go on to add that there are some crucial parameters that need to be met if any benefit is seen. The fibres need to be of a certain length, inter-spacing between fibres needs to be minimal (<0.1 mm) and they should be flexible. This gave the conclusion that this device works as viscous damper, damping the turbulent pressure fluctuations.

Studies with a single flexible element attached to the trailing using a DNS simulation were done by Schlanderer and Sandberg (2013) and later experimentally by Das et al. (2015). They found that the compliant trailing edge reduced the noise in the low and

intermediate range. However, Schlanderer and Sandberg (2013) saw an increase localised at the first three Eigen frequencies of the flap.

Kamps et al. (2017) tested an array of flexible oscillators (flaplets) attached to the trailing edge, rather than one individual element. Two different lengths of the oscillator were tested on a NACA0010 aerofoil and it was found that there was a reduction in tonal noise whilst there was an increase in the broadband noise at higher frequencies. They also noted that the longer flaplets were not as effective and reasoned that this was due to mechanical interaction of the flaplets. No reasoning for the acoustic benefit was given and this was the starting point for the current project.

1.1.1 Aerofoil self-noise mechanisms

Aerofoil self-noise is the noise emitted due to the interaction of the aerofoil body and the surrounding near wall flow. The main noise sources are predominantly caused by the boundary layer and the trailing edge of the aerofoil. Other self-noise mechanisms are due to the trailing-edge bluntness of the aerofoil, if a tip vortex is present or if there is separated flow on the aerofoil. These five mechanisms have been detailed by Brooks, Pope and Marcolini (1989) and herein they will be briefly discussed.

1.1.1.1 Turbulent boundary layer noise.

This noise source occurs due to the interaction of the turbulent boundary layer - trailing edge interaction. Within a turbulent boundary layer there are many different scales of turbulence, as such the noise radiated from the trailing edge is broadband in nature. At high Reynolds numbers, when there is no flow separation, this is the main source of aerofoil self-noise and can be well described using surface pressure measurements using empirical predictor models.

1.1.1.2 Laminar boundary layer noise.

Laminar boundary layer trailing edge noise manifests itself as discrete tones on a broadband hump. This type of boundary layer trailing edge interaction is more commonly known as ‘tonal noise’ and is discussed in great detail within this study. Tonal noise exists when there is a separation bubble on the pressure side of the aerofoil, and is caused by

the amplification the most unstable Tollmein-Schlichting mode at the point of separation near the trailing edge. A more detailed overview of tonal noise is detailed in §3.1.

1.1.1.3 Separation noise.

Separation or stall noise or is the noise due to flow separation on the aerofoil. By the nature of stall, this occurs at moderate to high angles of attack and can occur from the whole chord in deep stall or just from the trailing edge region in moderate stall cases. This noise source, is a dominant source when it occurs and can be up to 10 dB above an attached turbulent boundary layer noise scenario.

1.1.1.4 Trailing edge bluntness noise.

Trailing edge bluntness noise is caused due to the vortices being shed from the blunt trailing edge. The tone of the emitted noise is strongly dependent on how blunt the trailing edge is and the flow velocity. Therefore the typically bluntness noise source is high frequency noise for, due to the trailing-edges being typically quite 'sharp' (i.e. not blunt). Saying this, for blunt trailing edges (and even cylinders) the frequency can be quite low. Bluntness noise can be quite prevalent within the acoustic spectrum and manifests itself as a singular tone.

1.1.1.5 Tip vortex noise.

Tip vortex noise is caused by the turbulence within the wing tip vortex at the free-end of a blade / aerofoil section. The mechanism of the noise is caused by the interaction of the trailing edge and the wing tip vortex.

1.2 Thesis structure

The thesis is structured in a prospective publication format. Three publications are included herein as separate chapters. Each publication is followed by a critical analysis of the publication, where further clarifications, improvements to the study and future work are highlighted. Chapter 2 looks into the aerodynamic benefit of having trailing edge flaplets attached to a NACA 0012 aerofoil. Chapters 3 and 4, are aeroacoustic studies

where the focus was firstly to investigate what effect the flaplets had on the aeroacoustics (Chapter 3) and then to see if there was an 'optimal' geometry of flaplet (Chapter 4).

The structure of each publication is: (i) an abstract – a short summary of the publication. (ii) An introduction – where introductory remarks on the work is given and this section also includes a brief literature review of relevant previous work. (iii) Experimental arrangements / set-up – an overview of the materials and methods used for the experiment is given. Information on the data analysis techniques is also given in this section. (iv) Results-discussion – the results of the experiments are given and the discussion on the findings in is given. (v) Conclusion on the findings and proposed future work is discussed.

List of publications

- Talboys, E. and Brücker, C. 'Upstream shear-layer stabilisation via self-oscillating trailing edge flaplets'. *Experiments in Fluids 59.10* (2018), p. 145.
- Talboys, E., Geyer, T.F. and Brücker, C. 'An aeroacoustic investigation into the effect of self-oscillating trailing edge flaplets.' *Journal of Fluids and Structures*, 91 (2019): 102598.
- Talboys, E., Geyer, T.F., Prüfer, F. and Brücker, C. 'A parametric study of the effect of self-oscillating trailing-edge flaplets on aerofoil self-noise'. *Applied Acoustics*, 177 (2021): 107907.

List of conference proceedings

- Talboys, E., Geyer, T.F. and Brücker, C. 'The Aerodynamic And Aeroacoustic Effect Of Passive High Frequency Oscillating Trailing Edge Flaplets'. In: *IUTAM Symposium on Critical Flow Dynamics involving Moving/Deformable Structures with Design applications.* Santorini, Greece, 2018
- Talboys, E., Brücker, C. 'Shear Layer Instability Control Via Trailing Edge Flaplets: Wind Tunnel Study Using TR-PIV.' In:*19th International Symposium on Applications of Laser and Imaging Techniques to Fluid Mechanics.* Lisbon, Portugal, 2018.

- Talboys, E., Geyer, T.F., Prüfer, F. and Brücker, C. 'An aeroacoustic investigation into the effect of self-oscillating trailing edge flaplets.' In: *European Postgraduate Fluid Dynamics Conference.* Ilmenau, Germany, 2019.

- Talboys, E., Geyer, T.F., Prüfer, F. and Brücker, C. 'The aeroacoustic effect of different inter-spaced self-oscillating passive trailing edge flaplets.' In: *5^{th} Symposium on Fluid-Structure-Sound Interactions and Control.* Crete, Greece, 2019.

- Talboys, E., Geyer, T.F. and Brücker, C. 'Influence of self-oscillating trailing edge flaplets on turbulent boundary layer – trailing edge noise.' In: *23^{rd} International Congress on Acoustics.* Aachen, Germany, 2019.

2

Paper 1: Upstream shear-layer stabilisation via self-oscillating trailing edge flaplets

Contents

2.1 Introduction **10**
2.2 Experimental Set-Up **12**
2.2.1 Velocity Field Measurements 14
2.2.2 Flap Motion Tracking 15
2.3 Results **15**
2.3.1 Flaplet response to step input 15
2.3.2 Flow Field 17
2.3.3 Flaplet Motion 25
2.4 Conclusion **27**
2.5 Critical analysis **28**
2.5.1 Overview and study contributions 28
2.5.2 Limitations of the working hypothesis 29
2.5.3 Other aerofoil profiles 30
2.5.4 Mechanical coupling of flaplets 30
2.5.5 Tracking of flaplets 32
2.5.6 Chordwise sensitivity 33
2.5.7 Uncertainty of the High-Speed PIV measurements 34
2.5.8 Future work 35

Abstract

The flow around a symmetric aerofoil (NACA 0012) with an array of flexible flaplets attached to the trailing edge has been investigated at Reynolds numbers of 100,000 - 150,000 by using High-Speed Time-Resolved Particle Image Velocimetry (HS TR-PIV) and motion tracking of the flaplets' tips. Particular attention has been made on the upstream effect on the boundary layer evolution along the suction side of the wing, at angles of attack of 0° and 10°. For the plain aerofoil, without flaplets, the boundary layer on the second half of the aerofoil shows the formation of rollers as the shear-layer rolls-up in the fundamental instability mode (linear state). Proper Orthogonal Decomposition (POD) analysis shows that non-linear modes are also present, the most dominant being the pairing of successive rollers. When the flaplets are attached, it is shown that the flow-induced oscillations of the flaplets are able to create a lock-in effect that stabilises the linear state of the shear layer, whilst delaying or damping the growth of non-linear modes. It is hypothesised that the modified trailing edge could be beneficial for reducing drag and can reduce aeroacoustic noise production in the lower frequency band, as indicated by an initial acoustic investigation. The reduction in drag, although not measured explicitly, is a result of the reduced boundary layer thickness seen on the aerofoil with the flaplets attached.

2.1 Introduction

In recent years extensive research has been carried out by turning to nature for inspiring new designs in man-made aircraft and improving aerodynamic performance or reducing emissions such as noise or pollution. Ever increasing air travel and human habitation near airports, has led to the urgent need for cleaner and quieter air travel. A few solutions which have been previously investigated are; leading edge undulations (Miklosovic et al., 2004), serrated trailing edges (Howe, 1991), slitted trailing edges (Gruber, Azarpeyvand and Joseph, 2010), brush-like edge extensions (Herr and Dobrzynski, 2005) and porous aerofoils (Geyer, Sarradj and Fritzsche, 2010). In the present study, a flexible trailing edge consisting of an array of small elastic flaplets, mimicking the tips of bird feathers, is used.

The specific arrangement and structure of feathers on the trailing edge of an owl's wing is well known to be one of the key mechanisms that the bird uses to enhance noise suppression (Jaworski and Peake, 2013). In addition, secondary feathers on the upper side of the wings of the steppe eagle (*Aquila nipalensis*) (Carruthers, Thomas and Taylor, 2007) and the peregrine falcon (*Falco peregrinus*) (Ponitz et al., 2014), to give a few examples, have been observed to pop-up as the birds attack prey or come into land at a high angle of attack. This phenomenon has been the subject of many research studies.

Schluter (2010) could show that by attaching rigid flaps, via a hinge, on the upper surface of the wing, the C_L max is increased for a series of tested aerofoils (NACA 0012, NACA 4412, SD 8020). Schlüter also showed that the flaps bring the additional benefit of gradual stall rather than a more severe lift crisis. Osterberg and Albertani (2017) carried out a similar study on a flat plate subjected to high angles of attack, coming to the same conclusion.

Brücker and Weidner (2014) used flexible flaplets attached on the suction side of a NACA 0020 aerofoil that was subjected to a ramp-up motion. The results show a considerable delay in dynamic stall. Flap length and flap chordwise spacing were varied and it was found that the most successful configuration was two rows of flaps of length 0.1c spaced 0.15c-0.2c in the chordwise direction. The wavelength of the rollers in the shear layer was found to be of the same order, 0.15c-0.2c. This led to the conclusion that the flaplets resulted in a lock-in effect with these rollers, as the two spacial length scales were comparable. Concluding that this lock-in effect stabilises the shear layer. Rosti et al. (2017) then built on these findings of by carrying out a DNS (direct numerical simulation) parametric study. The flap element was rigid but coupled to the aerofoil surface by a torsional spring type coupling. It was found that when the flap oscillations were at the same frequency as the shear-layer roll up, the mean lift coefficient was at its highest.

Similar effects, as observed for aerofoils, have also be seen on tests with bluff bodies. A series of studies on cylinder flows with flaplets attached on the aft half of the cylinder have been carried out by Kunze and Brücker (2012) and Kamps et al. (2016) and Geyer et al. (2017a). Kunze and Brücker (2012) saw that the presence of the flexible elements allowed the shedding frequency to be locked in with the most dominant eigen-frequency

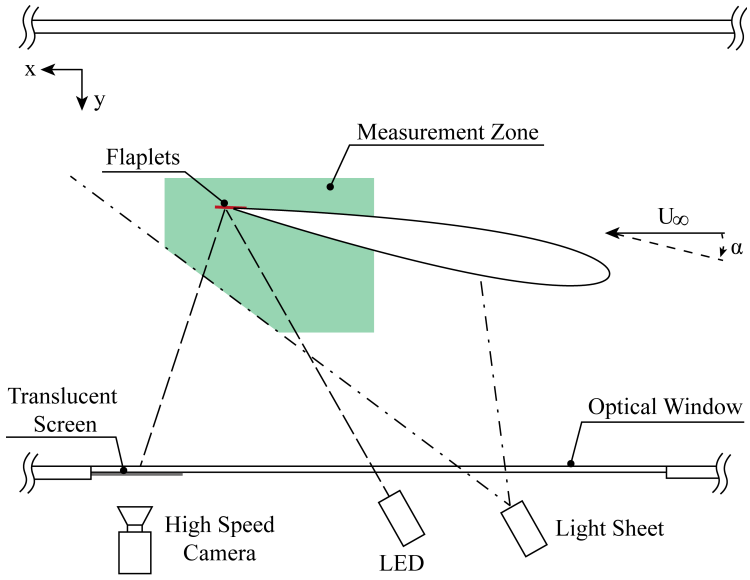
of the flaplets. This hints to a similar lock-in effect of the shear layer roll-up observed for the aerofoils, Rosti et al. (2017). Consequently the flow-structure in the wake is changed and a reduced wake deficit is observed. Kamps et al. (2016) then tested the same cylinder/flaplet configuration in an aeroacoustic wind tunnel and could show that the flaplets overall reduce noise, both in the tonal and the broadband components.

Talboys, Geyer and Brücker (2018) have very recently, during the review process of the current study, carried out an aeroacoustic campaign with the present configuration of aerofoil and self-oscillating trailing edge flaplets. They have found that when the flaplets are attached to the trailing edge, an acoustic reduction in the low to medium frequency range (100 Hz - 1 kHz) is observed over a large range of Reynolds Numbers and angles of attack. This supports the findings of the preliminary investigation carried out by Kamps et al. (2017) on a NACA 0010 with flexible flaplets attached to the trailing edge. In another recent publication Jodin et al. (2018) uses an active control technique with a vibrating solid trailing edge, which can oscillate up to 400 Hz with a peak deflection in the order of 1 mm. By using high-speed PIV in the wake it was seen that when the trailing edge oscillations are actuated, the wake thickness was reduced by as much as 10% and accompanying lift force measurements showed a 2% increase.

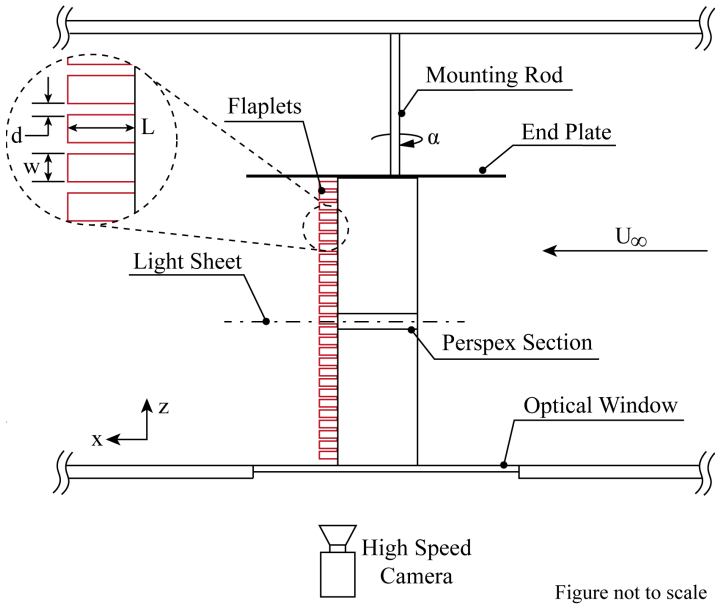
The present study builds off these previous studies in order to study the benefit/impact of flexible flaplets being attached to the trailing edge rather than on the aerofoil body. Tests of such modifications of the trailing edge by Kamps et al. (2017) and Talboys, Geyer and Brücker (2018) already show promising results in noise reduction. However, no details of the flow structure and the fluid-structure interaction are known which might explain the observed aeroacoustical modification. This is the motivation and purpose of the present study.

2.2 Experimental Set-Up

The experiments were carried out in the Handley Page laboratory at City, University of London in a closed loop wind tunnel. The test section of the tunnel is 0.81 m by 1.22 m in cross-section, and has a turbulence intensity of 0.8%. A NACA 0012 aerofoil, with a chord of 0.2 m and span of 0.52 m, was used for the present study. One side of the aerofoil



(a) Plan View



(b) Side View

Figure 2.1: Experimental Set-Up

spanned to the floor of the tunnel and an endplate was affixed to the exposed end to negate any end effects. The aerofoil was 3D printed in two sections with a small perspex section in the measurement window, as per Fig. 2.1b. The use of perspex in this region improves the quality of the PIV recordings close to the surface. Air flow with density of ρ = 1.2 kg/m^3 was applied at different flow speeds U_∞. Three chord based Reynolds

Re_c	Aperture Size	Pulse Separation	Capture Frequency
100,000	f/8	80 μs	1500 Hz
150,000	f/8	30 μs	1500 Hz

Table 2.1: TR-PIV parameters used for the two different Re_c

numbers were analysed in this study: 100,000 125,000 and 150,000; at two different angles of attack: 0° and 10°. A 0.3 mm thick boundary layer trip was implemented at 0.2c on both sides of the aerofoil to ensure that the boundary layer (BL) was turbulent.

The trailing edge with the flexible flaplets was made from a polyester foil, of thickness h = 180 μm, which was laser-cut at one long side to form an array of individual uniform flaplets. Each rectangular flaplet has on the long side a length of L = 20 mm and on the short side a width of w = 5 mm with a gap of d = 1 mm in spanwise direction (see Fig. 2.1b). The foil was adhered to the pressure side of the aerofoil using thin double sided tape such that the flaplets face downstream, with their free end located at a distance of x/c = 1.1c downstream of the trailing edge. The flaplets form a mechanical system of a one-sided clamped rectangular cantilever beam which is free to oscillate perpendicular to the mean-flow direction.

2.2.1 Velocity Field Measurements

High-Speed Time-Resolved Particle Image Velocimetry (HS TR-PIV) measurements were carried out using a 2 mm thick double pulsed Nd:YLF laser sheet in a standard planar set-up. A high speed camera (Phantom Miro M310, window size 1280 x 800 pixels) equipped with a macro lens, Tokina 100 mm, with f/8 was used in frame straddling mode. Olive oil seeding particles, of approximate size 1 μm, were added to the flow downstream of the model. A number of 500 pairs of images were captured at a frequency of 1500 Hz with the pulse separation time being altered for each case, given in Table 2.1.

The raw images were then processed using the TSI Insight 4G software which uses the method of 2D cross correlation. The first pass interrogation window size was 32 x 32 pixels, with a 50% overlap. The size was then reduced to 16 x 16 pixels for the subsequent pass. A 3 x 3 median filter was then applied to validate the local vectors, any missing or spurious vectors were interpolated by using the local mean.

Due to the limited pixel resolution of the high-speed camera and the requirement to have high-speed TR-PIV with good spatial resolution, only a small portion of the flow field could be investigated. Therefore in the present study the region of focus was the aft half and trailing edge sections of the aerofoil, as seen in Fig. 2.1b. This region was selected as this is where the modification of the flow, by the flaplets, is thought to be most prevalent.

2.2.2 Flap Motion Tracking

To track and record the real time motion of the flaplets with high resolution, a high power LED (HARDsoft IL-106G) was used alongside a second high speed camera (Phantom Miro M310) with a Nikon 50 mm f/1.8 lens. The LED was directed at the flaplets and the back reflections were seen on a translucent screen adhered to the transparent wind tunnel side wall (see Fig. 2.1a). Due to the optical lever-arm condition, small deflections of the flaplets led to a large displacement of the back-scattered light on the screen. The recordings were taken at 3200 Hz, with an exposure time of 320 μs and an aperture of f/1.8. In total 2.5 seconds of motion was recorded on the Phantom Camera Control Application (PCC), resulting in 8000 images for each case. An edge detection code (Matlab) was then used to track the flap tips motion over time. Spurious data points were removed from the data set and subsequently interpolated prior to a low pass filter (4^{th} order Butterworth low-pass with a cut-off frequency of 600 Hz) being applied to the data.

2.3 Results

The test cases mentioned in §2.2, were run both with and without the flaplets in order to ascertain a baseline for comparative analysis. For the remainder of the report the nomenclature in Table 2.2 will be used and only results for Re_c=100,000 and Re_c=150,000 are shown.

2.3.1 Flaplet response to step input

As previously mentioned (§2.2.2), the flaplets can be understood as thin rectangular cantilever beams, clamped at one side and free to oscillate in their natural bending mode

Test Name	Re_c	α	Trailing Edge
100-0-P	100,000	0°	Plain
100-0-F	100,000	0°	Flaplets
100-10-P	100,000	10°	Plain
100-10-F	100,000	10°	Flaplets
150-0-P	150,000	0°	Plain
150-0-F	150,000	0°	Flaplets
150-10-P	150,000	10°	Plain
150-10-F	150,000	10°	Flaplets

Table 2.2: Test matrix nomenclature

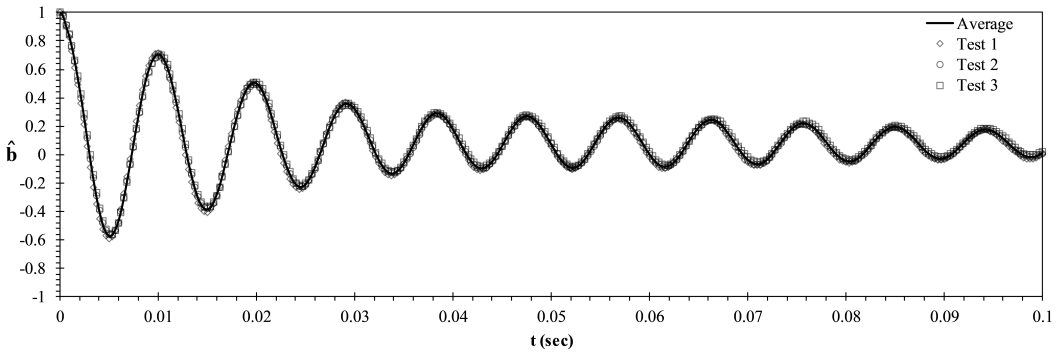


Figure 2.2: Response of a singular flaplet to a step input.

in the flow environment. The subsequent equation of motion from bending beam theory leads to the following ODE of the mechanical system (Stanek, 1965).:

$$EI\frac{\partial^2 b}{\partial x^4} = -\rho_f A\frac{\partial^2 b}{\partial t^2} - \frac{\xi}{L}\frac{\partial b}{\partial t} \tag{2.1}$$

Where E is the Young's modulus of the flaplets, I is the area moment of inertia, b is the vertical displacement of the flaplet tip, ρ_f is the flaplet material density, A is the cross-sectional area of the flaplet, ξ is the damping coefficient, The general solution for a damped harmonic oscillators is then:

$$\hat{b}(t) = \frac{b}{b_0}e^{-\psi\omega_n t}cos(\omega_d t - \phi) \tag{2.2}$$

In the case that the system is only weakly damped, the natural frequency results to:

$$f_k = \frac{\alpha_k^2 h}{2\pi L^2}\sqrt{\frac{E}{12\cdot\rho_f}} \tag{2.3}$$

A step-response test was conducted with a single flaplet being bent out of the equilibrium to an amplitude of b_0, and subsequently unloaded, after which the flaplet

oscillates back to its equilibrium position at rest. The tip motion was recorded by a high speed camera (Phantom Miro M310, 1200 x 800 pixels at 3200 Hz) and the previously mentioned edge detection script was used to track the tip. The recorded response, Fig. 2.2, gives a Q-factor of 61.6 ($Q_{factor} = 1/2\Psi$), which indicates a very weakly damped harmonic oscillator. The natural frequency of the flaplets is 107 Hz as obtained by analysing the spectrum of the signal. With the known solution of equation (2.3), for the weakly damped harmonic oscillator, and by using the first natural bending mode of the beam, $\alpha_1 = 1.875$, one can estimate the Young's Modulus of the flap material. Equation (2.3) has been further used to evaluate at which point the flaplets will go into the second vibration mode, for this case $\alpha_2 = 4.694$ leading to $f_2 = 671$ Hz.

Property	Value
f_1 at α_1	107 Hz
f_2 at α_2	671 Hz
ρ_f	1440 kg/m^3
E	3.12 GPa

Table 2.3: Flaplet dynamics and material properties

The non-dimensional bending stiffness of the flaplets has been calculated from equation (2.4) giving a minimum value of K = 6.13 x10^{-3} at Re_c = 150,000 and a maximum, K = 13.91 x10^{-3} at Re_c = 100,000. Overall, it is concluded that the flaplets are of sufficient flexibility in order to easily react with pressure fluctuations in the present flow conditions.

$$K = \frac{EI}{\rho L^3 U_\infty^2} = \frac{Ew}{12}\left(\frac{h}{L}\right)^3 \frac{1}{\rho U_\infty^2} \tag{2.4}$$

2.3.2 Flow Field

The high-speed PIV measurements were analysed to gather the coherent structures in the shear layer by conditional averaging and POD analysis. Therefore, a virtual probe location has been selected within the PIV field, which acts to give an indicative value for the passage of rollers. It is found that the proper location in the field is where

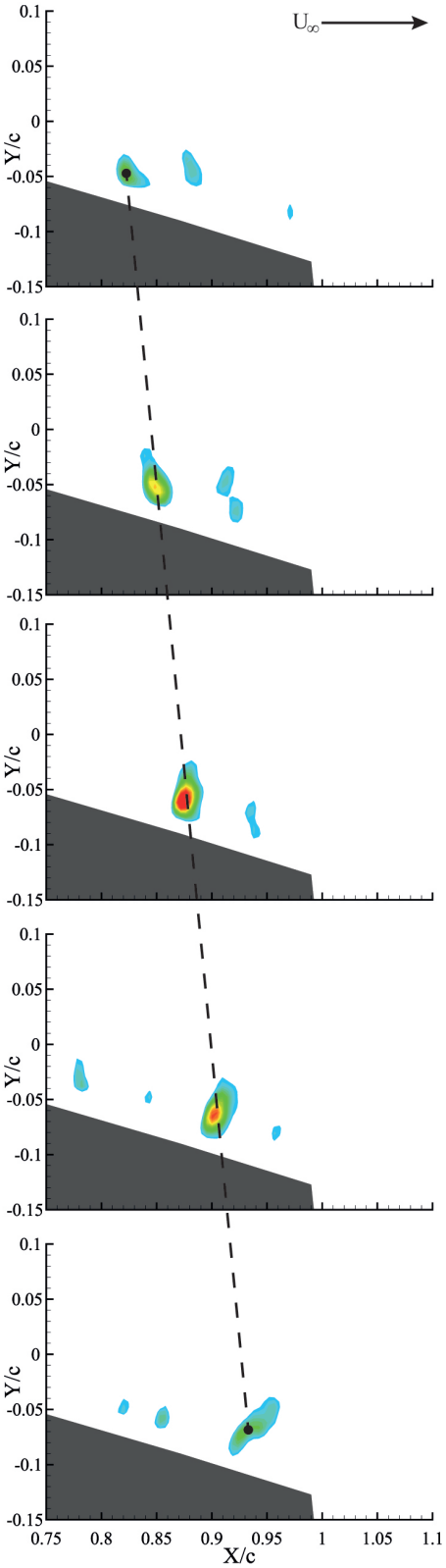
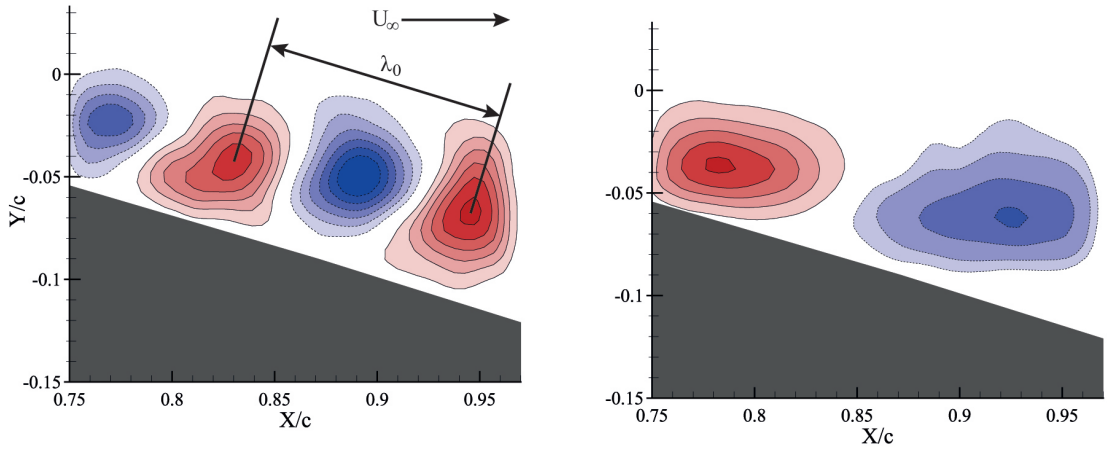


Figure 2.3: Q-Criterion for case 100-10-F. Time spacing in between each image is: $\Delta t^* = \Delta t \cdot U_\infty / c = 0.055$

the maximum RMS streamwise velocity fluctuations (u' RMS) occur. The wall normal position of the maximum u' RMS gives an approximate boundary layer displacement thickness (δ^*) and the position at which the inflection in the boundary layer occurs. Hence this location corresponds to the wall normal coordinate where the shear layer instability is most prevalent (Dovgal, Kozlov and Michalke, 1994). For the cases 150-10-P and 150-10-F, δ^*/c was found to be 0.027 and 0.028 respectively, at the chordwise location x/c = 0.85. Accordingly, the probe location has been set at x/c = 0.85 and y/c = δ^*/c.

The fluctuating vertical velocity (v') signal was recorded at the probe location (average of the 3x3 neighbouring vectors) and it was observed, from the PIV results, that the presence of a shear layer roller travelling through the probe area corresponded to a peak in the v' component. Therefore in order to visualise a clear depiction of these structures passing through the probe area, the velocity fields were conditionally averaged. To get the conditional average, the time history of the v' velocity component at the probe location was investigated. Here a peak in the time history corresponded to a roller passive through the probe location. Therefore by averaging the flow field at the time instances where these peak events occur, the frames proceeding and following provide a clear view of the movement of the structures over the aerofoil can be obtained. From these averaged frames the Q-criterion was subsequently computed and the convection speed was calculated, see Fig. 2.3. All cases fell in the range U_0/U_{infty} = 0.45 - 0.55. A further breakdown of the individual cases can be seen in Table 2.4.

In order to select the dominant modes in the flow field, a proper orthogonal decomposition (POD) of the fluctuating velocity field was carried out. POD reduces the field into modes, whereby each mode is a certain dominant flow feature or structure. Mode 1 represents the distribution of the Reynolds stresses in the boundary layer and is not shown here. In the present case the dominant features are the observed rollers that originate from the instability of the shear layer and the roll-up into vortices as seen in Fig. 2.3. The spatial reconstruction of two of the dominant modes can be seen in Fig. 2.4. Mode 4 (Fig. 2.4a) is the mode which corresponds to the fundamental instability, leading to the shear-layer rolling up into regular rows of spanwise rollers. A proof of being it mode 4 is given later based on previous research of boundary layers on aerofoils. Then,



(a) Mode 4, corresponding to f_0. Where λ_0 is the wavelength of the rollers.

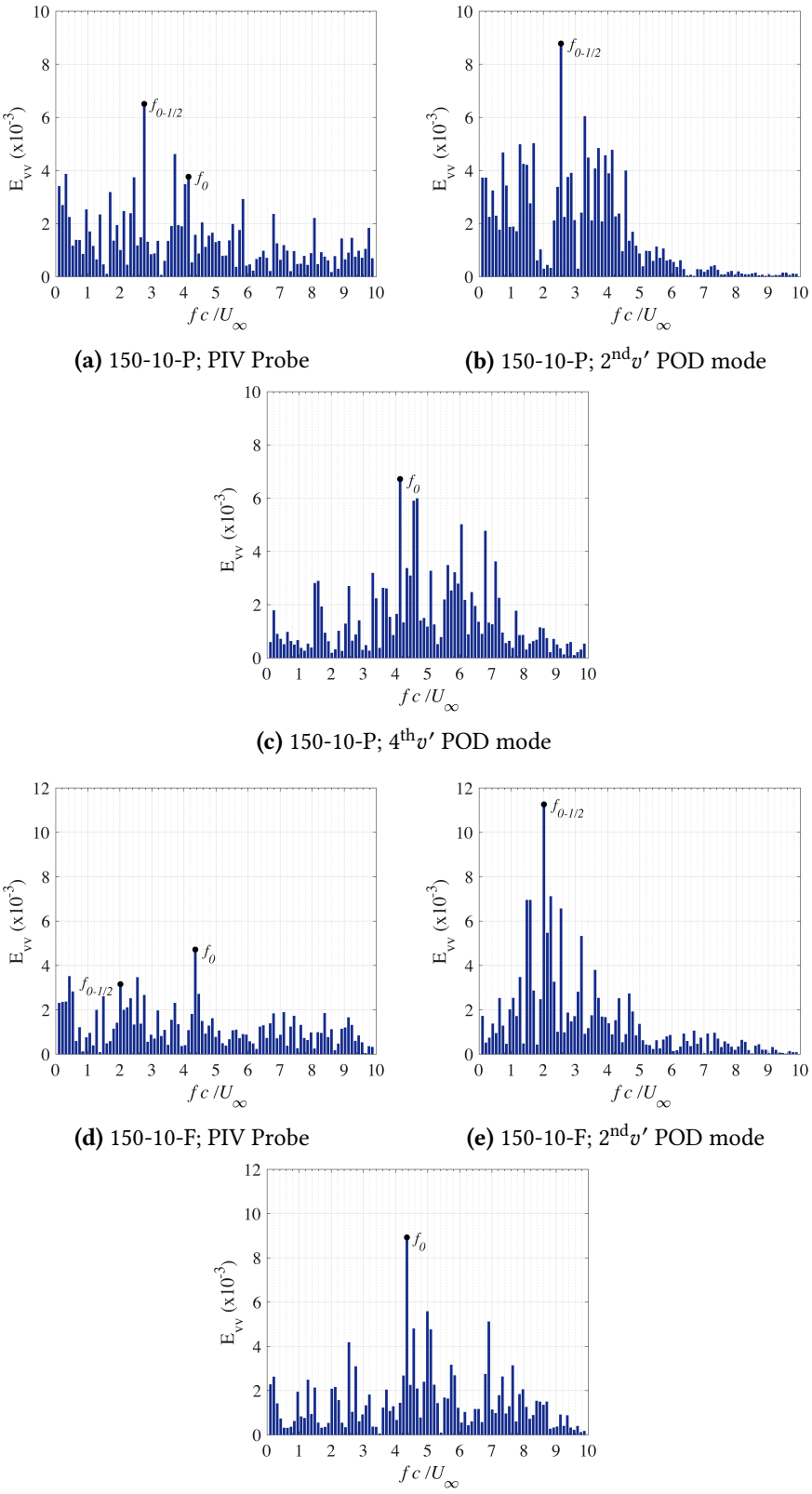
(b) Mode 2, corresponding to $f_{0-1/2}$

Figure 2.4: v' POD mode comparison for the case 150-10-F.

mode 2, Fig. 2.4b, corresponds to half of the fundamental instability which indicates the presence of a non-linear state in the shear-layer. This mode occurs at half the wavelength of the fundamental mode and represents a subharmonic feature generated by pairing of successive rollers. Mode 3 is a mixture of mode 2 and mode 4 and is linked with the fundamental mode with a factor of 2/3. Thus it seems to be an intermediate state.

$$\mathrm{St}_0^* = \frac{f_0 \lambda_0}{\mathrm{U}_{es}} = \frac{\mathrm{U}_0}{\mathrm{U}_{es}} \tag{2.5}$$

In order to justify our selection of the mode 4 representing the fundamental shear layer instability, the Strouhal number of the mode was calculated and compared to previous research on similar aerofoils, see Yarusevych, Sullivan and Kawall (2009). They suggested a certain range of the Strouhal number exists in which the fundamental mode should fall in when scaling the frequency (f_0) with the wavelength of the fundamental roll-up (λ_0) and the boundary layer edge velocity (U_{es}), see equation (2.5). Analytically Yarusevych, Sullivan and Kawall (2009) showed that this quantity should be in the region of $0.45 \leq \mathrm{St}_0^* \leq 0.5$ and more recently this range was increased to $0.3 \leq \mathrm{St}_0^* \leq 0.5$ by Boutilier and Yarusevych (2012). Values for λ_0 were obtained from the POD (Fig. 2.4) and the convection velocity of the vortex cores were calculated from the conditionally averaging, Fig. 2.3. The values of St_0^* obtained in the present study are within the



(a) 150-10-P; PIV Probe

(b) 150-10-P; 2$^{nd}v'$ POD mode

(c) 150-10-P; 4$^{th}v'$ POD mode

(d) 150-10-F; PIV Probe

(e) 150-10-F; 2$^{nd}v'$ POD mode

(f) 150-10-F; 4$^{th}v'$ POD mode

Figure 2.5: Spectral analysis of the v' component from the velocity probe, 4$^{th}v'$ POD mode and 2$^{nd}v'$ POD mode at Re_c = 150,000 and at α = 10°. a-b-c: Baseline case. d-e-f: Flaplet case

limits set by Boutilier and Yarusevych (2012) and are in agreement also with previous studies (Boutilier and Yarusevych, 2012; Thomareis and Papadakis, 2017; Yarusevych, Sullivan and Kawall, 2009; Brücker and Weidner, 2014). Similar roller wavelengths were observed by Brücker and Weidner (2014), where the wavelength they found was 0.15c - 0.2c. The value of the fundamental frequency could then be back calculated from this relationship and is presented in Table 2.4 as f_{0c}. These calculated values show good agreement with the values obtained from the v' spectra at the PIV probe location (Fig. 2.5), giving confidence in the presented frequencies. Additional analysis is carried out on the temporal coefficients of the POD modes as they represent the temporal signature of the mode (Semeraro, Bellani and Lundell, 2012; Meyer, Cavar and Pedersen, 2007). This helps to link the corresponding mode 4 with f_0 (Fig.2.5c-2.5f) and mode 2 with $f_{0-1/2}$ (Fig.2.5b-2.5e), as the identified frequencies in the v' spectra (Fig. 2.5a-2.5d). It should be noted here that, the values of the E_{vv} are really just showing how clear the frequency is within the mode (Eigen vector) and therefore the magnitude of E_{vv} shouldn't be used as a tool to compare differences between cases.

In Fig. 2.5a, 150-10-P, the dominant peak is observed at $f_{0-1/2}$, which corresponds to approximately half of the fundamental frequency and indicates the presence of mode 2. Therefore, at this condition, the shear layer upstream and near the trailing edge is already in a non-linear state with pairing of the rollers happening more often. This pairing effect has been seen in many previous studies of planar shear flows (Ho and Huang, 1982; Rajagopalan and Antonia, 2005; Rodríguez et al., 2013; Perret, 2009). It should be noted that this frequency herein is not exactly half of the fundamental peak, which is reasonable as the position of the transition point of the fundamental instability is typically fluctuating in the shear layer; hence this gives a more 'broadband' region where this frequency is seen (Prasad and Williamson, 1997; Rajagopalan and Antonia, 2005; Dong et al., 2006; Yarusevych, Sullivan and Kawall, 2009).

Once the flaplets are attached to the aerofoil and the flow is studied again at the same conditions, Fig. 2.5d. The $f_{0-1/2}$ peak is obviously suppressed and the f_0 is now the dominant frequency. Meanwhile, as shown further below, the flaplets oscillate at their natural frequency with an average amplitude of about 0.4mm (0.2%c), excited

Test Cases	PIV Probe		POD		Shear layer Strouhal number parameters					Boundary layer	
	f_0 c/U_∞	$f_{0-1/2}$ c/U_∞	f_0 c/U_∞	$f_{0-1/2}$ c/U_∞	U_0/U_∞	λ_0/c	U_{es}/U_∞	St_0^*	f_{0c} c/U_∞	δ/c	δ^*/c
100-10-P	4	—	4	—	0.466	0.138	1.02	0.456	3.36	0.0754	0.0234
100-10-F	3.52	—	3.52	—	0.498	0.154	1.02	0.488	3.23	0.0701	0.0234
150-10-P	4.14	2.76	4.14	2.55	0.497	0.125	1.04	0.478	3.98	0.0652	0.0285
150-10-F	4.35	2.02	4.35	2.02	0.519	0.131	1.04	0.499	3.96	0.0607	0.0274

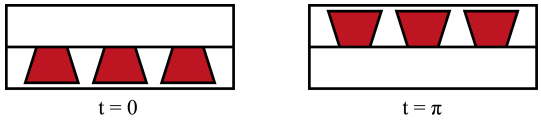
Table 2.4: Spectra results, Strouhal number and boundary layer quantities.

by the observed rollers over the trailing edge. The shift of the dominant peak back to the fundamental instability indicates that the shear-layer has now been stabilised and the growth of non-linear modes has been damped, thus reducing the tendency of vortex pairing. This stabilisation is thought to be caused by a lock-in effect between the oscillating flaplets and the shear layer fundamental instability, once the frequency of the latter exceeds the natural frequency of the flaplets. Such that they start to oscillate in the flow. This conclusion is based upon a similar observation of flow stabilisation with flaplets attached to the aft part of an aerofoil and a bluff body (Brücker and Weidner, 2014; Rosti et al., 2017; Kunze and Brücker, 2012), where the flaps act as 'pacemaker' and alter the shedding cycle, leading to a reduction in drag and lift fluctuations. It is worth to note that the herein observed stabilisation goes together with a slight reduction in the thickness of the local boundary layer edge (δ). Table 2.4, shows that with the flaplets the thickness has been reduced by 7.5%, inferring that with the attached flaplets the aerodynamic performance of the aerofoil might also benefit. It is hypothesised that the reduced thickness is the consequence of less pairing events in the stabilised situation, because the pairing causes a strong wall-normal momentum exchange and therefore a thickening of the boundary layer.

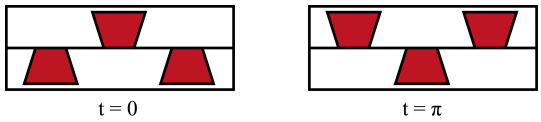
In order to investigate the chordwise sensitivity of the spectra, an additional 15 points both upstream and downstream of the presented probe location were averaged. The additional locations were taken at the same wall-normal position (δ^*/c) and with a chordwise spacing of 0.5%c. The averaged spectra showed no sensitivity in the result when compared to Fig. 2.5, and as such has not been presented here.

For the lowest Reynolds Number cases (100-10-P & 100-10-F), there was no dominating non-linear instabilities or vortex pairing (i.e. $f_{0-1/2}$) observed in the spectral analysis. The reason for this is thought to be because of the sub-critical state of the shear-layer formation at the lower flow speed (Prasad and Williamson, 1997; Rajagopalan and Antonia, 2005).

When analysing the velocity probe data for the zero degree cases, it was seen that no obvious spectral peaks were present. The shear layer at these conditions is



(a) Syncronous Motion



(b) Anti-syncronous Motion

Figure 2.6: Sketch of the flaplets in either synchronous or anti-synchronous motion, looking from a downstream view of the trailing-edge.

again expected to be in the sub-critical state as the adverse pressure gradient is weaker compared to the 10° angle of attack situation (Huang and Lin, 1995).

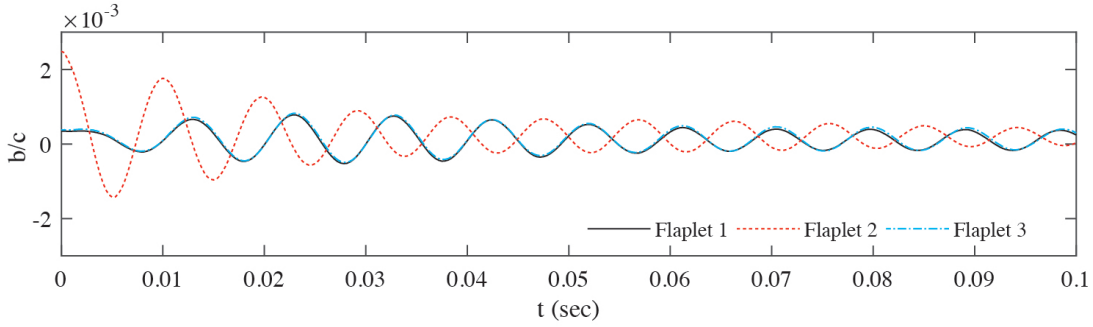
2.3.3 Flaplet Motion

For the motion study, three neighbouring flaplets were analysed in order to distinguish between random motion patterns, representing turbulent structures, or spanwise coherent structures, such as the described rollers convecting along the flaplets. Each flap represents a one-sided clamped rectangular beam which oscillates in the first bending mode perpendicular to the long axis, at the natural frequency when being excited. The motion was recorded and analysed for 2.5 seconds leading to a total of 8000 frames. For further analysis, the flaplet motion has been classed into two different categories, synchronous in-phase (S) motion and anti-synchronous (A-S) motion. The S motion is when all three flaplets are in the same phase, both for positive and negative deflections (see Fig. 2.6a for clarity). A-S motion is defined as when the flaplets have a phase delay of π with respect to each other (see Fig. 2.6b). A small variance of the phase of ±10° is allowed when the time traces are investigated for such events. To investigate the probabilities of whether the flaplets have S or A-S motion the natural frequency of the flaplets, f_1 = 107 Hz, is used to calculate the maximum number of possible 'flap events' in the sampling time, which is 535 over the captured period. Events are only looked at for when the centre flap is at its maximum positive or negative position.

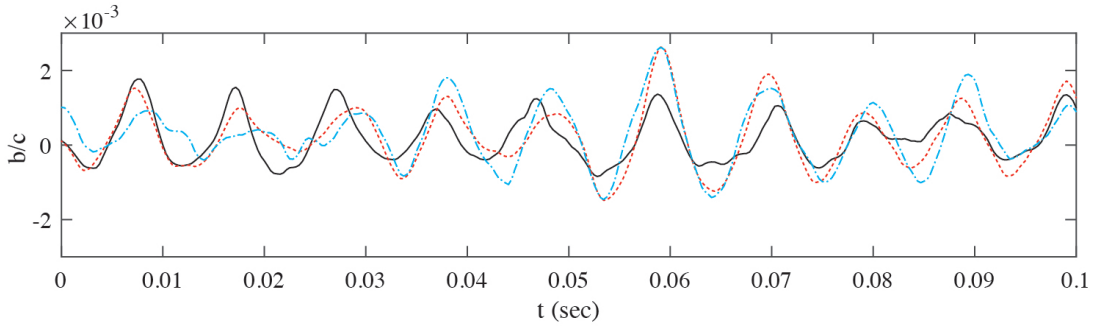
When observing the 10° cases in Table 2.5, it can be seen that the S motion has a significantly higher probability than the A-S motion. This is proposed to be due to the

Test Case	P(S)	P(A-S)
100-0-F	0.104	0.023
150-0-F	0.074	0.036
100-10-F	0.225	0.009
150-10-F	0.162	0.016

Table 2.5: Flaplet motion synchronisation probabilities



(a) Neighbouring flaplet response when only one flatlet, flaplet 2, is subjected to a deflection



(b) Neighbouring flaplet motion measured at the test case 150-10-F

Figure 2.7: Neighbouring flaplet motion

presence of strong spanwise coherent shear layer vortices. One might argue that the observed increase is due to the spanwise mechanical coupling of the flaplets. However as can be seen in Fig. 2.7a, if one flaplet is excited then the neighbouring flaplets are coupled with a phase delay of π, as all flaplets are connected via a base layer. Fig. 2.7b shows that at the test case 150-10-F, the neighbouring flaplets are in phase with each other and have a strong correlation with each other (minimum 0.716). This indicated that a spanwise structure excited all three flaplets at the same time. An interesting observation is that the 100-10-F case had a higher probability of S motion compared to 150-10-F. As the shear layer fundamental frequency close to that of the natural frequency

of the flaplets, it is hypothesised that the lock-in effect is more pronounced. A similar observation was made by Rosti et al. (2017) and hence a similar effect is proposed here. In comparison, for an angle of 0°, the flaplet motion is much more random. This is due to the weaker adverse pressure gradient on the upper side of wing, which reduces the mean shear in the inflection point of the boundary layer. Thus, the motion of the flaplets here is thought to be mainly due to small scale turbulent structures convected downstream and exciting the flaplets in a more random manner.

2.4 Conclusion

Attaching thin flexible flaplets (oscillators) at the trailing edge of an aerofoil - free to oscillate in wall-normal direction - has been seen to have a profound upstream effect on the boundary layer at moderate angles of attack (10°); leading to a stabilisation of the fundamental mode growing in the shear-layer on the suction side, along the second half of the wing. For the plain aerofoil, under the given flow conditions, spanwise coherent rollers are formed in the BL in the linear state and then further downstream the growth of non-linear instabilities leads to pairing of those rollers near the trailing edge. The pairing process is clearly suppressed when the flaplets are attached. They started to oscillate at their fundamental frequency with amplitudes of order of 1 mm (0.5%c), excited by the convection of the rollers over the trailing edge. This observation leads to the conclusion that the stabilisation is due to a resonance or lock-in between the fundamental instability mode and the attached oscillators (flaplets), as this effect is most pronounced when the frequency of the fundamental shear-layer mode is closer to that of the natural frequency of the oscillators, given that the shear-layer is already in its non-linear state. A previous study on bluff body wakes shows a similar stabilisation effect when flexible flaplets, being attached to the aft part, are getting into resonance with the vortex shedding cycle (Kunze and Brücker, 2012). A further consequence of the lock-in stabilisation is the observed reduction in the boundary layer thickness. This is explained by the reduced probability of pairing events, which otherwise are responsible for larger wall-normal momentum exchange and a further thickening of the boundary layer. It is hypothesised therefore that the flaplets have a beneficial effect on the integral

performance of the aerofoil such as reducing drag and increasing lift. This is supported by recent results of active trailing edges oscillators investigated at high frequency Jodin et al. (2018). The present study also supports on physical means the earlier observation of the flaplets causing the dampening of trailing edge noise in the low-frequency range (Kamps et al., 2017). More recent, Talboys, Geyer and Brücker (2018) have carried out an aeroacoustic study with the present configuration and indeed confirmed the reduction of acoustic noise in the low to medium frequency range (100 Hz - 1 kHz).

Compared to the very recent study on high-frequency active oscillating trailing edges Jodin et al. (2018), the present method represent a charming alternative as a passive flow control technique, which does not require sophisticated and costly active manipulation techniques. As shown herein, the flaplets act as self-excited 'pacemakers' to stabilise the shear layer on the suction side and therefore it is reasonable to suggest that they also improve the aerodynamic performance of the aerofoil, besides helping to reduce trailing edge noise as already proven in Talboys, Geyer and Brücker (2018). The natural frequency of these passive oscillators can be tailored for different flow situations either by using different shapes, intelligent materials with temperature or pressure depending properties or by simply applying a deployment strategy where the length of the freely extending tips of the flaplets is varied by sliding the sheet along the trailing edge.

2.5 Critical analysis

2.5.1 Overview and study contributions

The study presents a novel flow-control strategy in the form of passive flexible oscillators attached to the trailing-edge of an aerofoil. This type of flaplets had only been used in a preliminary acoustic study on a NACA0010 (Kamps et al., 2017) or on the aft half of a cylinder looking at the aerodynamics (Kunze and Brücker, 2012) and the aeroacoustics (Kamps et al., 2016; Geyer et al., 2019). Using POD the dynamics of the shear layer rollers could be elucidated showing that the flaplets cause an upstream stabilisation of the shear layer, by locking-in with the fundamental instability of the shear-layer and reducing the probability of pairing events of the roller vortices in the shear layer. Therefore, the action of the flaplets was considered similar to that of a "pacemaker",

which has its own dominant frequency (1st bending mode Eigen frequency) and which is driving the stabilisation process by interaction of the mechanical oscillations with the fluid-dynamical instabilities.

2.5.2 Limitations of the working hypothesis

The study was focusing in the initial tests of the flaplets on a specific range of Reynolds-number and angles of attack, therefore it could be explored further if the hypothesis holds also for an extended parameter space of larger range of Re_c and α. As discussed by Huang and Lin (1995), there are different vortex shedding modes of an aerofoil; laminar, sub-critical, transitional and turbulent. It was seen that when the vortex shedding was in the laminar or sub-critical state there were no nonlinear instabilities in the shear layer. As such if the Reynolds number were such that the vortex shedding was in a linear state the flaplets would not be effective at stabilising the instabilities, purely due to the fact that there is not enough energy in any nonlinear excitation processes yet to generate frequencies to stabilise. This is hypothesised as to what was observed seen in the study at $Re_c = 100,000$ where no dominant vortex pairing was observed in the shear layer. This is also the case when the angle was at $\alpha = 0°$. As the vortex shedding goes into the transitional state, the non-linear instabilities start to occur, seen as vortex pairing (sub-harmonic instabilities). This is observed in the study for the conditions at $Re_c = 150,000$ at $\alpha = 10°$, where the adverse pressure gradient is increased. Therefore it can be assumed that if the Reynolds number is increased further, the flaplets will continue to stabilise the shear-layer. However, this observation also suggests that there exist a critical point below which the flaplets are not effective in stabilising the flow. As will be discussed in Chapter 4, the flaplets can also go into flutter under certain conditions which is also limiting the practical use of the flaplets; however the observed Reynolds number for this happening are significantly higher than the ones testing herein.

Another possible factor is the existence of a laminar separation bubble on the airfoil, which may effect the instability scenario and the stabilisation hitherto. Yarusevych, Sullivan and Kawall (2009) stated that if there is a separation bubble forming on the surface of the aerofoil the sub-harmonic instability in the shear-layer is less pronounced.

Therefore, if using a non-tripped aerofoil the effect of the stabilisation effect could be less pronounced compared to the situation of a tripped one. This also indicates that if a different aerofoil was used, one with a higher adverse pressure gradient, such as a thicker aerofoil in the NACA 00xx series, the effect of the flaplets might also be more suppressed as the separation bubble would be stronger.

2.5.3 Other aerofoil profiles

A key concern is whether the effects observed by adding the flaplets to the aerofoil are only achieved on a NACA 0012 aerofoil. There have been studies recently that use similar trailing edge modifications using different aerofoil profiles, which show promising results. Simiriotis et al. (2019) used a sub-critical Airbus A320 aerofoil profile where the trailing edge consists of piezo-electric elements that can oscillate at specified frequencies and amplitudes. The amplitude and frequency of their elements were similar to those in this study. With the use of PIV measurements in the wake they showed a modification of the shed vortices leading to reduced drag. Yu and Yang (2020) carried out a CFD simulation using a S833 aerofoil profile with passive 'flapping trailing edge fringes'. They also found that the shed vorticies could be altered and which resulted in a reduction in drag. Although they did not look at the shear-layer stabilisation effect that was observed within this study, they did show that regardless of the aerofoil profile, flaplets do have a positive impact on the aerofoil performance.

2.5.4 Mechanical coupling of flaplets

As was mentioned in §2.3.3, the flaplets were observed to be mechanically coupled. This mechanical coupling was not intended by design. However, due to the manufacturing process of cutting the flaplets out of a single sheet of polyester, where the roots of the flaplets are all connected to the same sheet, the coupling exists. To investigate if such a mechanical coupling may occur per design, a modal simulation was carried out using ANSYS. First the material properties that have been obtained in Table 2.3, were put into the software and the frequency of the first mode was verified. Where the measured first bending mode was $f_1 = 107$ Hz and the simulated first bending

mode was seen to be $f_1 = 110$ Hz, therefore the modal analysis can accurately depict the bending modes of the flaplets.

Figure 2.8 shows the result of the modal analysis, where the first bending mode is activated at two time steps; (a) is at the peak deflection of the centre flaplet and (b) when the centre flaplet is at the opposite peak deflection. The contours of Fig. 2.8 shows levels of von-Mises stress, the values of which are not important as the model analysis package only gives an idea of the relative stress distribution rather than the actual value of the stress. It can be seen that the flaplets have a large stress concentration by the corners of the roots, this is a natural point of stress concentration due to the sharp corner. But crucially it can be seen that the stress path of each flaplet is connected together, hence coupling all the flaplets together in an anti-synchronous motion.

The question here is, to what extent does this anti-phase mechanical coupling contribute to the overall performance of the stabilisation effect of the flaplets. On one hand, it could be beneficial to have asynchronous flaplet motion in the way that they could break-up the spanwise rollers in a similar way as saw-tooth serrations do. Therefore the described forcing of anti-phasic coupling - although not intended initially - could be seen as another way of passive flow control with the effect to destroy the coherence of the shed rollers. Hence some additional energy needs to be taken from the flow to overcome this natural mechanical behavior, which is then fed back into the flow by the neighbouring flap moving in an out-of-phase manner. A simple test with different flaplet designs could finally give an answer whether this is of additional benefit. It could be done by comparing the present results with flaplets of the same geometry but being all individual elements. From a practical view point, this implementation could be difficult to bring the whole array of elements in equispaced arrangement for spanwise uniformity. A solution could be to have the placement of the flaplets upon the chord line of the symmetric aerofoil (i.e. along the centre line of the aerofoil) and to be extended out the trailing edge and long enough such that the mechanical coupling by the stress paths at the roots of the flaplets does not effect the motion.

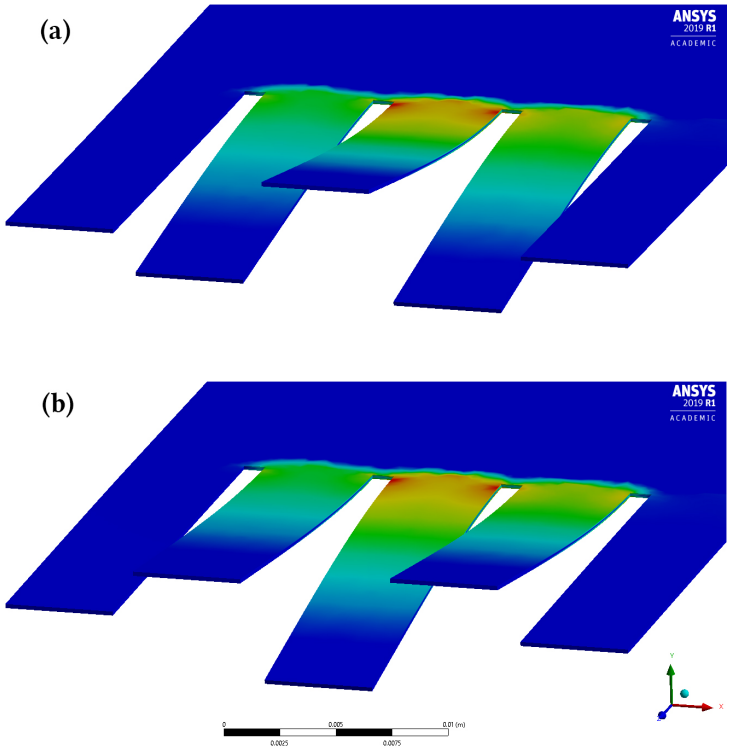


Figure 2.8: ANSYS simulation of flaplet motion

2.5.5 Tracking of flaplets

The tracking of the flaplets was subject to some difficulty with the current arrangement. As was mentioned in §2.2.2, an optical lever arm approach was used to visualise the flaplets motion by the scattering of the light onto a translucent screen, which was then recorded. The quality of the resulting images did pose some difficulty when it came to the analysis of the flaplets motion. Therefore edge filters had to be used. Figure 2.9a, is the raw image directly from the high speed camera, and Fig. 2.9b is the image once the edge filter is applied to the image. As it can be seen, once the filter is applied the tips of the flaplets end up with a black region which can be processed much easier with a Matlab code. Once the edges were located, the edges were tracked frame on frame, the resulting tip location can be seen in Fig. 2.9b as white dots. Only these three flaplets were tracked for this study and this was due to a very small step at the junction of the 3D printed and perspex section of the aerofoil. Due to the amplification effect that is caused by the optical lever, the reflected light was substantially effected and could give

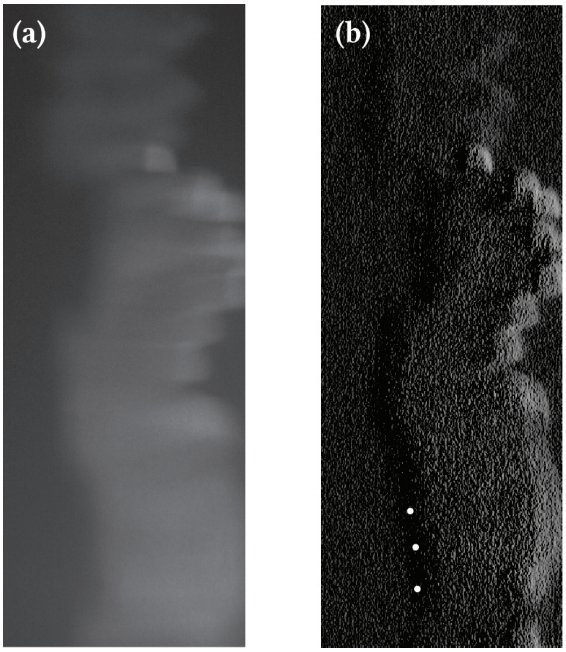
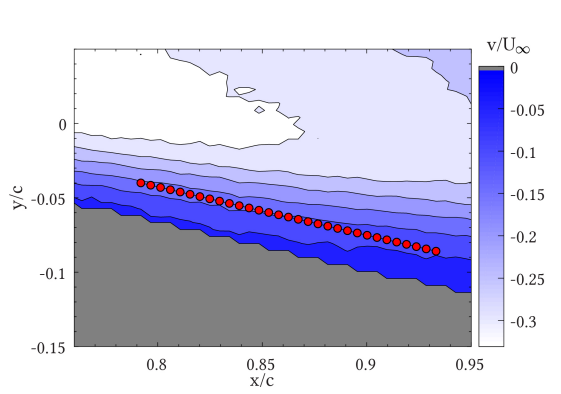


Figure 2.9: Flaplet tracking, (a) is the raw image and (b) is the enhanced image with the three tracked flaplets indicated with a white dot.

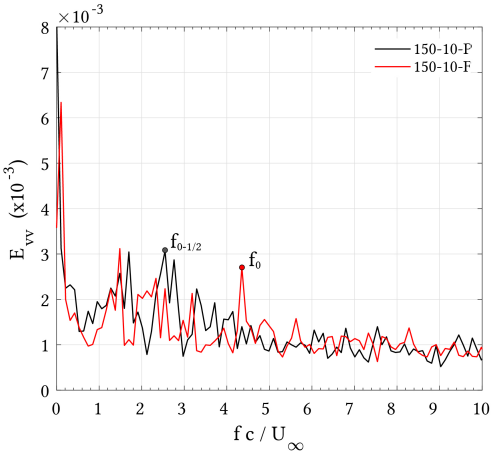
potential errors. So the three flaplets used were well away from this affected zone, to ensure no errors were made when tracking the flaplets.

2.5.6 Chordwise sensitivity

In this study the analysis of the non-linear boundary layer effects were done only at one selected chordwise location, however the variation of the fundamental instability in the boundary with the chordwise position should be studied further to understand how far upstream of the trailing edge such instabilities occur. Figure 2.10a, shows the contour of the averaged v/U_∞ flow field with the 31 additional probe locations (points in red) within the boundary layer. These additional points have a chordwise spacing of 0.005c and the wall normal height is the same as presented in the publication (δ^*/c). The resulting FFT can be seen in Fig. 2.10b, where the black line represents the plain aerofoil and the red shows the aerofoil with the flaplets attached. What can be instantly seen is that the fundamental instability, f_0, peak is clearly observed in the flaplet case whereas it is not seen in the plain case. However, in the latter the $f_{0-1/2}$ peak is clearly visible. This is a proof that the effect is visible also at other chordwise locations.



(a) Contour plot of the v/U_∞ and the additional probe points.



(b) Average spectra of the additional probe points.

Figure 2.10: Chordwise sensitivity of the shear-layer stabilisation effect.

2.5.7 Uncertainty of the High-Speed PIV measurements

Within Digital Particle Image Velocimetry (DPIV) measurements, there are three main areas contributing to the overall measurement uncertainty: 1) particle size effects, 2) sub pixel accuracy, 3) averaging effects within the interrogation region. The particles were 1 μm in diameter (as per particle generator specification, TSI 9307-6). The Stokes number (S_k) relates the particle to how well it can be advected through the domain. If $S_k < 0.1$ the error in the tracing accuracy is lower than 1%. For the current study, $S_k = 0.00015$ so the particles follow the flow with very good accuracy. In addition, because of their small size the particles settling velocity due to gravity effects is negligible (Sataloff, Johns and Kost, 2007).

For the current set-up the scale factor was calculated, with a calibration slide, to be 8.5 px per mm. Therefore one pixel corresponds to a length scale of 0.12 mm or 120 μm in the measurement plane. As a practical guidance, a minimum resolution of the displacement measurements can be achieved to a shift of 0.05 px, using a Gaussian sub-pixel analysis of the peak in the correlation plane (Raffel, Willert and Kompenhans, 1998). With the given time-separation of 0.08 ms and 0.03 ms between the double pairs, the uncertainty in the velocity measurements is 0.075 m/s and 0.2 m/s. This is about 0.9% and 1.7% percent of the mean velocity in the wind-tunnel experiments, respectively for the $\mathrm{Re_c} = 100,000$ and $150,000$ cases.

When looking at the averaging effects of the interrogation window, the size of the window is key. The windows used here were initially 32 x 32 pixel, which corresponds to a window of 3.76 x 3.76 mm. It is then reduced to a 16 x 16 pixel window size for the second pass (corresponding to 1.88 x 1.88 mm). In principle it would be advantageous to keep the window size as small as possible however if the window size becomes too small, then there could be too much in-plane pair loss i.e. not enough particles to obtain a good peak in the correlation plane, increasing the risk to produce erroneous vectors. Conversely, if the windows are too big then there will be significant averaging of the particles displacement, as such, flow details on smaller scale will be lost. Therefore, the final size of 16 x 16 pixel is a good compromise in practical High-Speed PIV. Better resolution is only possible with either a camera with super-resolution Mega-Pixel sensors or increasing the magnification with higher lens magnification in the field of view. Both solutions were not readily available with the given equipment.

2.5.8 Future work

For future work there are some interesting extensions of the project that could be further investigated.

2.5.8.1 Piezoelectric flaplets

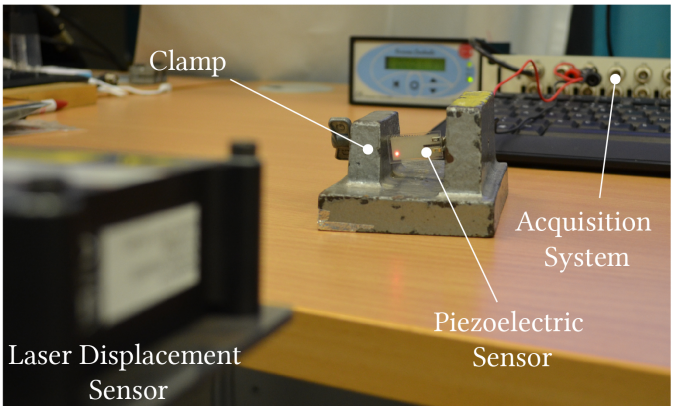
Flaps made of piezoelectric material could be used, as explained herein as a demonstrator. Such material is typically used for measuring vibrations in various applications however, their output voltage could be used also for energy harvesting. Fig.2.11a shows a demonstrator of a single piezoelectric flaplet which is crudely connected to LabVIEW such that the principle of operation can be demonstrated herein. In order to validate the signal that was obtain from the piezoelectric flaplets, a laser displacement sensor was used to measure the tip vibration of the flaplets. The response of the flaplet was measured at a frequency $f = 2$ kHz by LabVIEW and the laser displacement sensor was set at a measurement rate $f = 5$ kHz. A small fan, which had an approximate wind velocity of $u = 3$ m/s at the flaplet, was used to excite the flaplet. The fan was run for 60 seconds, whilst the two measurement systems captured the data. The response of

the two measurement techniques can be seen in Fig. 2.11b, where the black solid line is the output of the piezoelectric flaplet itself and the red dashed line is the output of the laser displacement sensor. Firstly, it can be seen that there is a peak in the spectrum at $f = 160$ Hz, which is assumed to be the fundamental bending mode of this type of flaplet. The predominant peak at $f = 50$ Hz stems from electrical mains noise, which can be removed with the use of a more sophisticated circuit rather than the rudimentary set-up used for this demonstrator. Overall, this simple piezoelectric flaplet shows that it can provide similar quality of vibrational motion data as the laser displacement sensor. This demonstrator can then be easily scaled up where ultimately the whole span of the aerofoil can be equipped with piezoelectric flaplet sensors which can be connected to a micro-controller and therefore a live view of the flaplets and their oscillation can be tracked in real time. This technique would also be a perfect way to see how the flaplets interact with each other across large span distances. It should also be noted here that the flaplets would not be mechanically coupled, hence any effects that occurred due to this coupling would be eliminated.

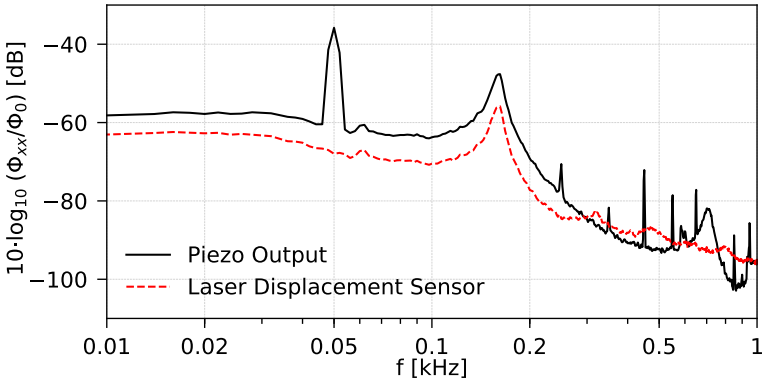
2.5.8.2 Additional measurements

To get a more global view of how the flaplets affect the flow, additional High-Speed PIV measurements should be undertaken. These measurements should be now focused on the wake, and the modification of the wake. It has been seen in other publications that an active trailing edge oscillator (Jodin et al., 2017; Simiriotis et al., 2019) can modify the wake significantly. In these publications, the trailing edge oscillates at similar frequencies and amplitudes as the ones used here. It was seen that the small vibrations cause a vortex breakdown for the largest structures in the flow, a reduction in pressure drag and an increase in overall lift.

If the measurements were to be carried out again, in order to get better statistics for the spectra, more frames should be captured in the DPIV measurement. The limiting factor here was the low amount of Random Access Memory (RAM) on the computer used for the measurements. Therefore an increase in the RAM of the system would immediately circumnavigate this problem. Saying this, looking at the ‘convergence’



(a) Photograph of the demonstration model, wired to the data acquisition system, and simultaneously measured with a laser displacement sensor. Note the fan used to excite the piezoelectric sensor is not in the image.



(b) FFT of the piezoelectric flaplets and the laser displacement sensor

Figure 2.11: A working demonstrator model of the piezoelectric flaplet and the comparison of the FFT response with a laser displacement sensor.

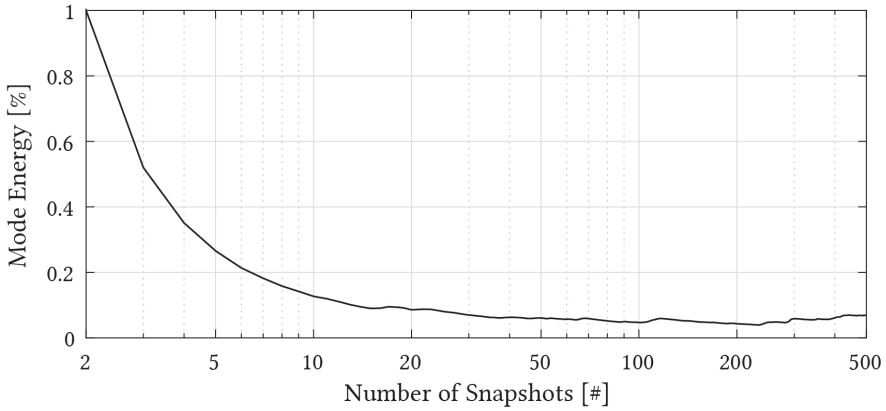


Figure 2.12: Convergence of 'mode energy' for the 1st POD mode for the case 150-10-P.

of the 1st POD mode in Fig. 2.12, it can be seen that the statistics for the POD mode converged at around 100 snapshots. So there is confidence in the presented results, the additional measurements would just amplify the effect providing further clarity.

In addition to the PIV measurements aerodynamic force measurements should be carried to quantify the aerodynamics in a more global sense. From this study, it was inferred that the flaplets reduce the pressure drag as the boundary layer was seen to be thinner. The lift can be assumed to be increased due to the flow modification in a similar manner as Jodin et al. (2017).

3

Paper 2: An aeroacoustic investigation into the effect of self-oscillating trailing edge flaplets

Contents

3.1 Introduction 40
3.2 Experimental Arrangement 43
3.3 Results 47
3.3.1 Theoretical Comparison 47
3.3.2 Single Microphone Measurements 49
3.3.3 Linear stability analysis 52
3.3.4 Overall sound pressure level measurements 54
3.3.5 Aerodynamic force measurements 56
3.3.6 Hot wire anemometry 57
3.4 Conclusion 60
3.5 Critical analysis 61
3.5.1 Overview and study contributions 61
3.5.2 Open jet considerations 62
3.5.3 Calibration of measurement systems 63
3.5.4 Simulation for lift and drag coefficients 67
3.5.5 Background noise 68
3.5.6 N-factor sensitivity 69
3.5.7 Separation bubble prediction 70
3.5.8 Future work 70

Abstract

The aeroacoustics of a NACA 0012 aerofoil with an array of self-oscillating flexible flaplets attached to the trailing edge has been investigated at low to moderate chord based Reynolds number (50,000 – 350,000) and at geometric angles of attack from $\alpha_g = 0°$ – 20°. Two distinct situations were tested: one in which the flaplets were attached to the pressure side, tangentially extending the surface down the trailing edge; the other is with the flaplets attached to the suction side and extending this surface, respectively. For the reference aerofoil, strong tonal peaks are observed. When the passive flaplets are attached to the pressure side, these tonal peaks are removed and the overall sound pressure level (OSPL) is reduced by up to 20 dB. If the flaplets are placed on the suction side, the noise reduction is still present but not as strong as compared to the other case. It is concluded that the case with flaplets on the pressure side is more beneficial in interrupting the feedback loop between the boundary layer instabilities and noise sources in the wake as it is seemingly modifying the laminar separation bubble situated on the pressure side of the aerofoil, the major tonal noise source. The somewhat lower overall noise reduction obtained by the case with flaplets attached on the suction side is suggested to result from the upstream stabilisation in the boundary layer on the suction side by the mechanism of lock-in as show in a recent paper by Talboys and Brücker (2018).

3.1 Introduction

Aerofoil self-noise reduction is a topic which is attracting increasing interest due to the growing need and desire for ‘quieter’ aerofoils for various engineering applications. The main source of this self-noise is the boundary layer – trailing edge interaction. Therefore various strategies have been proposed by engineers in recent years to mitigate this.

For moderate Reynolds numbers, when the boundary layer flow along the aerofoil is still in the laminar state, a strong tonal noise is present. As such is especially annoying for the human hearing spectrum, a significant amount of research has been carried out in order to try to understand this phenomenon. The first detailed study of this tonal

noise was done by Paterson et al. (1972). Their observations show that the main tonal peak frequency initially scales with the freestream velocity $U_\infty^{0.8}$ until sudden jumps to higher frequencies are observed, which is commonly referred to as 'laddering'. If those 'laddering' events are averaged out over a large frequency range, the scaling changes to $U_\infty^{1.5}$. Tam (1974) built off these results and proposed an aeroacoustic interaction between instabilities in the boundary layer of the aerofoil and noise sources situated in the wake, which self-enforce as a feedback loop. Arbey and Bataille (1983) then expanded on Tam's feedback model by showing that indeed Tollmien-Schlichting (T-S) waves in the boundary layer initiate the feedback when defracting at the trailing edge. There they create acoustic waves, which back-scatter upstream and feed the loop. This conclusion initiated more detailed investigations into the flow field around the aerofoil. Lowson, Fiddes and Nash (1994) and McAlpine, Nash and Lowson (1999) showed that the tonal noise is governed by the presence of a laminar separation bubble on the pressure side of the aerofoil and that the frequency of the tonal noise is the most amplified frequency in the boundary layer by using linear stability theory. Desquesnes, Terracol and Sagaut (2007) carried out the first direct numerical simulation (DNS) on the tonal noise issue and they found that another feedback loop co-exists with the previously described one, which originates from the instabilities on the suction side of the aerofoil. This feedback was then thought to modulate the discrete frequencies which are evenly spaced around the main tonal peak. Pröbsting, Scarano and Morris (2015) later showed that one of the two co-existing feedback mechanisms dominates the overall sound pressure level, of which depends on the Reynolds-number range. This conclusion was achieved by simultaneous measurements of the flow field by Particle Image Velocimetry (PIV) and the acoustic field with microphone-arrays. Their results show that the tonal noise generation at very low chord based Reynolds numbers (Re_c = 30,000) is controlled by the suction side, while at higher Reynolds numbers (Re_c = 230,000) it is dominated by the pressure side. By tripping either side of the aerofoil separately, it is demonstrated that both feedback loops can exist independently (Desquesnes, Terracol and Sagaut, 2007).

Many different techniques have been investigated to mitigate boundary-layer trailing edge noise generation, most of which are inspired from the well-known 'silent' flight

of the owl. Geyer, Sarradj and Fritzsche (2010) investigated a wide range of aerofoils with different porosities, inspired from the 'soft downy feathers' of the owl. Even a small porosity showed already an aeroacoustic benefit in the low to mid frequency range, of which effect increases with increasing porosity, even in some cases reaching up to 10 dB broadband noise reduction. However, this came with a penalty of noise increase in the high frequency range originating from the modified surface roughness of the aerofoil. In addition, both lift and drag forces were negatively effected compared to the non porous aerofoil.

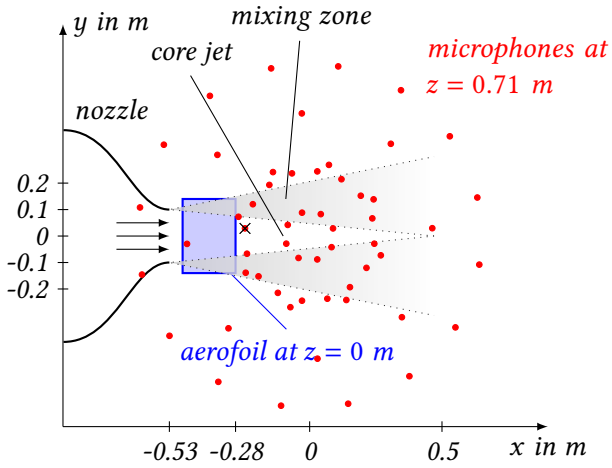
Another owl-inspired technique uses trailing edge brushes or serrations, mimicking the characteristic trailing edge structure formed by the feathers of owls. Brushes were observed to reduce noise in the high-frequency range 2–16 kHz (Herr, 2007), probably affecting mostly the broadband noise of the turbulent boundary layer interacting with the trailing edge. Finez et al. (2010) could show that the spanwise coherence of the shed vorticies in the wake behind the trailing edge is reduced by 25% in the presence of brushes. Serrations have been extensively researched in both the laminar boundary layer case (Chong, Joseph and Gruber, 2010) and turbulent boundary layer case (Arce León et al., 2017). Their mechanism in noise reduction is - similar to the brushes - through the reduction of spanwise coherence in the shed vortices. Studies with a single flexible flap at the trailing edge were investigated by Schlanderer and Sandberg (2013). They carried out a DNS study on a flat plate with an elastic compliant trailing edge and found an aeroacoustic benefit at low and medium frequencies with an increased noise level at the Eigen frequency of the material. These results were confirmed later by Das et al. (2015) in an experimental investigation using a similar arrangement to Schlanderer and Sandberg (2013). Active oscillations of a trailing edge flap were studied by Jodin et al. (2018). Their investigation was focused on the wake structure and it was observed that the wake could be reduced in thickness by as much as 10%.

In the present study, a novel configuration of a flexible trailing edge is used, consisting of an array of individual elastic flaplets mimicking the tips of bird feathers aligned along the span of the wing. This type of trailing edge modification with arrays of individual mechanical oscillators in form of elastic flaps has thus far only studied by the authors

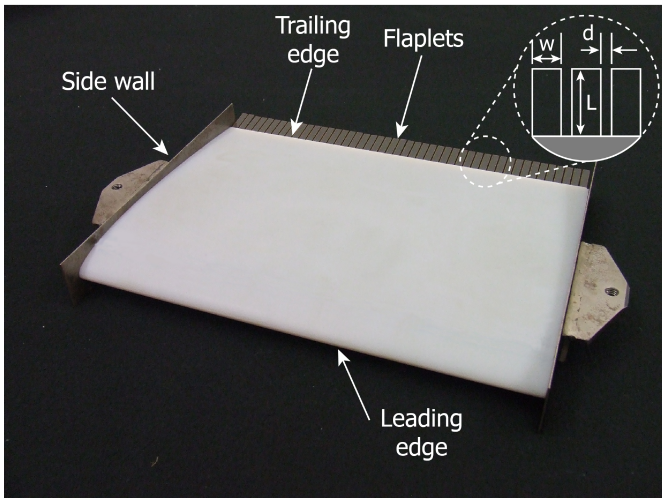
(Kamps et al. (2016), Kamps et al. (2017) and Geyer and Sarradj (2019)). Attached to the trailing edge of a NACA 0010 aerofoil, the rows of individual silicone flaplets clearly showed a reduction in tonal noise (Kamps et al. (2017)). A follow-up study on the flow modification by this type of trailing edge was done by Talboys and Brücker (2018) and demonstrated aerodynamic advantages as well. Detailed High-Speed PIV measurements, coupled with simultaneous motion recordings of the flap tips, prove a stabilisation mechanism of the flaps on the boundary layer on the suction side. A lock-in was triggered by tuning the fundamental frequency of the structural bending mode of the oscillator to match with the fundamental frequency of the shear-layer on the suction side, forming regular vortex rollers in the boundary layer. This lock-in delays the growth of non-linear instabilities such as the merging of the rollers, beneficially affecting also the overall aerodynamic performance. The present study builds on this previous work in order to provide a more in-depth aeroacoustic analysis on the benefits of such self-oscillating flaplets at the trailing edge. In addition, hot wire measurements of the turbulent velocity fluctuations in the wake of the airfoils provide insight into the effect of the flaplets on the flow field.

3.2 Experimental Arrangement

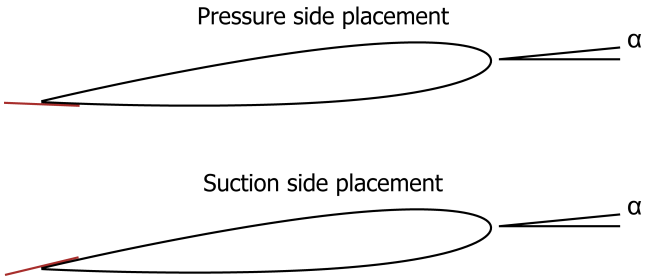
The aerofoil used for the present study was a NACA 0012, with a chord (c) of 0.2 m and a span (s) of 0.28 m. The model was 3D printed giving the aerofoil a trailing edge bluntness of 0.5 mm with a solid angle of 16°. The flexible trailing edge flaplets were manufactured, using a laser cutter, from a thin polyester film (see table 3.1 for dimensions and material properties). The flaplets were attached to the aerofoil using a thin strip of double sided tape, and placed such that the free ends were orientated downstream at $1.1c$, allowing them to freely oscillate at their Eigen frequency in the flow field. The Eigen frequency was determined to be 107 Hz in a previous study (Talboys and Brücker, 2018), using cantilever beam theory. The flaplets were placed on both sides of the aerofoil, separately, in order to observe if the there is any effect depending on whether the flaplets were orientated tangentially with the pressure or suction side.



(a) Schematic display of the measurement setup (top view, × marks the location of the single microphone)



(b) Photo of the NACA 0012 aerofoil with the flaplets adhered on the trailing edge.



(c) Showing the two different flaplet placements at an angle of incidence, α. Pressure side placement (top) and suction side placement (bottom)

Figure 3.1: Experimental set-up

Length (L)	Width (w)	Inter spacing (d)	Thickness	Density	Young's Modulus	Eigen frequency
20 mm	5 mm	1 mm	180 μm	1440 kg/m^3	3.12 GPa	107 Hz

Table 3.1: Flaplet Dimension and Material Properties

The acoustic and hot wire anemometery (HWA) measurements took place in the small aeroacoustic open jet wind tunnel (Sarradj et al., 2009) at the Brandenburg University of Technology in Cottbus, with a setup similar to that used in Geyer, Sarradj and Fritzsche (2010). The wind tunnel was equipped with a circular nozzle with a contraction ratio of 16 and an exit diameter D = 0.2 m. With this nozzle, the maximum flow speed is in the order of 90 m/s and at 50 m/s, the turbulence intensity in front of the nozzle is below 0.1 %. For the present study the chord based Reynolds number was varied from 50,000 – 350,000 and the geometric angle of attack, α_g, was varied from $\alpha_g = 0°$ to 20°. As the wind tunnel is open jet, a correction factor is commonly applied to the angle of attack. This correction factor was introduced by Brooks, Marcolini and Pope (1986) who used lifting line theory to account for the deflection induced by the open jet boundary conditions. However due to the small jet width to aerofoil chord ratio ($D/c \sim 1$), the correction factor should be used with caution (Moreau et al., 2003) and as such has not been used to indicate the angle in the present study. All angles, unless otherwise stated, are therefore the geometric angles of attack (α_g). During measurements, the wind tunnel test section is surrounded by a chamber with absorbing walls on three sides, which lead to a quasi anechoic environment for frequencies above 125 Hz. Here it should be noted that the aspect ratio of the aerofoil is low, as such a question is raised on the two dimensionality of the flow on the aerofoil. However, when looking at an oil flow-visualisation taken in §4 (Fig. 4.5) it can be seen that in the mid span section of the aerofoil, the flow is indeed two dimensional.

For the measurements, the aerofoil was positioned at a distance of 0.05 m downstream of the nozzle. The tips of the aerofoil were attached to a six component wind tunnel balance to simultaneously measure the integral aerodynamic forces. Since the span of the aerofoil (s = 0.28 m) exceeded the nozzle diameter, no aerodynamic noise was generated at the tips or the lateral mountings. A schematic of the setup is shown in Fig. 3.1a.

The acoustic measurements were performed using a planar microphone array, consisting of 56 1/4th inch microphone capsules flush mounted into an aluminium plate with dimensions of 1.5 m × 1.5 m (see Sarradj (2010)). The microphone layout is included in Fig. 3.1a. The aperture of the array is 1.3 m. The array was positioned out of the flow, in a distance of 0.71 m above the aerofoil.

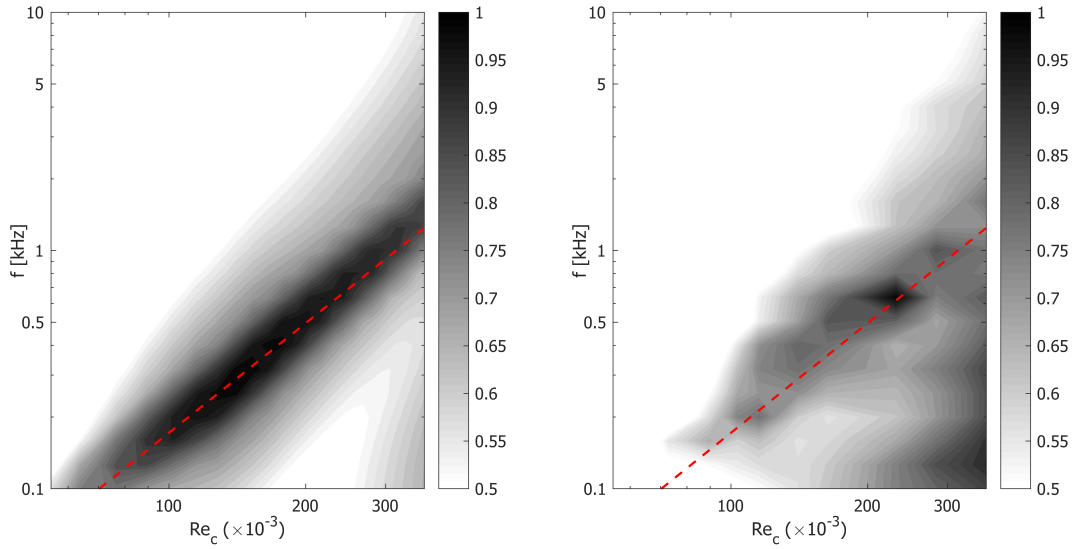
Data from the 56 microphones were recorded with a sampling frequency of 51.2 kHz and a duration of 60 s using a National Instruments 24 Bit multichannel measurement system. To account for the refraction of sound at the wind tunnel shear layer, a correction method was applied that is based on ray tracing (Sarradj (2017)). In post processing, the time signals were transferred to the frequency domain using a Fast Fourier Transformation (Welch's method, Welch (1967)), which was done blockwise on Hanning-windowed blocks with a size of 16384 samples and 50 % overlap. This lead to a small frequency spacing of only 3.125 Hz. The resulting microphone auto spectra and cross spectra were averaged to yield the cross spectral matrix. This matrix was further processed using the CLEAN-SC deconvolution beamforming algorithm proposed by Sijtsma (2007), which was applied to a two-dimensional focus grid parallel to the array and aligned with the aerofoil. The grid has a streamwise extent of 0.5 m, a spanwise extent of 0.4 m and an increment of 0.005 m. The outcome of the beamforming algorithm is a two-dimensional map of noise source contributions from each grid point, a so-called sound map. In order to obtain spectra of the noise generated by the interaction of the turbulent boundary layer with the trailing edge of the aerofoil, a sector was defined that only contains the noise source of interest. The chosen sector has a chordwise extent of 0.2 m and a spanwise extent of 0.1 m. Thus, spectra of the noise generated by this mechanism are derived by integrating all noise contributions from within this sector, while all potential background noise sources (such as the wind tunnel nozzle or the aerofoil leading edge) are excluded from the integration. The resulting sound pressures were then converted to sound pressure levels L_p *re* 20 μPa and 6 dB were subtracted to account for the reflection at the rigid microphone array plate. In addition to the beamforming results, auto spectra of a single array microphone close to the aerofoil trailing edge were analysed. The microphone position is highlighted in Fig.3.1a.

The HWA measurements were taken in separate experiments to the acoustic measurements, to insure no additional noise from the HWA and associated traverse system was measured in the acoustic spectra. The probe used was a Dantec X wire probe (55P64), where the data was taken at a sampling frequency of 25.6 kHz. The Dantec HWA hardware system used for the measurements contains an electronic low-pass filter with a cut-off frequency of 10 kHz. The wake profiles were initiated at $0.25c$ above the aerofoil till $0.25c$ below the aerofoil, at a distance of $0.25c$ from the solid aerofoil edge approximately at mid span. The increment of the measurements was large in the freestream region (1 mm), and then the increment was systematically reduced such that the region of the boundary layer was measured with 0.2 mm increments. Each measurement was taken for a period of 10 sec, prior to moving on to the next increment. Longer measurements were taken, directly behind the trailing edge such that the spectra of the turbulent velocity fluctuations of the wake could be analysed. The measurement period for these measurements was 60 sec. These measurements were converted to the frequency domain using Welch's method, which was done on rectangular windowed blocks of 65536 samples with an overlap of 50 %, leading to a frequency spacing of 0.39 Hz. Even though an X wire probe was used, only the u velocity component was used throughout this study.

3.3 Results

3.3.1 Theoretical Comparison

Brooks, Pope and Marcolini (BPM) (Brooks, Pope and Marcolini, 1989) created a semi-empirical model that aims to predict the aerofoil self-generated noise by breaking it down into five main components; laminar boundary layer – trailing edge interaction (LBL–TE), turbulent boundary layer – trailing edge interaction (TBL–TE, both on suction and pressure sides), separated flow noise, trailing edge bluntness and tip vortex noise. As the aerofoil used in the present study is bounded by two end plates, the tip vortex noise is not considered. In order to use this model to predict and analyse the noise sources the open source software, NAFNoise (Moriarty, 2005), was used. NAFNoise uses a panel method, Xfoil, to calculate the necessary boundary layer parameters for the model and has an



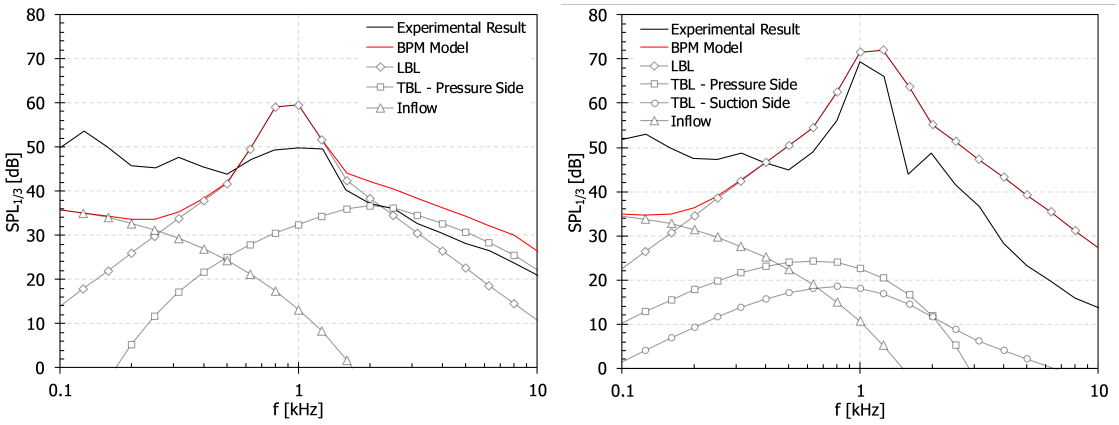
(a) BPM Empirical Model **(b)** Single microphone experimental result

Figure 3.2: Contours of normalised third octave band SPL across the Reynolds number range studied at $\alpha_g = 0°$. The contours are normalised by their respective maximum SPL. The ---- shows the $\sim Re_c^{1.5}$ trend line observed by Paterson et al. (1972)

additional feature which uses a simplified version of the Guidati model, to calculate the additional noise induced from a turbulent inlet flow. As mention in Section 3.2, the inflow turbulence is low for the present experimental set-up; nonetheless this has still been accounted for in the prediction.

Figure 3.2 shows the comparison of the BPM model with the reference experimental results at $\alpha_g = 0°$, for all of the Reynolds numbers tested. The contours have been normalised by their respective maximum SPL in order to compare the overall trends. Immediately it can be seen that in Fig. 3.2a, there is a clear trend of increasing tonal peak with Reynolds number. This trend corresponds well with the empirical $\mathrm{Re_c^{1.5}}$ scaling from Paterson et al. (1972). As the results from the BPM model are in third octave bands, the 'laddering' effect, which scales as $\mathrm{Re_c^{0.8}}$, cannot be seen and only the average effect is observed. In the experimental results, Fig. 3.2b, the trend is also clearly visible and hence the BPM model can be used for the current experimental set-up over a wide range of Reynolds numbers to help to understand the noise sources.

Fig. 3.3 shows the BPM prediction against the experimental results for the baseline case and both of the flaplet orientation cases for one Reynolds number, 300,000 and



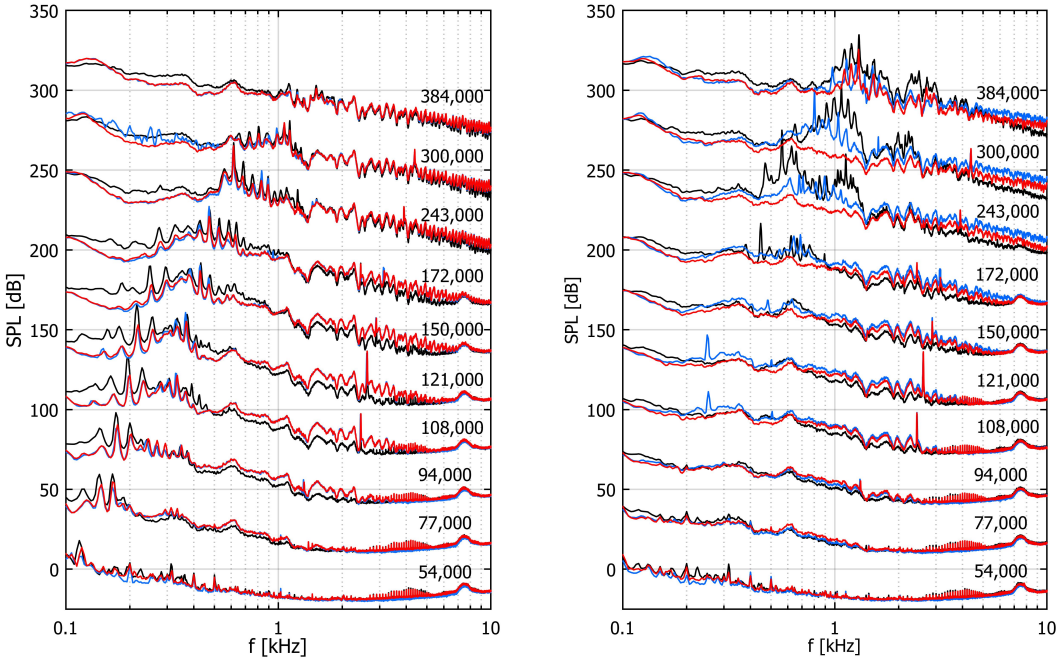
(a) $\alpha_g = 0°$ **(b)** $\alpha_g = 10°$

Figure 3.3: Comparison of the third octave sound pressure level ($SPL_{1/3}$) at Re_c = 300,000 between experimental result and the BPM prediction model. Where the BPM model is the summation of the laminar boundary layer (LBL) noise, both the pressure and suction side turbulent boundary layer (TBL) noise and the turbulent inflow noise.

at two different geometric angles of attack. In general the BPM model can predict the frequency of the tonal peak at both angles of attack well, however the magnitude is over predicted. The LBL-TE noise is the dominating source in both cases, which is to be expected as transition is not forced. In the 0° case (Fig. 3.3a), it can be seen that in the higher frequency range the pressure/suction side TBL (only the pressure side TBL has been plotted in Fig. 3.3a) becomes the dominating noise source, but the influence on the overall noise level is small in relation to the LBL-TE tonal peak. As the angle increases, Fig. 3.3b, the predicted tonal peak also increases in amplitude and the turbulent noise sources no longer affect the predicted spectra.

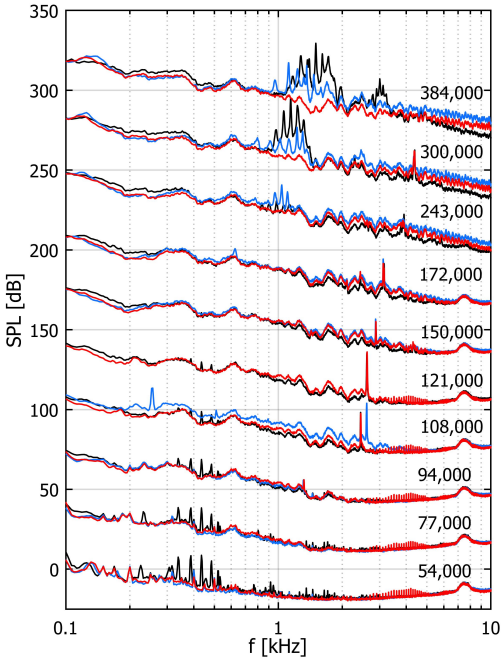
3.3.2 Single Microphone Measurements

Fig. 3.4 shows the single microphone measurements from the microphone situated vertically above the trailing edge, see Fig. 3.1a. For clarity, each Reynolds number test is spaced with an increment of 30 dB from the previous test case, their corresponding Reynolds number is labeled next to each group of spectra. At zero incidence, Fig. 3.4a, it can be seen that for all Reynolds numbers a tonal peak can be observed. An interesting observation can be seen in the low frequency range (0.1 kHz – 0.4 kHz) where there is a significant reduction in the noise level across all cases once the flaplets are applied.

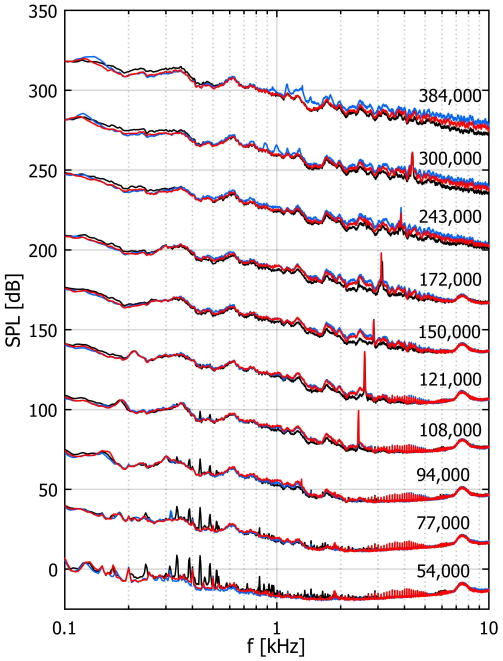


(a) $\alpha_g = 0°$

(b) $\alpha_g = 10°$



(c) $\alpha_g = 15°$



(d) $\alpha_g = 20°$

Figure 3.4: Single microphone measurements for each Reynolds number case, are spaced with 30dB increments for clarity. Each of the angles stated are the geometric angles of attack. For each angle and Reynolds number there are three test cases: a baseline case with no flaplets (—), the case where the flaplets are affixed to the pressure side (—) and when the flaplets are affixed onto the suction side (—).

There is no preference in the surface placement of the flaplets. However, this is expected due to the symmetry of the aerofoil at $\alpha_g = 0°$. The reduction that is seen is thought to be related to the vortex shedding noise which is changed due to the flaplets modifying the wake. This reduction of vortex shedding noise has been observed on a cylinder with flexible elements on the aft half of the cylinder (Kamps et al., 2016; Geyer and Sarradj, 2019). Jodin et al. (2017) have showed that by using a similar, but active, trailing edge modification the wake structure is modified and it is this type of flow modification that is thought to be the mechanism behind the low frequency noise reduction. It can be seen that the reduction in the low frequency range has been scattered into the medium to high frequency range ($\sim$ 1 kHz). As the Reynolds number is increased, the reduction in the low frequency and the high frequency increase both reduce. This is postulated to be due to the low Eigen frequency of the current flaplet geometry, and therefore these benefits observed are limited to a finite low frequency range. It should be noted here that the flaplet Eigen frequency is insensitive with Reynolds number, whereby the frequency only increases a small amount from the original Eigen frequency. This is discussed in further detail in §4.

As the angle increases to $\alpha_g = 10°$, Fig. 3.4b, a tonal peak starts to emerge at 450 Hz for the reference case at $Re_c = 172,000$. As the Reynolds number increases further the tonal peaks in the baseline case increase in frequency and intensity. The tonal peaks which are observed for this angle of attack and the subsequent angles agree well with the 'tonal envelope' model, Fig.3.5, which was first proposed by Lowson, Fiddes and Nash (1994), when the angle is normalised using the empirical scaling factor (Brooks, Marcolini and Pope, 1986). A series of previous publications using the NACA 0012 have also been normalised, accounting for different experimental set-ups, and fall within this tonal envelope.

A particularly interesting result can be first seen in Fig. 3.4b, where the placement of the flaplets on the pressure side of the aerofoil significantly reduces or removes the tonal frequencies. Whereas the placement on the suction side does not have such a profound impact. However, it should be noted that the peaks are slightly reduced. The low frequency reduction is also observed, but is reduced compared to that of the zero

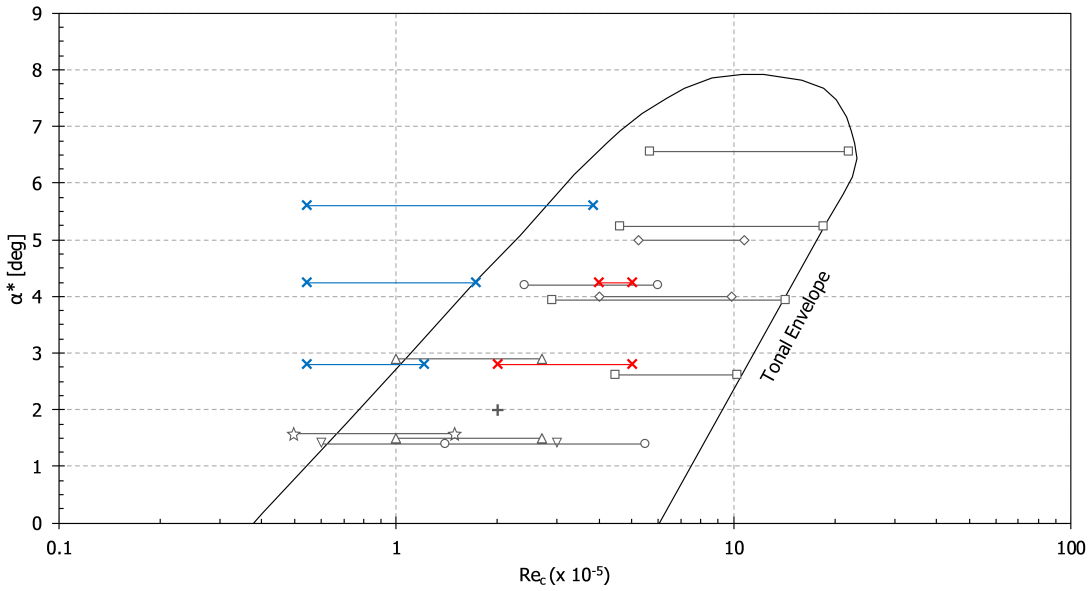


Figure 3.5: Comparison of previous literatures and the present study in the tonal noise envelope for the NACA 0012 aerofoil as proposed by Lowson, Fiddes and Nash (1994). The angle of attack (α^*) is corrected using the BPM empirical correction for the open jet wind tunnel results. Neither the direct numerical simulation (DNS) or closed wind tunnel angles have been adjusted. □ Paterson et al. (1972); ◇ Lowson, Fiddes and Nash (1994); + Desquesnes, Terracol and Sagaut (2007); ▽ Inasawa, Ninomiya and Asai (2013); ○ Chong, Joseph and Kingan (2013); △ Pröbsting, Serpieri and Scarano (2014); ☆ Arcondoulis et al. (2018); × Present (tonal) and × Present (non-tonal)

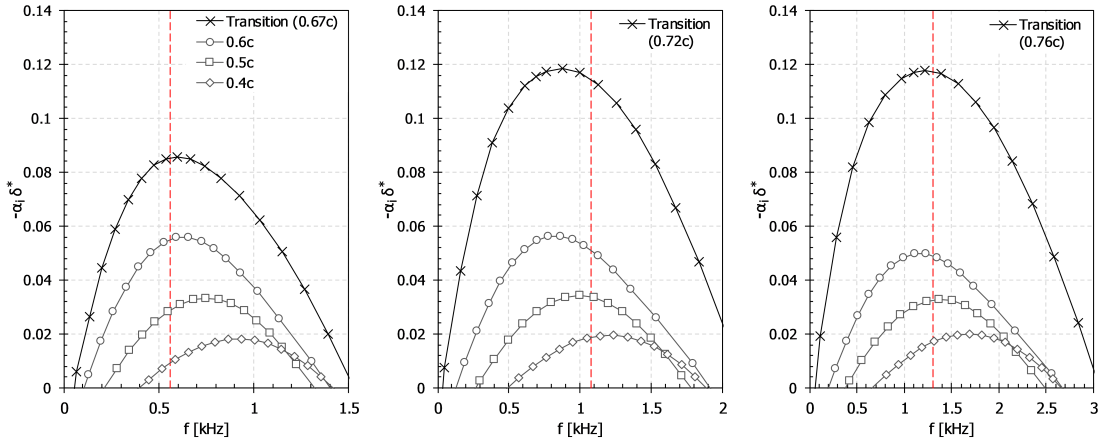
incidence case. This suppression of tonal noise is also seen at $\alpha_g = 15°$, Fig. 3.4c, at the higher Reynolds number cases. At $\alpha_g = 20°$, Fig. 3.4d, there is no real discernible difference between the two flaplet orientations due to the test cases being outside the tonal envelope. The low frequency noise reduction can still be seen at higher incidences, however it is reduced and has a trend of reducing as Reynolds number and α_g increase, in a similar fashion to that of the $\alpha_g = 0°$ case.

3.3.3 Linear stability analysis

As detailed by Lowson, Fiddes and Nash (1994) and McAlpine, Nash and Lowson (1999), the most amplified instability wave in the boundary layer, prior to the separation bubble on the pressure side, is very close to that of the tonal frequency observed. They also stated that a separation bubble on the pressure side is a necessary requirement in the production of tonal noise on the NACA 0012 aerofoil. Therefore a linear stability

analysis (LSA) has been carried out on the $\alpha_g = 10^\circ$ cases where the tonal peaks were observed (i.e. the top three cases in Fig. 3.4b). The LSA was carried out using the Airbus Callisto boundary-layer solver (a more detailed overview of the methods used in the solver can be found in Atkin (2014) and the references therein). In summary, Callisto has three distinct stages; obtaining the pressure distribution of an aerofoil (using the Callisto Viscous Garabedian and Korn method), produce boundary profiles for each station on the aerofoil and then carry out a stability analysis. In the present study the pressure distributions are created using Xfoil, which are then imported in to the QinetiQ BL2D solver. Due to the limitations of the open jet correction factor, the true angle of attack is unknown. Therefore, the measured lift forces were used in order to iterate the pressure distribution, such that the correct pressure distribution can be found. BL2D then uses a standard finite-difference, parabolic solver which is based on Horton and Stock (1995) to produce boundary layer profiles up to the transition point. These profiles are subsequently then analysed using QinetiQ CoDS, which is the linear stability analysis solver. CoDS uses an e^{N} method to obtain the N-Factors of the boundary layer profiles, and as such it can produce an amplification curve for each boundary layer profile. In the present results, Fig. 3.6, the non-dimensional spatial growth rate, $-\alpha_i\delta^*$, is plotted against modal frequency (f), where δ^* is the local displacement thickness of the boundary layer and α_i is the imaginary part of the spatial growth rate. A negative α_i indicates an unstable mode, hence the maxima in the $-\alpha_i\delta^*$ curves show the most unstable mode and the corresponding frequency it occurs at. As the current aerofoil was modelled as a semi-infinite 2D model, only Tollmien-Schlichting (T-S) waves are responsible for the instability growth.

The general trend, that can be seen in Fig. 3.6, is that the spatial growth rate of the instabilities increases in amplitude as they are convected downstream. The most amplified modal frequency also becomes more defined. Eventually non-linear effects take over, shortly followed by a breakdown to turbulence. As such the linear stability analysis is not valid beyond this point. The most amplified frequency in the boundary layer can therefore be found at the point prior to when these non-linear instabilities take over forming a laminar separation bubble (LSB). When comparing the frequency



(a) $Re_c = 243,000;\ \alpha_g = 10°$ **(b)** $Re_c = 300,000;\ \alpha_g = 10°$ **(c)** $Re_c = 384,000;\ \alpha_g = 10°$

Figure 3.6: The spatial growth rate on the pressure side of the aerofoil at different chordwise positions (x/c) against the frequency at which they occur. (---) Indicates the frequency where the tonal peak (f_n) is observed in the experiment, see Fig. 3.4b.

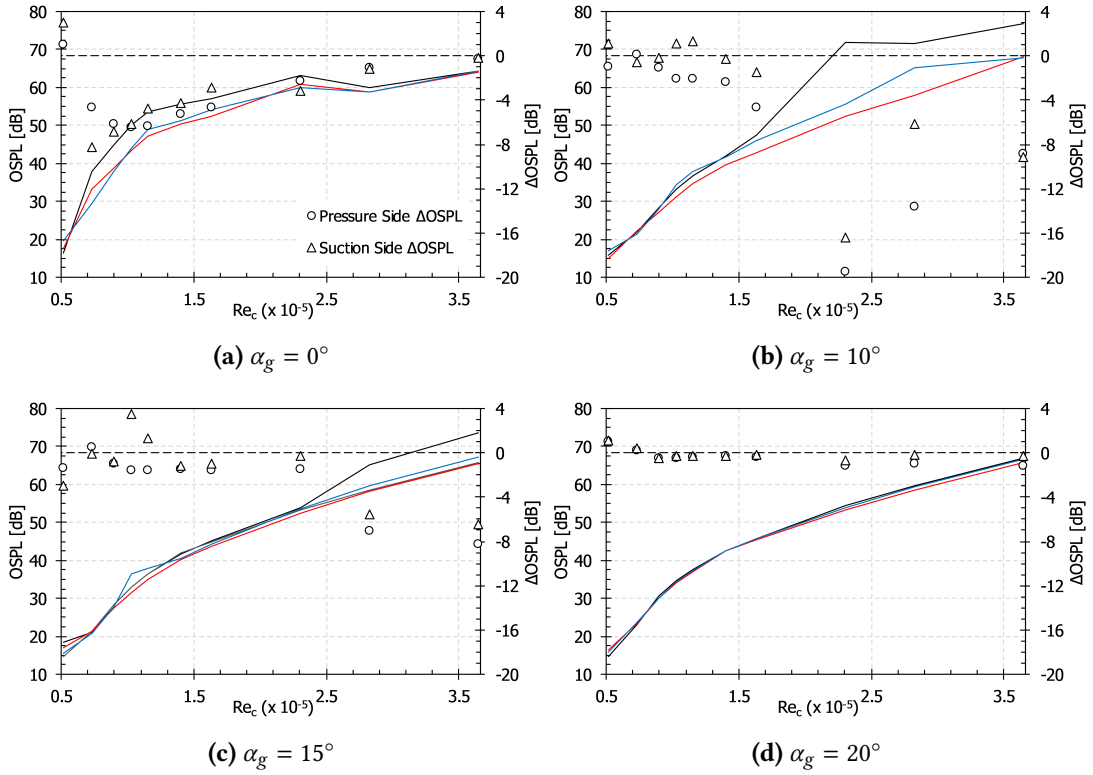
at which this maximum growth rate occurs, to the corresponding experimental tonal peaks (see Fig. 3.4b), good agreement between both sets can be seen. The addition of the flaplets on the pressure side of the aerofoil creates a small step (measured to be 0.28 mm) at a chordwise position of 0.85c, which is in the region of this separation bubble. This could trigger transition earlier and as such the LSB is not present. Therefore the tonal noise component is removed, as the presence of a LSB is a prerequisite for tonal noise (Lowson, Fiddes and Nash, 1994).

3.3.4 Overall sound pressure level measurements

Fig. 3.7 shows the overall sound pressure level (OSPL) obtained by beamforming as described in Section 3.2. The OSPL is a means of summing all of the acoustic contributions from each frequency in the signal to give one numerical value for each test case (see Eqn. (3.1)). In order to easily quantify the effects numerically, the difference between the corresponding baseline and flaplet cases (see Eqn. (3.2)) has been analysed as well.

$$\mathrm{OSPL} = 10\log_{10}\left[\sum_{f=0.1\ kHz}^{f=10\ kHz} 10^{\mathrm{SPL}_i/(10\ \mathrm{dB})}\right] \tag{3.1}$$

$$\Delta\mathrm{OSPL} = \mathrm{OSPL}_{\mathrm{flaplet}} - \mathrm{OSPL}_{\mathrm{baseline}} \tag{3.2}$$



(a) $\alpha_g = 0°$ **(b)** $\alpha_g = 10°$

(c) $\alpha_g = 15°$ **(d)** $\alpha_g = 20°$

Figure 3.7: Overall sound pressure levels for the reference cases and the flaplet, pressure side mounted, cases. ΔOSPL has been plotted on the second axis to yield a clear indication of the difference at each Reynolds number. The zero line on the ΔOSPL axis is shown as (- - -). Reference (—), flaplets pressure side mounted (—) and flaplets suction side mounted (—). ○ Indicates the ΔOSPL of the pressure side mounted flaplets and △ indicates the ΔOSPL of the suction side mounted flaplets.

For the $\alpha_g = 0°$ case, Fig. 3.7a, it can be seen that both flaplet orientations lead to a reduction of ~5-7 dB up to a Reynolds number of 250,000. Then beyond this, the overall noise reduction approaches zero. The large reduction in the low Reynolds number range is due to the observed low frequency reduction in Fig. 3.4a. Then at the higher velocities the smaller low frequency reduction cancels out with the high frequency noise increase. For the increased angles, where tonal noise is observed (Fig. 3.7b and 3.7c), the trend is the opposite. The low Reynolds number cases show little or no noise reduction. But as Reynolds number increases, the tonal noise component starts to emerge on the reference aerofoil and as such the reduction becomes much more profound. At $\alpha_g = 10°$, noise reductions of up to ~16-20 dB can be seen and ~6-8 dB can be seen at $\alpha_g = 15°$. As was seen in Fig. 3.4b and 3.4c, the suction side flaplets do not show as much noise reduction as the pressure side flaplets. This is due to a reduced tonal noise suppression and an

increased noise level at high frequencies. At $\alpha_g = 20°$, there are very little differences between all the cases, resulting in minimal noise reduction benefits. Table 3.2 gives the averaged ΔOSPL for each of the angles.

α_g	0°		10°		15°		20°	
Flaplet placement	P	S	P	S	P	S	P	S
Average ΔOSPL [dB]	-3.62	-3.47	-5.49	-3.07	-2.48	-1.35	-0.41	-0.09

Table 3.2: Average ΔOSPL for each of the geometric angles of attack (α_g). A placement of 'P' indicates that the flaplets are affixed to the pressure side and 'S' indicates a suction side placement.

3.3.5 Aerodynamic force measurements

The integral aerodynamic forces were taken simultaneously with the acoustic measurements for the current study. Due to the open jet flow conditions, the exact span that is subjected to the flow is not precisely known. Therefore the lift and drag forces have been normalised by their respective baseline measurement, to give an indication of relative performance difference.

$$F_L^* = \frac{F_{L,i}}{F_{L,ref(i)}} \tag{3.3}$$

$$F_D^* = \frac{F_{D,i}}{F_{D,ref(i)}}, \tag{3.4}$$

In Eqns. (3.3) and (3.4), $F_{L,i}$ and $F_{D,i}$ are the measured lift and drag for the cases with the flaplets, while $F_{L,ref(i)}$ and $F_{D,ref(i)}$ are the corresponding forces of the reference aerofoil at the same Reynolds number and geometric angle of attack. Therefore a value of $F_L^* > 1$ means an increase in lift compared to the baseline and vice versa for a values less than 1. The same reasoning holds for F_D^*. A generic trend can be seen in Fig. 3.8, where the pressure side placement decreases drag and lift and the suction side placement increases both lift and drag. At $\alpha_g = 20°$, the trend does not hold where the pressure side cases have an increased drag, but with comparable lift. This trend is in agreement with a basic XFLR simulation, where the flaplet orientation (as indicated in Fig. 3.1c) alters the circulation of the aerofoil and hence the aerofoil performance. As the Reynolds number

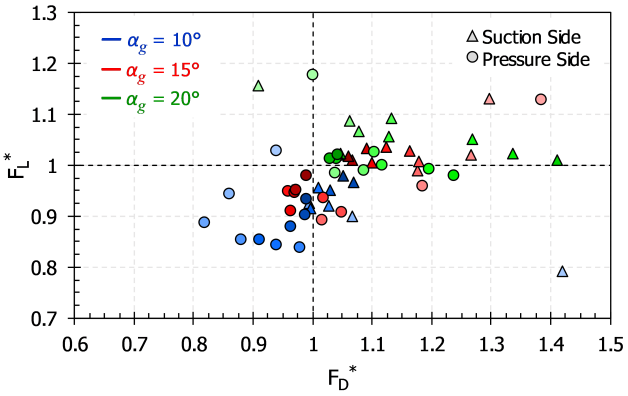


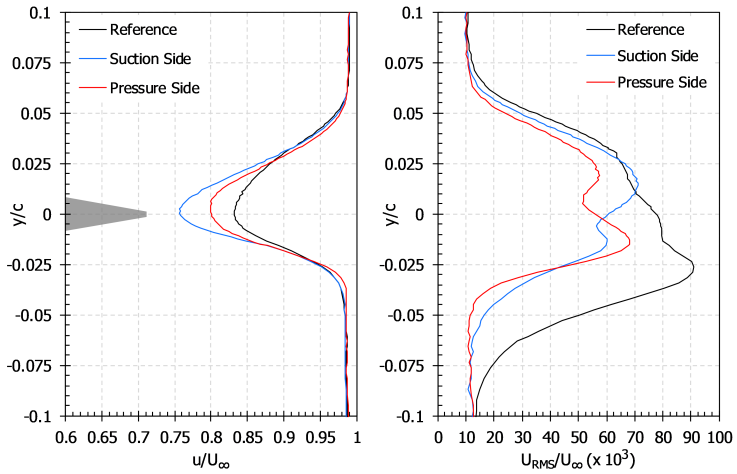
Figure 3.8: Normalised lift and drag measurements for all cases, where the shading of the colours indicates the Reynolds number. A lighter shade indicates a lower Reynolds number and the darker shade indicates the higher Reynolds number cases.

increases, it is also seen in both cases, that the results converge to the centre of the polar. The results for $\alpha_g = 0°$ have been omitted due to very small values observed for the lift, due to the symmetry of the aerofoil, and as such any deviation gives a very large F_L^*.

3.3.6 Hot wire anemometry

The mean flow profile and fluctuation statistics in the wake of the aerofoils were measured with a hot-wire traversed in y-direction at a distance of 0.25c downstream of the solid trailing edge. The measurements with the attached flaps were all compared to the reference case at the same position and angle of incidence. The mean profiles in Fig. 3.9a demonstrate an increased wake deficit for both flaplet cases compared to the plain aerofoil. Partly, this effect is due to the extension of the chord by the presence of the attached flaps, which in effect extend the trailing edge to 1.1c. Therefore, in the cases with attached flaps the boundary layer will grow further and the resulting wake deficit at the measurement location should be larger. When comparing only the two different cases with flaplets, it is seen that the deficit, in the case of the flaplets attached to the pressure side, is not as pronounced as in the suction side case. In addition, it has also a somewhat smaller width of the wake, which indicates a lower drag. This is in agreement with the observations seen in Fig. 3.8.

The effect of the flaplets is more evident when comparing the statistics of the velocity fluctuations, u_{RMS}, as shown in the profiles in Fig. 3.9b. The reference case exhibits



(a) U velocity **(b)** u_{RMS}

Figure 3.9: Hot wire anemometer results of the streamwise component (u) for the case at Re_c = 243,000 and α_g = 10°. The shaded area in Fig. 3.9a is a graphical representation of the reference aerofoil orientation with respect to the profile measurements.

overall significantly higher values than both of the flaplet cases, with a pronounced lobe on the pressure side of the aerofoil. The rms-profiles for the cases with attached flaplets show two distinct lobes, with the broader of the two situated on the suction side of the aerofoil, associated with the thicker shear layer on this side. The larger peak of both lobes in each rms-profile is always found on the same side, where the flaplets were attached.

The turbulence spectra of the streamwise velocity fluctuations (u') are displayed in Fig. 3.10, normalised by a nominal value of $\Phi_0 = 1\ m^2/s$. For clarity, the suction side and pressure side spectra have been spaced with -10 dB increments from the reference case to distinguish between the plots presented in the same figure. The reference case clearly illustrates the strong tonal peak at about 700 Hz, together with the first harmonic at 1.4 kHz. In addition, a pair of fringe frequencies, equispaced by 70 Hz on either side of the spectral peak is visible, similar as those observed by Pröbsting, Serpieri and Scarano (2014). The frequency of the peak in the reference case is slightly different to that of the tonal noise peak in Fig. 3.4b. This is believed to be due to the different experimental arrangement and mounting mechanism that had to be used for the hot-wire anemometery experiment. As such the angle of attack might be slightly different. The angle of attack is set manually and as such care was given to try to get the

angle of attack as close to the set angle as possible but some slight differences, typically $\pm 0.1^{\circ}$, could be seen. As the tonal noise is sensitive to any differences, a combination of the different mounting technique and possible slight different angle of attack are attributed to this difference. When the flaplets are attached to the aerofoil, one can clearly see the beneficial modification of the spectrum along the tonal peak. When attached to the pressure side, the flaps lead to a complete disappearance of the frequency peaks corresponding to the tonal noise. In comparison, when the flaps were attached to the suction side a tonal peak is still visible at a similar peak frequency range as for the plain aerofoil, however at lower energy ($\sim$ 13 dB lower) as the first harmonic is not present. In addition, there is no indication of any fringe frequencies. The results furthermore demonstrate the beneficial effect of the flaps at the trailing edge, similar as it was observed earlier in the flow studies reported by Talboys and Brücker (2018). In conclusion, the flaps lead to a redistribution of energy from velocity fluctuations in certain frequency bands towards a more broadband spectrum. The positive feedback of the lock-in of the oscillating flaps onto the fundamental instability of the boundary layer on the suction side has already been proven by detailed flow measurements (Talboys and Brücker (2018)). Therefore we suggest that the observed cancellation of the fringe frequencies is related to this lock-in effect. Pröbsting, Serpieri and Scarano (2014) argued that the fringe frequencies are caused by the modification of vortical structures convecting over the surface, which are affected by a back-scatter effect when those structures shed from the trailing edge. We found these vortical structures to be rollers in the shear-layer as a consequence of the fundamental instability. The flaps had clearly an influence on delaying the non-linear interaction of these rollers. This could indicate that the presence of the oscillating flaplets damps the related pressure fluctuations associated with these interactions. This hypothesis is somewhat supported by the u_{RMS} values shown in Fig. 3.9b, where a large reduction in both is observed on the pressure side of the aerofoil.

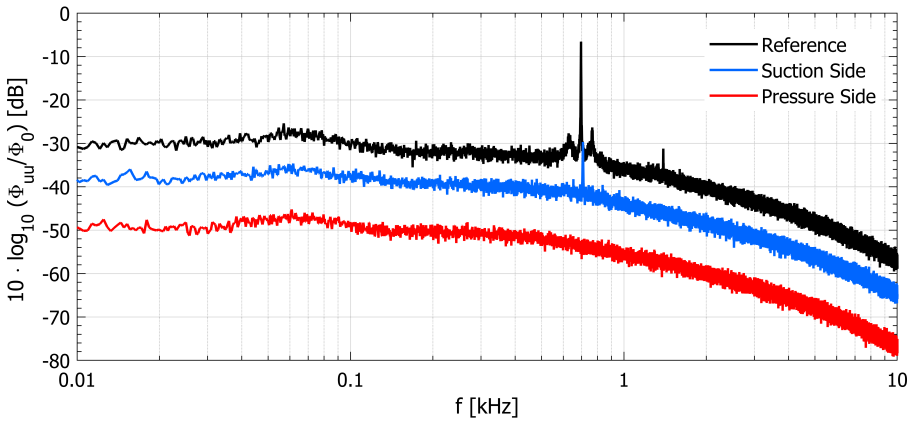


Figure 3.10: Fluctuating streamwise velocity turbulence spectra (Φ_{uu}), normalised with $\Phi_0 = 1\ \mathrm{m}^2/\mathrm{s}$, behind the trailing edge for the untripped case at $\mathrm{Re_c}$ = 243,000 and $\alpha_\mathrm{g} = 10°$

3.4 Conclusion

Aeroacoustic measurements with a microphone-array were carried out in an anechoic chamber for the flow along a NACA0012 aerofoil in order to observe the acoustic effect of a trailing edge with attached flexible passive flaplets (bending beam oscillators). The measurements focus on moderate Reynolds number flows in the range 50,000 – 350,000 at geometric angles of attack $\alpha_g = 0° - 20°$, where strong tonal peaks are observed on the baseline case consistent with previous literature Desquesnes, Terracol and Sagaut (2007). Two distinct situations were tested: one in which the flaplets were attached to the pressure side, tangentially extending the surface down the trailing edge; the other is with the flaplets attached to the suction side and extending this surface, respectively. Both configurations have a clear beneficial effect on reducing the tonal noise. For the case with the flaplets attached to the pressure side the tonal peaks even are completely cancelled out and the overall sound pressure level (OSPL) is reduced by up to 20 dB. This is suggested to be due to a modification to the laminar separation bubble on the pressure side, which is the key mechanism for tonal noise. High-Speed PIV measurements are currently under way in our lab to further elucidate the dynamics of the separation bubble. On the suction side, the flaplets are known from Talboys and Brücker (2018) to stabilise the shear-layer rollers developing in the boundary layer via a lock-in mechanism. Whether this lock-in mechanism has an effect

on the development of the T-S waves on the pressure side of the aerofoil is still not yet fully established. However, it is clear that the oscillatory behaviour of the flaplets is having an effect on the global flow circulation which will affect the separation bubble length and hence the tonal noise. Also for the suction side case a reduction in low frequency noise observed. This results in an overall noise reduction of ~1.5 – 2 dB over the whole range of Reynolds numbers. The findings from the acoustic measurements are complemented with results from aerodynamic force measurements as well as hot wire anemometry measurements in the wake. For the case with flaplets on the suction side, the force measurements show also a benefit in aerodynamic performance by increasing the lift. This results is consistent with recent flow simulations for a NACA0012 with an actively controlled trailing edge undergoing harmonic oscillations (Jodin et al., 2017). Note, that the described aeroacoustic observations are only valid for the specific flap geometry and mechanical properties chosen, consistent with the previous flow study reported in Talboys and Brücker (2018). For a more global conclusion, the studies should incorporate the effect of different flaplet length, width and inter-spacing. This is currently being investigated in our lab.

3.5 Critical analysis

3.5.1 Overview and study contributions

This study is an acoustic study, looking into what effect the trailing edge flaplets have on the aeroacoustics of a NACA0012 aerofoil. During this study the flaplets were attached, tangentially, on the surface of the aerofoil on the pressure and suction side of the aerofoil in separate experiments. A reduction was observed in the low frequency noise spectra and a reduction in the tonal noise. This reduction in tonal noise was most evident when the flaplets were on the pressure side where the tonal noise had been neutralised. This is believed to be due to a small step introduced by the flaplets themselves (i.e. the thickness of the flaplets), hence tripping the separation bubble on the pressure side of the aerofoil which is a necessity for tonal noise. A noise increase was also observed at higher frequencies but the benefits from tonal noise reduction and the low frequency reduction outweighed this increase.

3.5.2 Open jet considerations

There are a few considerations that need to be taken into account when using open jets for acoustic measurements. One consideration that will be discussed in §4.5, is the effect of the jet shear layer on the acoustic results. Another consideration that will be discussed here is the effect of the aerofoil on the flow of the jet and the consequences it has on the aerodynamics. In the presence of the aerofoil, the jet gets curved and as such this alters the aerofoils properties such as the effective camber and the angle of attack; and hence the measured aerodynamic forces. For this study it is still fair to compare the plain aerofoil with the aerofoil with attached flaplets, but care would need to be taken when comparing to other work. Therefore Brooks, Marcolini and Pope (1984) have proposed a method to find the angle of attack that would give an equivalent lift and the camber line of the aerofoil that would give the same pressure distribution in an unbounded flow situation. Both of these methods use the aerofoil chord (c) and tunnel height (nozzle diameter, D).

$$\alpha^* = \alpha_g/\zeta \tag{3.5}$$

$$\zeta = (1+2\sigma)^2 + \sqrt{12\sigma} \tag{3.6}$$

$$\sigma = (\pi^2/48)(c/D)^2 \tag{3.7}$$

Moreau et al. (2003) then carried out detailed RANS (Reynolds Averaged Navier Stokes) simulations looking into more detail at the how the width of the jet affects the pressure distribution over an aerofoil. What they saw was that when the jet width is not sufficiently wide enough, in comparison to the chord, then the aerofoil acts more as if it were part of a blade cascade. This means that the pressure distribution over the aerofoil will be impacted and as such the aerodynamic performance will also be effected. Hence, any comparison to isolated aerofoils should be avoided but as mentioned above comparison within the study is fair. In this study the chord was c = 0.19 m and the nozzle diameter was D = 0.2 m, therefore the chord to jet width ratio is c/D$\sim$ 1. In the §3.3.2 the existence of tonal noise was compared, Fig. 3.5, with other publications with the angle adjustment presented in equation (3.5). However, here it was more to see if

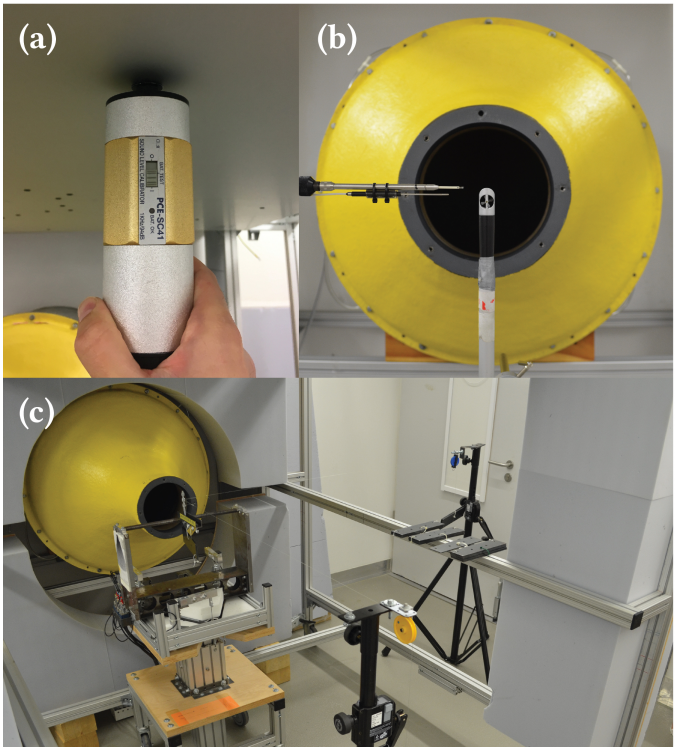


Figure 3.11: Calibration of the measurement systems; **(a)** calibration of the microphone array, **(b)** calibration of the hot wire anemometer, **(c)** calibration of the force balance.

the results of the tonal noise envelope fits, generally, with other NACA0012 aerofoil studies. It was seen that there was good agreement with these other studies but more detailed comparison should not be carried out due to the reasoning detailed above.

3.5.3 Calibration of measurement systems

3.5.3.1 Microphone array

To calibrate the microphone array, a PCE-SC 41 acoustic calibrator was used as can be seen in Fig. 3.11a. This calibrator was placed on each microphone individually and a 1 kHz and 94 dB noise source was played. The response of each microphone was then recorded. The calibration file then has a correction factor for each microphone, where the factor is used to multiply the measured sound pressure in order to get a sound pressure of 1 Pa; which corresponds to a sound pressure level of 94 dB. In an ideal world, the microphone calibration would be carried out at multiple different frequencies across the measured range. However, it is very typical that they are calibrated at one frequency and therefore it is assumed that the microphone sensitivity does not change with frequency.

Although it is not related to the calibration of the microphone array, here the properties of the surrounding walls should be noted. An absorbing foam is used only for three side walls and the bottom of the cabin surrounding the test section. The material is a melamine foam made by BASF called Basotect, which is quite common in room acoustics. For the walls, the material was used with a thickness of 0.24 m, leading to an absorption coefficient close to 1 at frequencies above 125 Hz (Geyer and Sarradj, 2019).

3.5.3.2 Hot wire anemometery

To calibrate the hot wire, the voltage at known wind speeds needs to be recorded and at known air temperatures. The process of the calibration that was followed was the same as documented by Jørgensen (2002). As seen in Fig. 3.11b, the hot wire probe is placed into core of the open jet (horizontal in the figure) along with a vane anemometer (vertical in the figure). For the calibration the lower velocity limit was at least, $0.1 \cdot U_{\text{min,exp}}$, and the upper limit was at least, $1.5 \cdot U_{\text{max,exp}}$. Here the $U_{\text{exp}} = 19.1$ m/s, therefore the lower limit of the calibration should be at least $U_{\text{min}} = 1.9$ m/s and the upper limit should be at least $U_{\text{max}} = 28.7$ m/s. As such, that limit were set to 0.7 m/s and 30 m/s. As the calibration curve for a hot wire is a polynomial curve, it is prudent to measure many different velocities between the two velocities. Where more measurements are taken towards the lower velocity range and fewer at the higher range. Once the list of velocities has been set, the tunnel was then switched on and using the vane anemometer the first velocity was set and once the tunnel speed was stabilised the voltage of the two wire probe was taken. This process was repeated 9 more times such that 10 velocities and corresponding voltages were taken. A 4^{th} order polynomial curve, equation (3.8), is then fitted to the data and stored. Where U is the wind tunnel velocity, C_i are the calibration coefficients that are to be found and E is the measure voltage of each probe. Figure 3.12 shows the 4^{th} order polynomial fitted to a set of calibration data for both of the probes.

$$U = C_0 + C_1 E + C_2 E^2 + C_3 E^3 + C_4 E^4 \tag{3.8}$$

Where the coefficients for each probe can be seen in Table 3.3

Probe No.	C0	C1	C2	C3	C4
1	-4.613	5.508	-2.108	0.616	-0.024
2	-10.790	15.897	-7.842	1.939	-0.130

Table 3.3: Hot wire anemometery calibration coefficients.

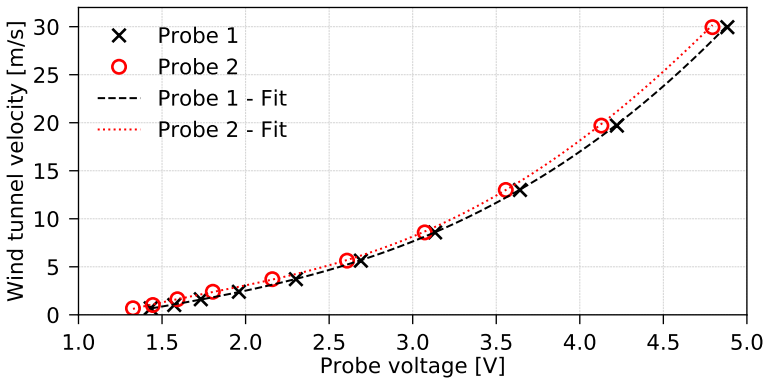


Figure 3.12: Hot wire anemometer 4^{th} order polynomial fit for each of the wire on the X wire probe.

As a two wire probe is used here, it is important to make sure that the probe is normal to the flow such that when the yaw of the two probes are resolved there are no errors. To do this, once the calibration above was complete the tunnel was turned on at a low velocity ($u \approx 2$ m/s) and a live view of the resolved velocity components was seen on the miniCTA software. If the v velocity component was not equal to zero then the the rotation of the hot wire probe was adjusted until it showed zero. Once this was complete, a velocity calibration was again carried out and a check on the v velocity component was checked again to make sure everything was correct. Table 3.4 shows the resolved components for the data in Fig. 3.12.

The final stage was to be mindful of the temperature variations throughout the experiment. To compensate for any increases in air flow temperature during the experiment, a temperature probe (Dantec Dynamics 90P11, accuracy ±0.3°C from 0°C – 40°C) was attached just below the hot wire probe holder (see Fig. 3.11b).

The temperature was then used to correct the measured voltage and hence the velocity. For this study, the calibration was carried out after every other wake measurement to ensure the accuracy of the measurements.

Input velocity		Measured velocity	
u [m/s]	v [m/s]	u [m/s]	v [m/s]
0.68	0.00	0.64	-0.02
1.02	0.00	1.10	0.02
1.62	0.00	1.61	0.02
2.40	0.00	2.37	0.00
3.71	0.00	3.69	-0.04
5.64	0.00	5.68	0.01
8.58	0.00	8.60	0.03
13.00	0.00	12.95	-0.03
19.70	0.00	19.73	0.01
29.95	0.00	29.95	0.00

Table 3.4: Comparison of the set input wind tunnel velocity and the measured velocity, after the calibration and resolution of each component.

3.5.3.3 Force balance

To calibrate the force balance (see Fig. 3.11c), two tri-pods with pulley systems were place in two locations, one horizontally behind the force balance (to simulate aerodynamic drag) and one laterally to the side of the balance (to simulate aerodynamic side force). There was a vertical rod with three different notches are at different heights (for the wire connecting to the side force and drag weights to be attached to and simulate pitch, roll and yaw moments) and a series of hooks at different horizontal distances (to simulate lift/downforce and also a pitching moment). At the end of the wire, in both horizontal and lateral directions, weights were added and also on the horizontal hooks, weights were also attached. By varying the height at which the force acts, the horizontal distance at which the lift force acts and the force/weight itself many different combinations can be recorded. As the balance measures six components, a 6x6 matrix of voltages and the corresponding weights will need to be resolved. Therefore, to resolve this there needs to be at least 36 different combinations or weights and heights such that the matrix can be solved. To allow for extra redundancy, 40 different combinations were measured and the matrix was then resolved.

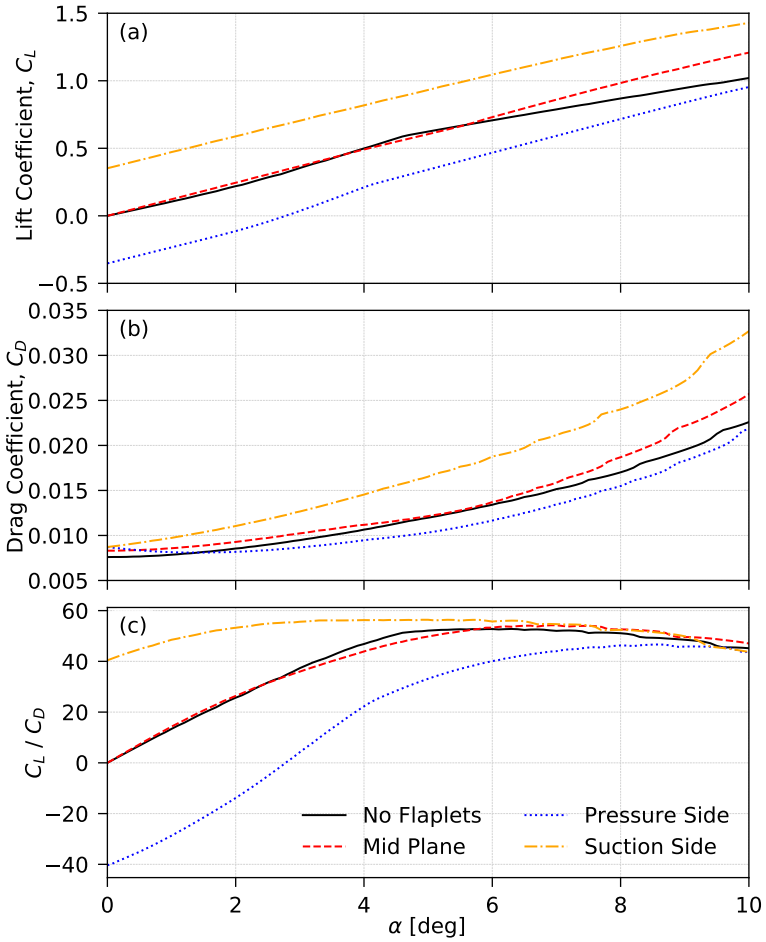


Figure 3.13: XFLR Simulation looking at lift and drag coefficients for different flaplet positions on the aerofoil at $Re_c = 350,000$.

3.5.4 Simulation for lift and drag coefficients

As was mentioned in §3.3.5, an XFLR simulation was carried out in order to get an idea of the circulation change due to the placement of the flaplets. Figure 3.13 shows $\alpha = 0 - 10°$ for the lift and drag coefficients at a nominal Reynolds number, $Re_c = 350,000$. It can be seen that when there are no flaplets and flaplets in the mid plane of the aerofoil; i.e. extending from the trailing edge, there is little difference at angles below $\alpha = 6°$. Beyond this there is some deviation, where both the lift and drag is seen to increase with the flaplets. However, when looking at the lift-drag ratio, Fig. 3.13c, it can be seen that the two lines more or less trace each other across the displayed range.

When the flaplets are on the pressure side of the aerofoil, as in Fig. 3.1c, the lift is reduced, so much so that it creates downforce for angles less than 3°. Showing

that the flaplets are inducing a camber effect on the aerofoil. When looking at the lift-drag ratio, it can be see that; although the drag is lower than the base case, the lift is significantly lower and as such the ratio is much lower than showing that they are much less efficient when on this side of the aerofoil.

The opposite occurs when the flaplets are placed on the suction side of the aerofoil, where the lift and drag are both increased. When looking at the lift-drag ratio, it seems to converge to the no flaplet case and where the flaplets are on the mid plane at angles beyond 6°.

Overall, it should be noted that for future work the flaplets should be placed on the mid plane of the aerofoil rather than tangentially on the suction or pressure side, such that a better comparison can be made on the aerodynamic performance of the flaplets.

3.5.5 Background noise

In the lower Reynolds number cases ($Re_c = 54,000 - 108,000$) some tones emerged at $\alpha_g = 15°$ and 20° in Fig. 3.4. As the acoustic results are single microphone measurements, they pick up all noise sources present in the flow and from the surroundings. To assess whether these tones are from the aerofoil trailing edge or not a beamforming algorithm was used. As this was a quick check the CleanSC algorithm was chosen, where the integration sector for the algorithm was set at the trailing edge (see the sector used in Fig. 4.1a). Figure 3.14 shows the comparison of the single microphone and the CleanSC. What is immediately clear are the frequencies where the acoustic sources are not picked up by the CleanSC beamformer. This is one of the limitations of this model, which is discussed in further detail in §4.5.3. However, the tones that are present between $f = 300 - 500$ Hz on the single microphone spectra are no longer present when the beamformer is focused on the trailing edge of the aerofoil. Which indeed shows that these are more likely to be from the wind tunnel or outside of the region of interest, as such these will have no bearing on the results of this study.

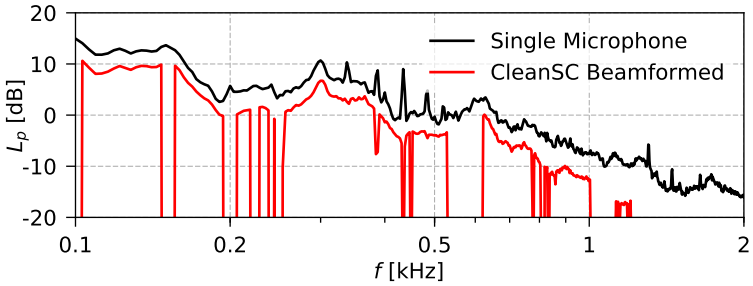


Figure 3.14: Single microphone vs CleanSC beamformed acoustic spectra at $Re_c = 94,000$ and $\alpha_g = 20°$.

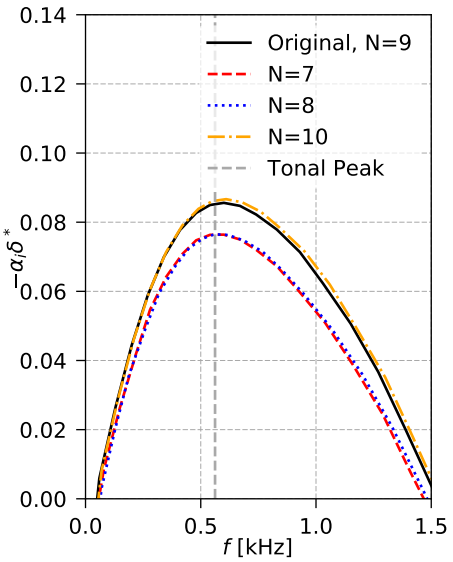


Figure 3.15: Linear stability analysis N-factor sensitivity at $Re_c = 243,000$ and $\alpha_g = 10°$.

3.5.6 N-factor sensitivity

When using the e^N method for transition prediction, the sensitivity of the N-factor needs to be addressed. If a larger N-factor is used, the threshold for transition is greater and as such transition is delayed and vice versa for smaller N-factors. Therefore when looking at the linear stability analysis in §3.3.3, how the predicted tonal noise peak frequency changes with different is important for validation. Figure 3.15 shows the comparison of the transition point and the most amplified modes at this point. Although the levels of the amplification are different at the various N-factors, it is clear that there is very little difference in the most amplified frequency for this condition. When comparing to the observed tonal peak, they again show good agreement and it can be said that the use of an N-factor of 9 throughout §3 is sound.

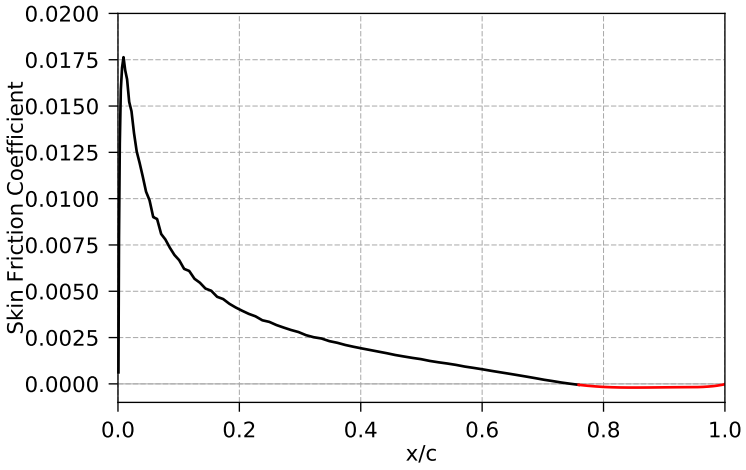


Figure 3.16: Skin friction coefficient on the pressure side of the aerofoil across the whole chord, at $Re_c = 243,000$ and $\alpha_g = 10°$. Where the red line indicates where the skin friction coefficient is negative.

3.5.7 Separation bubble prediction

Within §3.3.3 the presence of a separation bubble on the pressure side of the aerofoil was mentioned. However no proof was given, as such an XFOIL simulation has been conducted at $Re_c = 243,0000$ and at $\alpha_g = 10°$, which is a case that is seen to have tonal noise in Fig. 3.4. Figure 3.16 shows the skin friction coefficient along the pressure side of the aerofoil. The skin coefficient has been used as when there is a negative value it is a very clear indicator of flow separation / reversed flow. It can be seen that at $x/c = 0.78$, the skin coefficient goes negative (indicated as a red line) until the trailing edge. Therefore, it is indeed indicating separation on the pressure side of the aerofoil for this condition. Later in the thesis, §4.3.2, a surface oil flow visualisation is taken, albeit at a higher Re_c, which also shows this separation on the pressure side of the aerofoil at this angle of attack.

3.5.8 Future work

Within this chapter, it can be seen that there are many extensions of the project to consider. The first is that the flaplets should be placed along the chord line (mid plane) of the aerofoil. This is to mitigate any observed effects from either the alteration of the camber and the tripping of the boundary layer towards the rear of the aerofoil. When

thinking about what effect this will have on the acoustics, it is expected to have less of an effect on the tonal noise but the low frequency reduction is still expected to be present, as this effect was seen when the flaplets were on both sides of the aerofoil. An investigation into what effect different lengths, widths and inter-spacing should also be carried out. This will give more of an idea as to the true effect of: 1) how the acoustics are altered with changing Eigen frequency; 2) whether it is better to have wider or narrower flaplets, and whether the noise is radiated less/more when narrower/wider; 3) is it necessary to have such a small inter-spacing or can we obtain similar effects with a wider inter-spacing. These are all things that have been looked into, in Chapter 4.

4

Paper 3: A parametric study of the effect of self-oscillating trailing-edge flaplets on aerofoil self-noise

Contents

4.1 Introduction . . . 74
4.2 Experimental Arrangement and Measurement Techniques . . . 79
4.2.1 Wind Tunnel . . . 79
4.2.2 Aerofoil . . . 80
4.2.3 Acoustic Measurements . . . 80
4.2.4 Constant Temperature Anemometry . . . 81
4.2.5 Laser Displacement Measurements . . . 82
4.3 Results . . . 82
4.3.1 Static Flaplet Response . . . 82
4.3.2 Tonal Noise . . . 84
4.3.3 Acoustic, Hot Wire Anemometry and Vibration Results . . . 87
4.4 Conclusion . . . 114
4.5 Critical analysis . . . 117
4.5.1 Overview and study contributions . . . 117
4.5.2 Model Vibration . . . 117
4.5.3 Beamforming Considerations . . . 120
4.5.4 Carbon fibre flaplets . . . 129
4.5.5 Flaplet porosity as a metric . . . 133
4.5.6 Targeting certain Strouhal number noise reduction . . . 134
4.5.7 Other considerations . . . 134
4.5.8 Future work . . . 137

Abstract

This paper presents an acoustic study of a standard NACA 0012 aerofoil with additional self-oscillating passive flaplets deployed from the trailing edge for self-noise reduction, putting special emphasis on the potential reduction of tonal noise generated by the periodic shedding of vortices from the trailing edge. The flaplets protruding out of the trailing edge act as rectangular thin cantilever beams exited by the surrounding flow to oscillate in their dominant flexural bending mode. The noise attenuation performance is studied for different deployment length, width and inter-spacing to find the most dominant contributions at chord based Reynolds numbers Re_c from 100,000 to 900,000 and three geometric angles of attack $\alpha_g = 0°, 10°$ and $15°$. It was observed that all flaplet configurations oscillate and thereby reduce the tonal noise. The range of the highest noise reduction in the low frequency range scales with the Strouhal number based on chord length, whereby this range can be set specifically by how far the flaplets protrude out of the trailing edge. This determines the free vibrating length and therefore the natural frequency of the oscillators. Laser-based measurements of the flaplet oscillations confirm the occurrence of a lock-in mechanism observed in previous studies, which effectively describes the oscillating flaplets as pacemaker to keep the fundamental instabilities of the flow in their linear state. It is concluded that this contributes mainly to the tonal noise reduction while the more broadband noise reduction stems from the geometry of the flaplets acting as 'slitted-serrations'. A larger width of the flaplets is most effective in the low-frequency range, while narrower flaplets are best addressing high-frequency noise components. The results further show that a smaller inter-spacing also benefits the noise reduction. The study paves the way for novel morphing techniques to target specific noise ranges during different flight manoeuvres.

4.1 Introduction

Engineers have been extensively researching ways to mitigate aerofoil self-noise in recent years. There are various different sources of aerofoil self-noise, as explained in

detail by Brooks, Pope and Marcolini (1989), but the main source of noise is boundary layer – trailing edge interaction. For the current study, laminar boundary layer – trailing edge noise is present and this manifests itself as a strong tonal noise, which is particularly annoying for the human hearing spectrum. As such this tonal noise has had a significant amount of research, to obtain a better understanding of this phenomenon and how it can be avoided.

The first study to investigate in detail tonal noise was carried out by Paterson et al. (1972). They observed that there was an interesting feature, which they named 'laddering', occurring. The main tonal peak frequency was scaling with the freestream velocity, $f \propto U_\infty^{0.8}$, until a certain point when the tonal noise peak made a sudden jump to a high frequency, hence termed laddering. After averaging out all of these laddering events, across a wide range of velocities and frequencies, it was seen that $f \propto U_\infty^{1.5}$. Tam (1974) then proposed that the tonal noise is due to an acoustic feedback loop from an aeroacoustic interaction between instabilities in the boundary layer and noise sources situated in the aerofoil wake. The feedback model was expanded by Arbey and Bataille (1983), who showed that Tollmien-Schlichting (T-S) waves in the boundary layer diffract at the trailing edge of the aerofoil, subsequently creating acoustic waves that back-scatter upstream, feeding back into the feedback loop. This conclusion initiated more detailed investigations into the flow field around the aerofoil. Lowson, Fiddes and Nash (1994) and McAlpine, Nash and Lowson (1999) first showed that a necessary feature of tonal noise is the presence of a laminar separation bubble on the pressure side of the aerofoil. They then further found that by using linear stability theory, the frequency of the tonal noise component was that of the most amplified instability within the boundary layer. Desquesnes, Terracol and Sagaut (2007) carried out the first direct numerical simulation (DNS) on the tonal noise issue. It was found that there was another, co-existing, feedback loop coming from the instabilities in the boundary layer on the suction side of the aerofoil. It was then thought that this feedback loop modulated the fringe frequencies that are found on either side of the tonal peak. Pröbsting, Scarano and Morris (2015) carried out simultaneous Particle Image Velocimetry (PIV) and acoustic measurements to find that at very low chord based Reynolds numbers ($\mathrm{Re_c}$ = 30,000)

the tonal noise is generated by the suction side of the aerofoil, while the pressure side dominates the generation of the tonal noise at higher Reynolds numbers (Re_c = 230,000). By tripping either side of the aerofoil separately, it is demonstrated that both feedback loops can exist independently (Desquesnes, Terracol and Sagaut, 2007). Arcondoulis et al. (2019) built upon this dual feedback loop hypothesis to present an updated feedback model, where the tonal frequency is generated on both sides of the aerofoil. It was observed that these tones have a near exact frequency to each other, but the fringe frequencies were seen to have large differences when comparing either side of the aerofoil. Most of the boundary layer – trailing edge mitigation strategies applied by researchers are inspired from the well known 'silent' owl flight. One technique the owl uses, is due to its 'soft downy feather'. These features can be seen as acting like a porous surface, and Geyer et al. Geyer, Sarradj and Fritzsche (2010) and Geyer and Sarradj (2019) investigated the aeroacoustic benefit of having a porous aerofoil. It was found that by even having a small amount of porosity, either by a small streamwise amount of porosity (Geyer and Sarradj, 2019) or with a certain flow resistivity (Geyer, Sarradj and Fritzsche, 2010), a benefit can be seen in the low – mid frequency range. As the porosity increases, the benefit increases reaching up 10 dB broadband noise reduction. The benefits do come at a penalty, where there is an increase in high frequency noise. This is primarily due to the increased surface roughness that the aerofoil is then constructed of.

Another owl-inspired technique uses trailing edge brushes or serrations, mimicking the characteristic trailing edge structure formed by the feathers of owls (Herr, 2007), for which an acoustic reduction was observed in the high frequency range (2–16 kHz). This is believed to be due to the broadband noise of the turbulent boundary layer trailing edge interaction being affected. Finez et al. (2010) could show that the spanwise coherence of the shed vortices in the wake behind the trailing edge is reduced by 25% in the presence of brushes.

Serrations have been extensively researched in both the laminar boundary layer case (Chong, Joseph and Gruber, 2010; Chong and Joseph, 2013) and turbulent boundary layer case (Arce León et al., 2017; Arce León et al., 2018). For the laminar case, Chong et al. (Chong, Joseph and Gruber, 2010; Chong and Joseph, 2013) found that the flat plate

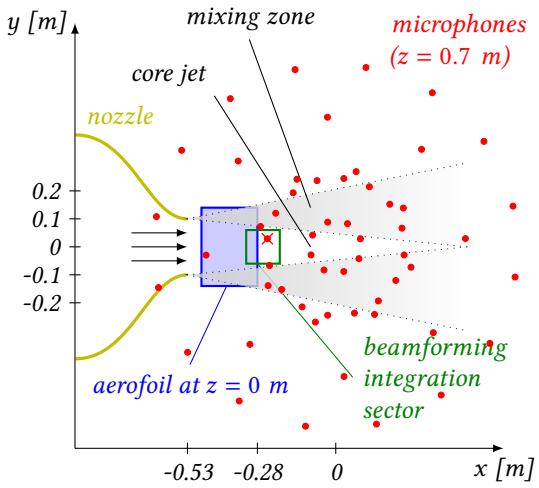
extensions were effective at reducing tonal noise by modifying the separation bubble on the pressure side of the NACA 0012 used. Another type of serration that has been seldom studied is slit-serrations. Gruber, Azarpeyvand and Joseph (2010) carried out a comparative experiment on a tripped cambered NACA 651210 aerofoil with saw-tooth serrations and slit serrations. They found that reductions of up to 3 dB can be achieved with the slit serrations at low frequencies but increase the noise level at high frequencies. It was seen that the maximum reduction occurs as the thickness is reduced and the spacing between the slits needs to be small for optimal noise reduction.

Studies with a single flexible flap at the trailing edge were investigated numerically by Schlanderer and Sandberg (2013). They carried out a DNS study on a flat plate with an elastic compliant trailing edge and found an aeroacoustic benefit at low and medium frequencies with an increased noise level at the Eigen frequency of the material. These results were confirmed later by Das et al. (2015) in an experimental investigation using a similar arrangement to Schlanderer and Sandberg (2013).

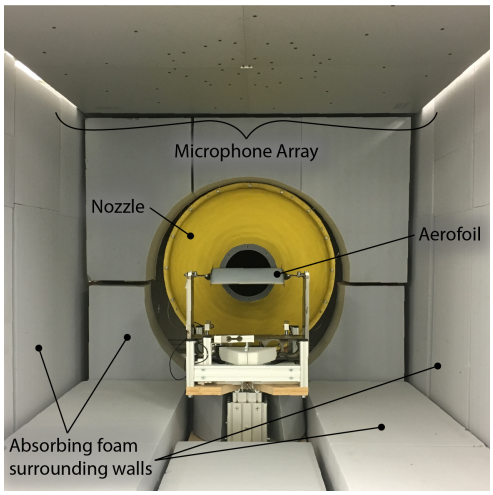
The present acoustical study continues a series of original experiments of the authors on arrays of individual self-oscillating elastic elements attached to the trailing edge of an aerofoil to reduce self-noise. This type of trailing edge modification with arrays of elastic flaps has been proven as a novel effective way for passive noise cancellation (Talboys and Brücker, 2018; Kamps et al., 2016; Kamps et al., 2017; Geyer et al., 2019; Talboys, Geyer and Brücker, 2019a; Talboys, Geyer and Brücker, 2019b). This mainly refers to tonal noise, which is generated by the periodic shedding of vortices from the trailing edge of an aerofoil. The noise reduction that can be achieved with the flexible flaplets was attributed to a lock-in process reported in (Talboys and Brücker, 2018), which causes the fundamental instabilities in the flow over the aerofoil - the periodic vortex shedding - to lock-in their frequencies with the natural frequency of the oscillating flaplets. Therefore, these attached oscillators effectively act as pacemaker, keeping the flow instabilities to remain in the state of linear growth. Using high-speed PIV measurements, the authors could show that non-linear instabilities within the shear layer along the suction side were suppressed by adding the flaplets to the trailing edge.

So far, variants of flaplets on aerofoils in these studies focused first on the location to attaching the flaplets to the trailing edge. In Talboys, Geyer and Brücker (2019a), experiments with flaplets tangentially to the pressure and alternatively to the suction sides of a NACA 0012 aerofoil were carried out across a moderate Reynolds number range (50,000 – 350,000, based on chord length). When attached to the pressure side, the flaplets were observed to effectively trip the boundary layer, which, ultimately, had the effect of completely removing the tonal noise component. When the flaplets were on the suction side, it was observed that the tonal noise was significantly reduced due to the above described lock-in mechanism and the subsequent dampening of T-S instabilities within the boundary layer. All of these effects culminated for the given flaplet geometry and properties in average overall sound pressure level reductions of 3.5, 4 and 2 dB at geometrical angles of attack of $0°, 10°$ and $15°$, respectively.

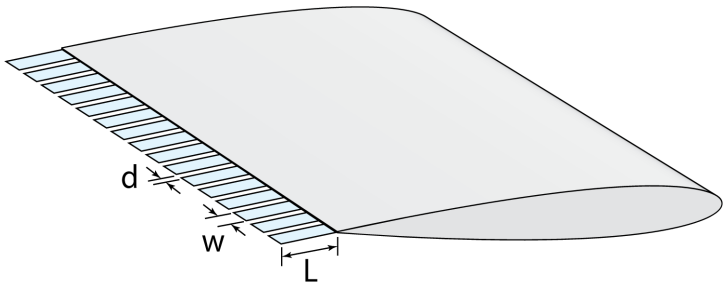
The objective of the present investigation is to test a broader parameter space of the geometry and properties of flexible trailing edge flaplets to explore the overall noise cancellation potential and the dominant contributions to it. Here the flaplets will be placed inside the aerofoil in a slit along the centre-chord line of the aerofoil, extending with their free ends tangentially out into the flow. By moving the flaps further inwards or outwards of the slit, it is possible to control the free length and therefore the Eigen frequency of the oscillator as they act as one-sided clamped cantilever beams. In addition, the flaplets will be tested at much higher Reynolds numbers than in the previous acoustic study by the authors (Talboys, Geyer and Brücker, 2019a). The primary focus of the present study is the variation of the flaplet geometrical parameters, such as their length, width and inter-spacing, on the sound power and associated radiated noise. All configurations are tested regarding their acoustic effect in an anechoic wind tunnel facility complemented with detailed velocity measurements in the wake using hot wire anemometry.



(a) Schematic display of the measurement setup, plan view. The single microphone used is indicated with a red cross.



(b) Photograph of experimental set-up, looking from downstream of the aerofoil and nozzle.



(c) Sketch of the aerofoil with the flaplets attached to the trailing (flaplet spacing d, width w and length L).

Figure 4.1: Overview of experimental set-up.

4.2 Experimental Arrangement and Measurement Techniques

4.2.1 Wind Tunnel

The experiments were carried out in an open jet style wind tunnel at Brandenburg University of Technology, Cottbus (Sarradj et al., 2009). Schematics and a photograph of the set-up are shown in Fig. 4.1. The wind tunnel was equipped with a circular nozzle with a contraction ratio of 16 and an exit diameter of D=0.2 m. With this nozzle, the maximum flow speed is in the order of 90 m/s. At 50 m/s, the turbulence intensity in front of the nozzle is below 0.1 %. For the present study the chord based Reynolds number (Re_c) was varied from 100,000 – 900,000 and the geometric angle of attack, α_g , was varied from $\alpha_g = 0° - 15°$. The chord used here is the solid aerofoil chord, and

as such the length of the flaplets was not taken into account for when calculating the chord based Reynolds number or chord based Strouhal number.

4.2.2 Aerofoil

The aerofoil used is a NACA 0012 symmetric aerofoil, with a chord of 0.19 m and a span of 0.28 m. The span is such that it extends the entire nozzle diameter, to ensure that there are no wing tip effects. The aerofoil was 3D printed, using a polyjet printer, in two halves, where the dividing line was the chord (centre) line of the aerofoil. This allowed the flaplets to be inserted easily along the chord line and extrude out of the trailing edge of the aerofoil, such that the free ends were orientated downstream (see Fig. 4.1c). This allows them to freely oscillate at their Eigen frequency (equal to the natural frequency). The determination of the Eigen frequency will be discussed in Section 4.3.1. The flexible trailing edge flaplets were manufactured, using a laser cutter, from a thin polyester film (see Table 4.1 for dimensions). It should be noted here that a singular flexible trailing edge, one that spans the entire trailing edge, was not tested in this study. This was motivated by the idea to break-up any spanwise coherence.

4.2.3 Acoustic Measurements

The acoustic measurements were performed using a planar microphone array consisting of 56 1/4 inch microphone capsules flush mounted into an aluminium plate with dimensions of 1.5 m × 1.5 m. The array was positioned in a distance of about 0.7 m above the aerofoil (see Fig. 4.1a). Data from the 56 microphones were recorded with a sampling frequency of 51.2 kHz and a duration of 60 s using a National Instruments 24 Bit multi-channel measurement system. To account for the refraction of sound at the wind tunnel shear layer, a correction method was applied that is based on ray tracing Sarradj (2017). In post processing, the time signals were transferred to the frequency domain using a Fast Fourier Transformation (Welch's method, Welch (1967)), which was done block-wise on Hanning-windowed blocks with a size of 16384 samples and 50% overlap. This lead to a small frequency spacing of only 3.125 Hz. The resulting microphone auto spectra and cross spectra were averaged to yield the cross spectral matrix. This matrix

was further processed using the DAMAS beamforming algorithm proposed by Brooks and Humphreys (2006), which was applied to a two-dimensional focus grid parallel to the array and aligned with the trailing edge. The grid used has a streamwise extent of 0.7 m, a spanwise extent of 0.4 m and an increment of 0.02 m. The outcome of the beamforming algorithm is a two-dimensional map of noise source contributions from each grid point, a so-called sound map. In order to obtain spectra of the noise generated by the interaction of the boundary layer with the trailing edge of the aerofoil, a sector was defined that only contains the noise source of interest. The chosen sector has a chordwise extent of 0.12 m and a spanwise extent of 0.12 m. Thus, spectra of the noise generated by this mechanism are derived by integrating all noise contributions from within this sector, while all potential background noise sources (such as the wind tunnel nozzle or the aerofoil leading edge) are excluded from the integration. The resulting sound pressures, which represent the values that would be measured at the center of the microphone array, were then converted to sound pressure levels, L_p (with a reference value of 20 μPa), and 6 dB were subtracted to account for the reflection of sound at the rigid microphone array plate. It should be noted here that for the 2D sound map figures used herein, a grid increment of 0.01 m was used to obtain better image resolution.

4.2.4 Constant Temperature Anemometry

Constant Temperature Anemometry (CTA) measurements were taken in separate experiments to the acoustic measurements, to insure no additional noise from the HWA and associated traverse system was measured in the acoustic spectra. The probe used was a Dantec X wire probe (55P64), where the data was taken at a sampling frequency of 25.6 kHz. The Dantec HWA hardware system used for the measurements contains an electronic low-pass filter with a cut-off frequency of 10 kHz. The wake profiles were initiated at $0.25c$ above the aerofoil till $0.25c$ below the aerofoil, at a distance of $0.25c$ from the solid aerofoil edge approximately at mid span. The increment of the measurements was large in the freestream region (1 mm), and then the increment was systematically reduced such that the region of the boundary layer was measured

Name	Length (L) [mm]	Width (w) [mm]	Spacing (d) [mm]
Baseline	20	5	1
Long	30	5	1
Short	10	5	1
Wide	20	10	1
Narrow	20	2.5	1
Large Spacing	20	5	7
Medium Spacing	20	5	3

Table 4.1: Geometric specifications and naming convention for the tested flaplet cases. The thickness of each flaplet configuration was constant at 0.18 mm.

with 0.2 mm increments. Each measurement was taken for a period of 10 s, prior to moving on to the next increment.

4.2.5 Laser Displacement Measurements

To measure the flaplet displacement within the flow, a laser displacement sensor was used. The sensor used was a Micro Epsilon optoNCDT ILD2300-200, where the frequency was set at $f = 5$ kHz. This was such that sufficient frequency resolution could be obtained to capture the oscillation without sacrificing the quality of the measurements. The sensor was placed beneath the aerofoil such that it was out of the flow of the open-jet. It was positioned in a way that the laser was directed at a point just prior to the tip of the flaplet, so that the true deflection of the tip of the flaplets could be tracked as accurate as possible. Additional care was taken to ensure that the sensor was positioned normal to the flaplets in order to make sure that the back-scattered signal can be accurately detected for signal clarity.

4.3 Results

4.3.1 Static Flaplet Response

The Eigen frequency of the flaplets needs to be determined in order to see at what frequency the flaplets will oscillate in the flow. The set-up and image processing for this response test is the same as was used in Talboys and Brücker (2018). The normalised response of the long, baseline and short flaplets is shown in Fig. 4.2, where $t^* = t \cdot \omega_n$, t

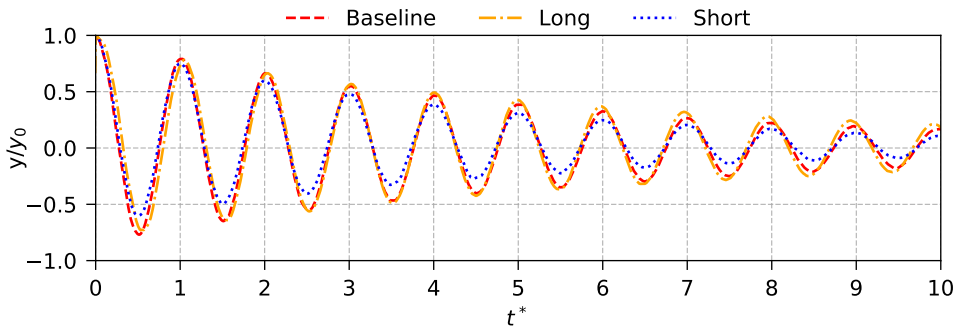


Figure 4.2: Response of the flaplets to a step input, normalised with the stating position (y_0) and the time is normalised by the measured Eigen frequency ($t^* = t \cdot \omega_n$, t is the time in seconds, ω_n is the observed Eigen frequency in Hz).

Case	Experimental	Finite Element Analysis			Estimated
	$f_{1^{st}B}$ [Hz]	$f_{1^{st}B}$ [Hz]	$f_{1^{st}T}$ [Hz]	$f_{2^{nd}B}$ [Hz]	Flutter [Hz]
Baseline	107	110	918	689	455
Long	50	45	547	284	187
Short	345	369	1702	2313	1220
Wide	105	111	494	696	343
Narrow	128	118	1879	740	488
Large S.	104	99	919	620	409
Medium S.	111	110	828	689	455

Table 4.2: Experimental Eigen frequencies, finite element analysis predictions of the 1st bending ($f_{1^{st}B}$), 1st torsion ($f_{1^{st}T}$) and 2nd bending ($f_{2^{nd}B}$) bending modes and an estimation of the flutter frequency using Eqn. (4.1) from Xin et al. (2017)

is the time in seconds, ω_n is the observed Eigen frequency in Hz, y is the displacement and y_0 is the starting position of the flaplet. Once the Eigen frequency is obtained, the Young's Modulus of the flaplets can be derived using classical cantilever beam theory. Determining the Young's modulus then allows the use of a finite element analysis (FEA) software, in the present case ANSYS, in order to predict the first torsion mode. This is when the flap response enters the flutter regime and therefore provides a limit of frequencies, above which any excitation of this mode may disturb the lock-in effect and lead to additional noise. Therefore, the range of tested flow speeds (Reynolds-number) was limited to avoid the excitation of this mode.

From Table 4.2, each of the flaplets Eigen frequencies can be seen, derived both experimentally and by using FEA. It can be observed that there is good agreement between the FEA model and the experiment. As the Eigen frequency is inversely proportional to the squared length, only the short and long flaplets should differ largely

in their Eigen frequency. It is important to note that the narrow cases show a higher Eigen frequency than expected. This is assumed to be caused by the laser-cutting process, when additional heat is introduced at the cutting edge. As a result, the Young's modulus of the narrow flaplets was seen to be slightly different to the other flaplets and was adjusted accordingly in the FEA model. When looking at the torsional mode, it can be seen that the long and the wide flaplet cases have a considerably lower torsional frequency in comparison to the other flaplets. Also by looking at the second bending modes, it can be seen that the long flaplets have a very low second bending frequency. Using the estimated flutter frequency equation given by Xin et al. (2017),

$$f_f = f_{n,1} + f_{n,2}/2 \tag{4.1}$$

where f_f is the estimated flutter frequency, $f_n, 1$ is the first bending mode and $f_n, 2$ is the second lowest bending mode (either 2^{nd} bending or 1^{st} torsional mode, whichever is lowest), it can be seen that the predicted flutter frequencies for the long and the wide flaplets are lower than the other configurations. It can be seen that the predicted flutter frequencies for the long and the wide flaplets are lower than the other configurations and it can therefore be expected that those will go into flutter at a lower Reynolds number, hence limiting the working velocity range for these cases.

4.3.2 Tonal Noise

For the current study tonal noise was seen at all three geometric angles of attack, but for brevity only the results for the reference aerofoil and the aerofoil with baseline flaplets at $\alpha_g = 10°$ are shown here. Figure 4.3 shows the narrow-band far field acoustic spectra for the chord based Reynolds number where tonal noise was observed, $250,000 \leq Re_c \leq 700,000$. Each of the spectra are spaced with 50 dB from each other for clarity. One of the key features that is observed with tonal noise is distinct frequencies overlaid on a broadband hump. These distinct peaks can be seen in all of the presented cases in Fig. 4.3. It is well known that the as the Re_c is increased, the range of the tonal peaks move to higher frequencies, hence the spectra have been scaled to with the scaling

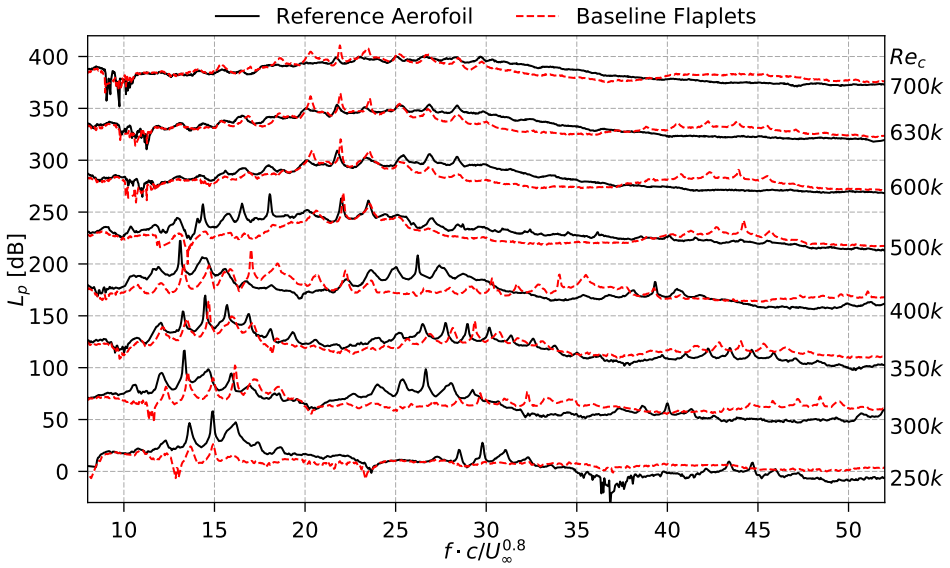


Figure 4.3: Far field narrow-band sound pressure level spectra *re* 20μPa for the reference (plain) aerofoil, focusing on the tonal noise produced at $\alpha_g = 10°$. Each of the spectra are spaced with 50 dB from each other for clarity. The frequency has been scaled with the local scaling factor of $U_\infty^{0.8}$.

factor proposed by Paterson et al. (1972) for local tonal noise. This local scaling is called 'laddering' where this scaling holds true for limited band of Reynolds number prior to jumping to another 'rung'. This can be clearly seen in the spectra obtained for the reference aerofoil, where the frequency of the tonal peaks from $Re_c = 250,000 - 400,000$ increases linearly. To further analyse this effect, Fig. 4.4 shows the frequency of the tonal peak and the associated fringe frequencies at each Re_c. The plot includes trend lines both for the local velocity-frequency scaling and for the global velocity-frequency scaling, as proposed by Paterson et al. (1972), revealing the typical 'rungs' of the ladder for both the reference and baseline case.

When comparing the reference aerofoil and baseline flaplets tonal noise, it can be seen that the flaplets indeed reduce the magnitude of the tonal noise component, consistent for the whole range of tested Reynolds numbers. In the lowest Re_c case presented, $Re_c = 250,000$, the tonal noise can be seen to be dramatically reduced by the presence of the flaplets, where the tonal peaks are only slightly more pronounced than the low frequency broadband content in the spectra. Furthermore, the tonal peaks extend to a higher velocity than the reference aerofoil due to the presence of the flaplet.

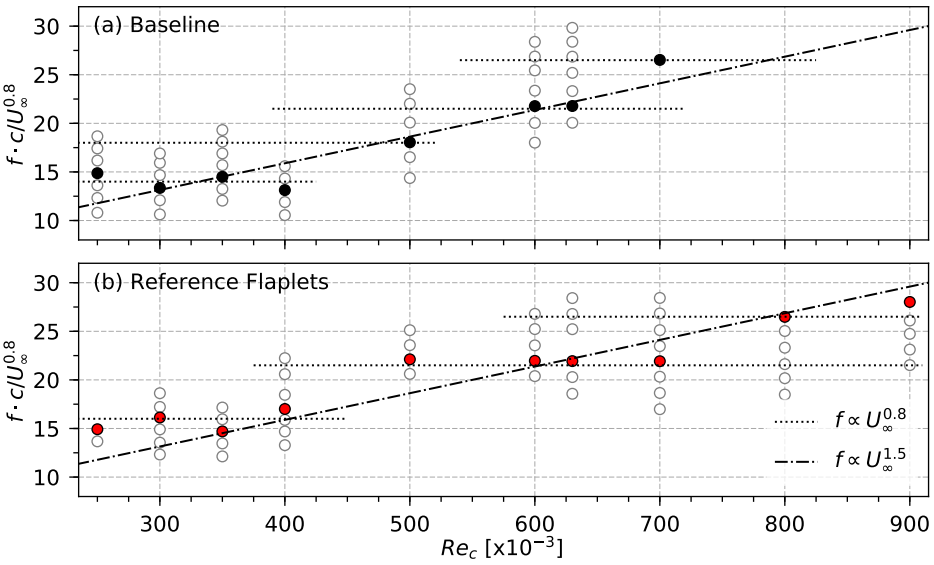


Figure 4.4: Tonal peaks (solid) and fringe frequencies (hollow) for each Reynolds number at $\alpha_g = 10°$. Global and local trend lines from Paterson et al. (1972) are also indicated.

In addition, it is visible that the spectra obtained for the reference aerofoil contain a second range of tones at twice the frequency of the first occurrence, which are the first harmonics of the tonal noise. These harmonics are much less distinct in the spectra obtained for the aerofoil with flaplets, especially at low Re_c. These findings strongly indicate that flaplets are dampening the T-S instabilities within the boundary layer. In order to observe this potential damping, a surface oil flow visualisation (SOFV) was carried out at $Re_c = 350,000$ and at $\alpha_g = 10°$. Figure 4.5, shows a composite of the SOFV on the pressure side of the aerofoil, with the left side of the image showing the reference aerofoil and the right showing the aerofoil with the baseline flaplets.

The separation bubble can be clearly seen towards the trailing edge of the foil, and on either side of the separation the flow is attached. This is due to this area being in the region where the shear layer of the core jet mixes momentum into the flow, keeping it attached. Therefore only the centre part of the aerofoil should be focused on. When comparing the separation bubble, it is immediately clear that the baseline flaplets reduce the separation bubble. The start of the bubble on the reference aerofoil is at $x/c = 0.87$ and the baseline flaplets is at $x/c = 0.89$, showing that the differences that are observed in the spectra are indeed due to the change of the separation bubble on this side of the aerofoil. This delay gives rise to a change in the acoustic feedback loop, hence the

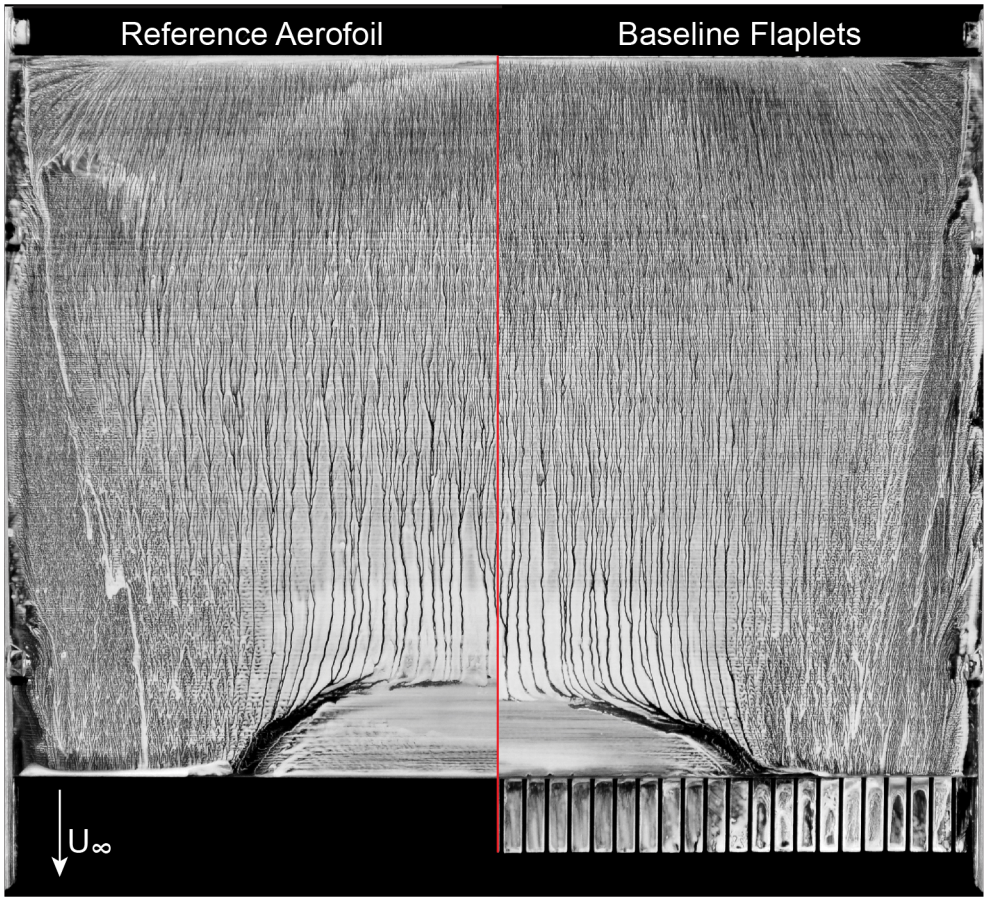


Figure 4.5: Flow visualisation comparing the pressure side of the aerofoil for the reference aerofoil (left) and the baseline flaplets (right), at $Re_c = 350,000$ and $\alpha_g = 10°$. The flow direction is indicated in the bottom left of the image.

probable cause for the slight modification of the frequency that was observed in Fig. 4.3 and the reduction in the sound pressure level.

In order to enable a better description of the effect of the flaplets on the noise generation compared to the reference aerofoil, far-field noise spectra will be shown in 1/3 octave bands in the remainder of this paper.

4.3.3 Acoustic, Hot Wire Anemometry and Vibration Results

In this section the results of the 1/3 octave band acoustic spectra, 2D sound maps, overall sound pressure level, hot wire wake measurements and laser displacement measurements will be presented in this order, in turn, for each of the geometric variations, starting with the variation in length, then width and finally the inter-spacing.

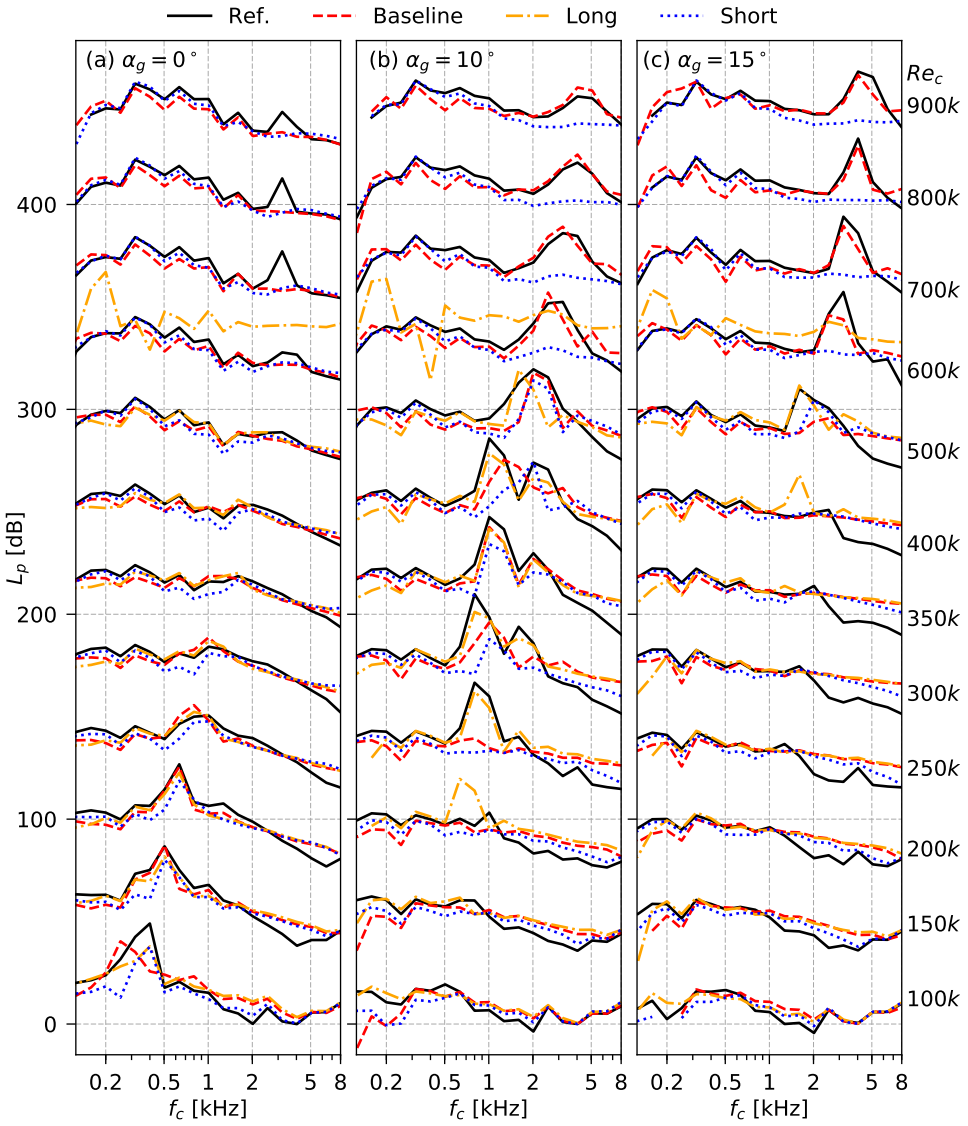


Figure 4.6: 1/3 Octave band acoustic spectra for variation in length. Each of the spectra are spaced with 35 dB from each other for clarity.

4.3.3.1 Variation in Flaplet Length

Figure 4.6 shows the acoustic 1/3 octave band spectra at three geometric angles of attack at various chord based Reynolds numbers. In order to visualise all Reynolds number cases on one plot, each spectra are incremented 35 dB from the spectrum at the previous Reynolds number. At $\alpha_g = 0°$, Fig. 4.6a, a clear tonal noise component is visible for all cases up to a Reynolds number of 250,000. It can be seen that the baseline and long flaplets have little effect on the tonal noise at this angle of attack, whereas the short

flaplets show a clear reduction in tonal noise.

What is interesting here is that there is seemingly a strong correlation of length of the flaplets and the frequency range of most efficient noise reduction, as such it will be discussed separately in Fig. 4.7.

An interesting feature can be seen at Reynolds number of 600,000, where the long flaplets show a dramatic increase in the noise level, with a peak at f_c = 200 Hz. This is when this specific geometry starts to 'flutter'. The flutter is due to the excitation of the lowest two bending/torsion modes of the flaplets. Here it can be seen in Table 4.2, that the two lowest frequency modes for the long flaplets are the first two bending modes, which leads to a predicted flutter frequency of f_f = 187 Hz. This frequency is within the f_c = 200 Hz third octave frequency band, showing good agreement with the predicted flutter frequency model from Eqn. (4.1). This can be observed at the same Reynolds number for each of the geometric angles of attack, showing that this is indeed the critical Reynolds number, where the flutter is excited for this geometry. It can also be seen that all of the flaplets increase the noise level at frequencies above 5 kHz. Again, as at low frequencies, there is a distinct order in which the noise level is increased. The most elevated levels are observed for the long flaplets, while the least comes from the short ones.

As the angle is increased to α_g = 10° (Fig. 4.6b), the emergence of tonal noise can be seen at a Reynolds number of 250,000 for the baseline case, and is present up to the highest Reynolds number tested (900,000), as previously discussed in Section 4.3.2. A similar trend as for the zero degree angle case is observed: All the flaplets show a reduction in the low frequency range and an increase at the higher frequency range, the magnitude of this modification being tendentiously higher.

The tonal noise component is in general reduced at all flaplet cases, albeit that the long flaplets only show a small reduction in comparison to the reference. Saying this, at Re_c = 600,000 and above the baseline flaplets are approximately at parity with the reference case and, interestingly, the tonal noise is completely removed for the short flaplets.

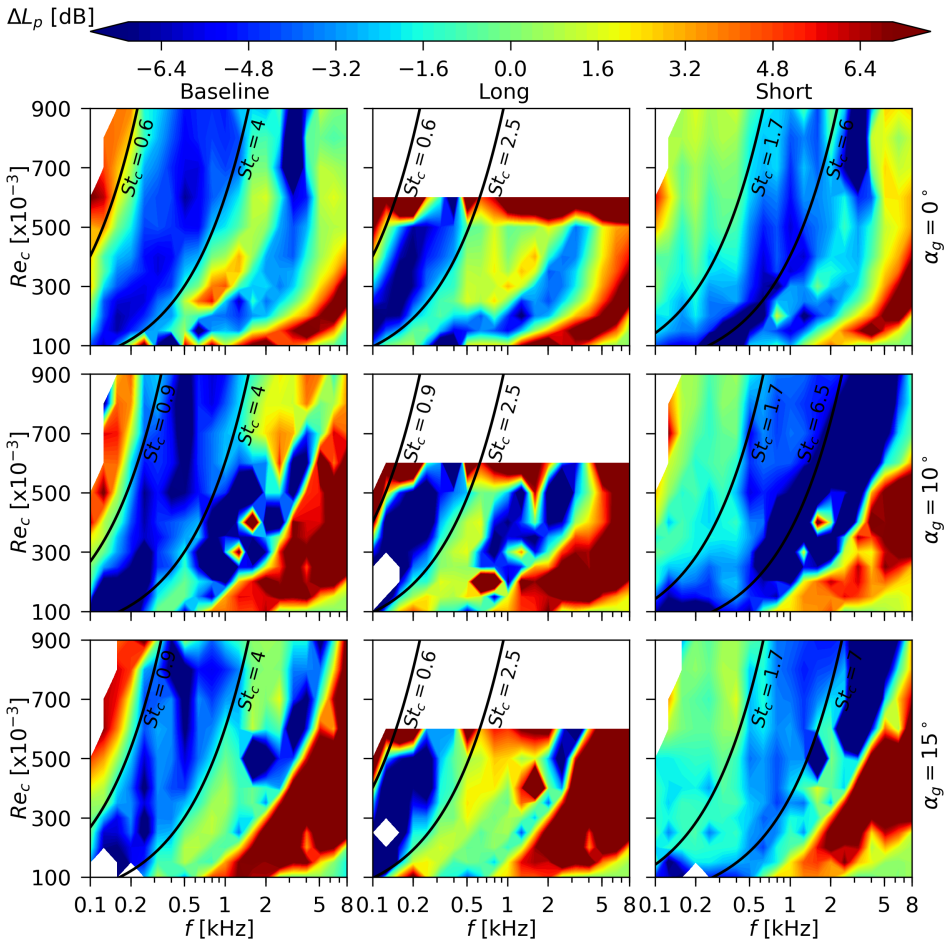


Figure 4.7: ΔL_p contours for variation in length, with the zone of maximum reduction indicated.

At the highest tested angle, $\alpha_g = 15°$, the tonal noise on the reference aerofoil starts to occur at higher Reynolds numbers. This is consistent with previous literature (Talboys, Geyer and Brücker, 2019a). All the trends that have been observed at $\alpha_g = 10°$ can also be seen at the increased angle. Again, the magnitude of the effects are increased further.

To quantify the low frequency noise reduction, Figure 4.7 shows the ΔL_p contours.The columns show the different flaplet geometries and the rows are indicating the different geometric angles of attack. Looking at the first column, for the baseline flaplets, clear zones of noise reduction and noise increase can be determined. The reduction zone can be identified by using limits of chord based Strouhal number, with the lower limit being $St_c = 0.6$ and the upper limit being $St_c = 4$. As the angle increases, the lower limit slightly increases to $St_c = 0.9$, whereas the upper limit stays the same. The magnitude of the reduction can be seen to be the most at $\alpha_g = 10°$. Increasing the angle further, still shows

the reduction zone is still there, however the magnitude of the reduction is reduced. Beyond these reduction zones at $\alpha_g = 0^\circ$ and 10°, it can be seen that there are regions of high noise increase. This high noise is due to the tonal noise effects caused by the shift in the tonal noise frequency by the flaplets, hence a seemingly large noise increase. This effect can be seen for all flaplets at these angles. When the flaplets length is increased, the bounds of the reduction zone can be seen to have reduced, where the maximum limit is $St_c = 2.5$. This means that a lower band of frequencies can be reduced. As was seen in the baseline case, the magnitude of reduction was seen to increase at $\alpha_g = 10^\circ$ and then slightly reduce at $\alpha_g = 15^\circ$. Here we should remind the reader, that at $Re_c = 600,000$ the long flaplets went into resonance, hence the spectra for Re_c greater than this are not available for this contour. Finally, the short flaplets again cause a change to the reduction zone, where the bounds have increased to $St_c = 6 - 7$ depending on the α_g. It should be noted that due to the tonal noise component these bands could be different if there were no tonal noise component (i.e. just turbulent boundary layer noise) but investigating this is out of scope of this publication and is left as future work. As was previously mentioned in the discussion of Fig. 4.6, the magnitudes of the reductions also seem to differ with the different flaplet length. It can be clearly seen that the long flaps at $\alpha_g = 10^\circ$ show significant reduction in this low frequency band with a maximum reduction of up to 8 dB and an average of approximately 5 dB, whereas the baseline flaplets show reductions of approximately 4 dB. The shortest flaplets show the least reduction, within this low frequency zone, where the average reduction is approximately 3 dB.

The mechanism of this reduction is not totally clear and should be investigated in further detail with the use of simultaneous particle image velocimetry and acoustic measurements. However the authors have two concepts of thought on the source of the reduction. The first is the hypothesis of the global flow modification effect documented in Talboys and Brücker (2018) (flaplets act as pacemaker), which could play an important role in the stabilisation of the T-S waves. Because of the different Eigen frequencies of the flaplets, they are modifying the wake with different frequencies, hence the different acoustic frequency reductions. This type of vortex shedding noise

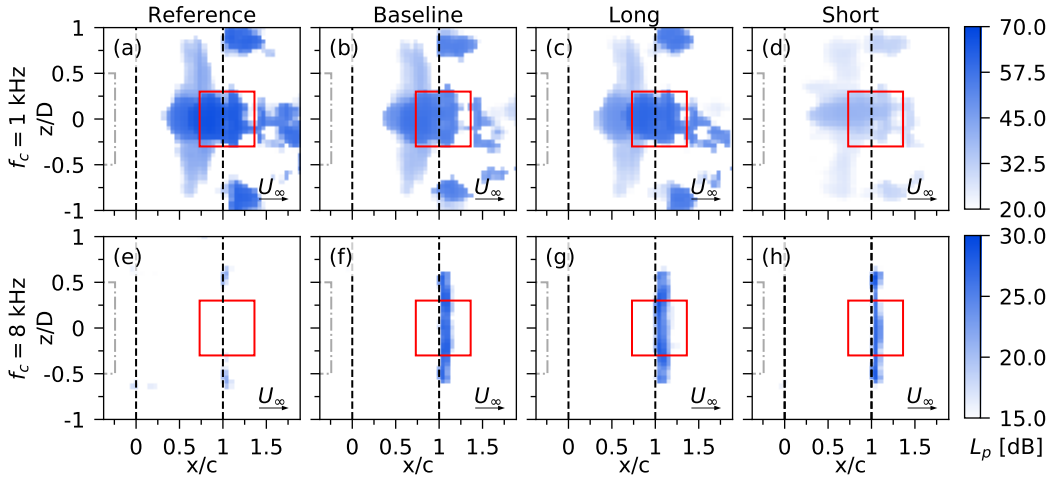


Figure 4.8: 2D sound maps as the length is varied, at Re_c=350,000 and $\alpha_g = 10°$. (a–d) shows the frequency band, f_c=1 kHz and (e–h) shows the frequency band, f_c = 8 kHz. (- · - ·) indicates the jet nozzle, (- - -) indicates the aerofoil, (——) indicates the interrogation region for acoustic spectra.

reduction has also been observed by Geyer et al. (2019), where they used a cylinder with flexible flaplets on the aft part of the cylinder.

The other hypothesis is that it is due to the shape of the flaplet geometry, where the flaplets are effectively 'slit-trailing edge serrations'. A somewhat similar low frequency noise reduction was observed by Gruber, Azarpeyvand and Joseph (2010) with cardboard slit serrations, both experimentally and analytically. However the analytical approach was able to determine multiple frequencies that could be reduced, whereas their experimental results only really showed one reduction zone, similar to the results herein. We should note here that small vibrations from the cardboard-type serrations cannot be excluded in their experiments in a similar fashion as the flaplets herein, as the observed effect is already visible for vibration amplitudes as small as 100-200 μm. Furthermore, their noise reduction was focusing on the broadband noise while the flaplets herein clearly address the tonal noise components. So, a definite conclusion cannot be drawn, rather we assume that both mechanisms are involved in the overall noise attenuation effect.

In order to view the location of the dominant acoustic sources, sound maps can be used. These maps are shown as sound pressure levels on a discretised grid that can be interrogated to observe certain noise sources in certain frequency bands. These sound

maps are presented as plan views of the test set-up, and in each of the plots the nozzle exit, leading and trailing edge and the spectral integration zone are indicated.

Figure 4.8 shows such 2D sound maps obtained at Re_c = 350,000 and α_g = 10° for the frequency bands with centre frequencies f_c of 1 kHz and 8 kHz respectively. This specific testing condition has been chosen as a clear tonal peak can be seen in the acoustic spectra for the reference case, which therefore forms a good basis to compare any tonal noise reduction.

Tonal noise has been previously shown to be reduced with the presence of flaplets. From Fig. 4.8a it can be seen that the noise source starts from the chordwise position x/c ≈ 0.3 extending beyond the solid trailing edge and is located in the mid-span location of the aerofoil. It must be noted here that there are small regions of increased noise at either side of this large noise source. These noise sources are due to the interaction of the shear layer of the wind tunnel, which is highly turbulent, with the trailing edge of the aerofoil. Looking at all the flaplet cases it can be seen that with the baseline and long flaplets (Fig. 4.8b-c) there is only a small reduction of the tonal noise, whereas, in contrast, the short flaplets (d) reduce the tonal noise significantly.

When investigating the locations of the acoustic sources with respect to the observed high frequency noise increase, the sound maps at a 1/3 octave band with f_c = 8 kHz are better suited than those obtained at 1 kHz. As seen in Fig. 4.8e, at the higher frequency the reference case now only shows noise sources where the jet shear layer interacts with the leading edge and trailing edge of the aerofoil. It can then be seen for the flaplet cases that somewhat weaker noise sources appear directly aft of the solid trailing edge and along the length of the flaplets, which correspond to the increase in noise levels seen in the acoustic spectra in Fig. 4.6. This is thought to be due to the oscillatory motion of the flaplets giving rise to an additional acoustic source. It can be seen that this source is a function of the flaplets surface area, as there is a clear difference in the extension of the source from the trailing edge as the flaplets increase in length, where (h), corresponding to the short flaplets, is the smallest region and the largest area is seen in (g) which is for the long flaplets.

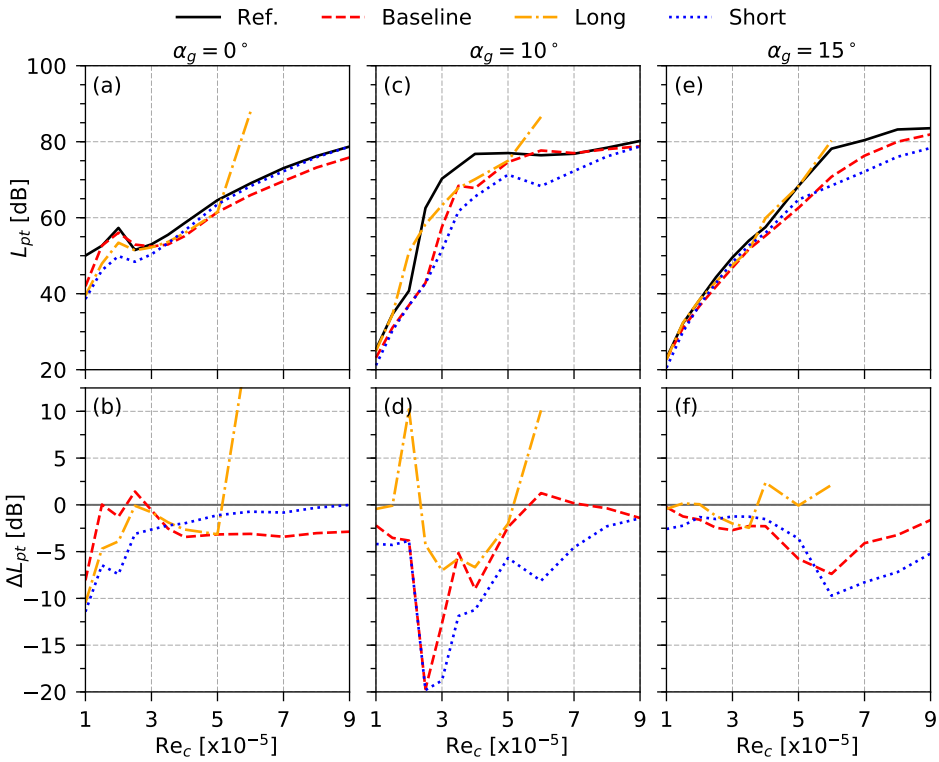


Figure 4.9: OSPL, denoted as L_{pt}, and Delta OSPL, ΔL_{pt}, for variation in flaplet length.

As a means to investigate the overall acoustic effect of the flaplets, the overall sound pressure level (OSPL) has been computed for each of the cases according to

$$L_{pt} = 10 \log_{10} \left(\sum_{f_c=0.2 \text{ kHz}}^{8 \text{ kHz}} 10^{\frac{L_{pi}}{10 \text{ dB}}} \right) \text{ dB}, \tag{4.2}$$

where L_{pi} is the sound pressure level at the i^{th} centre frequency (f_c). In order to obtain an easier appreciation of the magnitude of the differences between the cases, the difference between the reference case and the different flaplets cases has also been calculated as

$$\Delta L_{pt} = L_{pt,\text{flaplet}} - L_{pt,\text{reference}}. \tag{4.3}$$

The results are shown in Figs. 4.9a-c-e.

At $\alpha_g = 0°$, Fig. 4.9a, it can be seen that as the Reynolds number increases, the general trend is that the OSPL also increases. There is a slight reduction in OSPL from Re_c= 200,000 – 250,000, which is due to the tonal noise component being reduced at this condition. When comparing the flaplet cases to the reference case, Fig. 4.9b, it can be seen that at the lowest Reynolds numbers up to 350,000, the shortest flaplets

show the best overall reduction. This reduction is of the order of 5 to 10 dB. After this point the OSPL of the shortest flaps tends back to the reference case. The OSPL for the baseline flaplets, on the other hand, is initially approximately the same as that for the reference case and then tends to a reduction of ~3.5 dB from a Reynolds number of 400,000 onward. The long flaplets show reasonable overall reductions at low Reynolds number until the sudden noise increase occurs at Reynolds numbers above 500,000, as can be seen in the acoustic spectra. At $\alpha_g = 10°$, Fig. 4.9c, the reference case leads to a sudden increase in OSPL at Re_c= 250,000. This is due to the prevalent tonal noise that dominates the spectra. Once the Reynolds number reaches 400,000, the OSPL plateaus for the remaining tested Reynolds numbers. Immediately it can be seen that for the baseline and short flaplet cases, the OSPL is lower across the whole range of Reynolds numbers. The largest reduction of approximately 20 dB can be seen at Re_c=250,000 and this is due to the delay in the occurrence of tonal noise, which can be clearly seen in the acoustic spectra (Fig. 4.6b). At Reynolds numbers beyond 500,000 it is seen that the baseline flaplets do not show too much, if any, OSPL reduction, which is due to the tonal noise in both the reference and baseline cases being approximately the same. As was seen at $\alpha_g = 0°$, the OSPL for the short flaplets tends towards the value for the reference aerofoil as the Reynolds number increases. Increasing α_g further to 15° reveals similar effects as those seen for both lower angles, although the effects are less pronounced. At Reynolds numbers below 400,000 it can be seen that both the short and baseline flaplets show an OSPL reduction of around 2.5 dB, after which the reduction increases. This is again due to the lower tonal noise component observed with the flaplets.

In order to observe the effect of the flaplets on the wake flow, hot wire measurements were taken at a streamwise distance of $0.25c$ aft the solid trailing edge. Therefore, no offset has been taken into account for the flaplets length. Figures 4.10a-c-e show mean streamwise velocity profiles for each of the flaplets of varied length at each of the tested angles of attack at $Re_c = 200,000$. At $\alpha_g = 0°$, the profile is symmetric about the $y/c = 0$ line. This is expected as the aerofoil is symmetric itself, the wake deficit should also be symmetric here. As the angle is increased, the wake profiles become thicker on the suction side of the aerofoil ($y/c > 0$), which is due to the thickening of the boundary

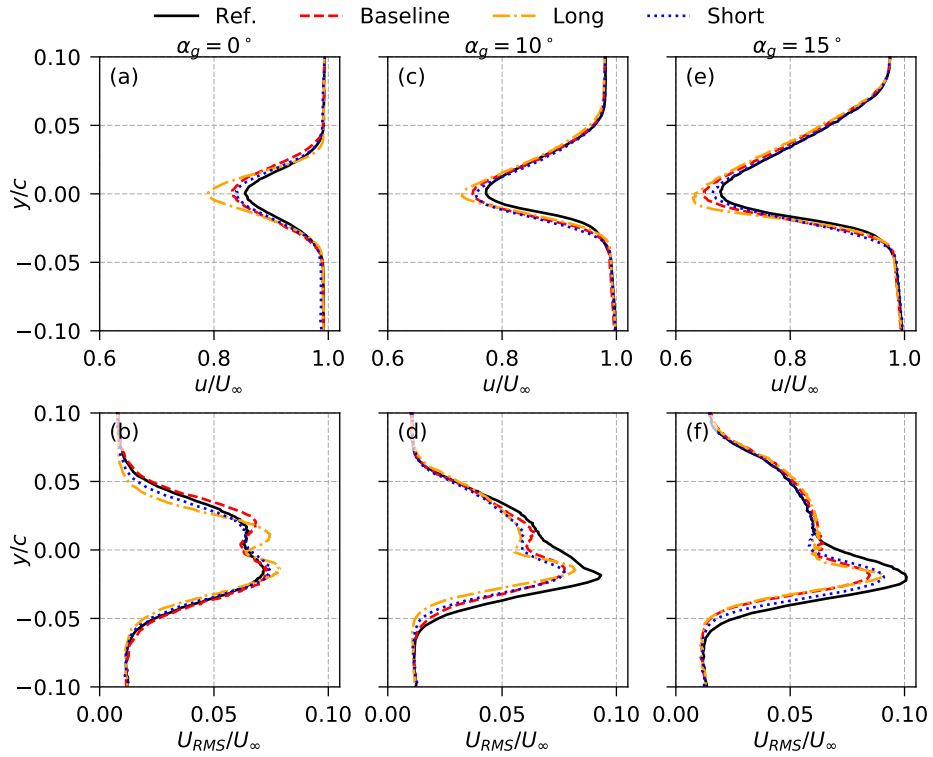


Figure 4.10: Mean and RMS wake profiles of the streamwise velocity component at Re_c = 200, 000 for variation in length.

layer on this side of the aerofoil. In addition, the absolute value of the velocity deficit is also seen to increase at higher angles, from a value of $u/U_\infty = 0.85$ for the reference aerofoil at $\alpha_g = 0^\circ$ to a value of around 0.7 for the same aerofoil at $\alpha_g = 15^\circ$ It can be seen that at each of the angles the largest velocity deficit is visible for the long flaplets followed by the baseline and then the short flaplets. This is a logical conclusion as there was no offset for the flaplet length, hence the tip of the long flaplet was physically closer to the probe. A more discernible difference between flaplets and reference aerofoil can be seen when looking at the streamwise RMS profiles as shown in Figs. 4.10b-d-f. At $\alpha_g = 0^\circ$ it can be seen that all RMS profiles are similar, even with those obtained for the baseline and the long flaplets showing a small increase compared to the reference aerofoil. As the angle increases to $\alpha_g = 10^\circ$, Fig. 4.10d, a peak in the RMS velocities can be seen on the pressure side of the aerofoil. This is very evident for the reference aerofoil and is attributed to be due to the high levels of turbulence caused by the separation and reattachment of the separation bubble on the pressure side of the aerofoil close to

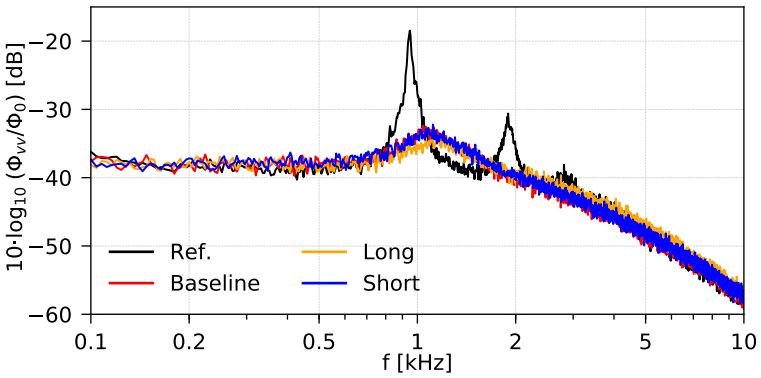


Figure 4.11: Fluctuating vertical velocity component, v', turbulence spectra (Φ_{vv}) normalised with a nominal $\Phi_0 = 1$ m^2/s at the peak RMS point in wake profiles at $\alpha_g = 15°$ and $Re_c = 200,000$ for variation in length.

the trailing edge. All of the flaplet cases show some reduction in the RMS velocities and are of similar amplitude. Increasing the angle further, again shows a similar level of reduction for each of the tested cases. Therefore it is clearly seen that the flaplets indeed modify the turbulent fluctuations in the wake at $\alpha_g = 10°$ and $15°$. Interestingly, there also does not seem to be a length dependency in this reduction.

In order to obtain a better understanding about how the flaplets are modifying the wake structures, spectra of the turbulent velocity fluctuations, taken at the point of maximum RMS observed in Fig. 4.10f, will be analysed. This point was specifically chosen as it corresponds to the approximate position of the centre of the shed vortices. Also, an angle of $\alpha_g = 15°$ was selected for this analysis, as the velocity spectra at the lower angles showed influences from the tonal noise observed in the acoustic spectra, and as such the trends were not as clear as those shown in Fig. 4.11. The spectra correspond to the vertical fluctuating velocity component, v', as this can be assumed to be more sensitive to spanwise structures, such as shed vortices from an aerofoil. When looking at the results for the reference aerofoil, it can be clearly seen that there is a strong dominant peak at 950 Hz, and the subsequent secondary and tertiary harmonics at 1850 Hz and 2850 Hz respectively. Observing the resulting velocity spectra obtained for the three flaplet cases immediately reveals that there is a clear, almost complete reduction in this peak. The remaining hump has been shifted to a slightly higher frequency, $\approx$ 1100 Hz, and it is more broadband in nature. This broadband

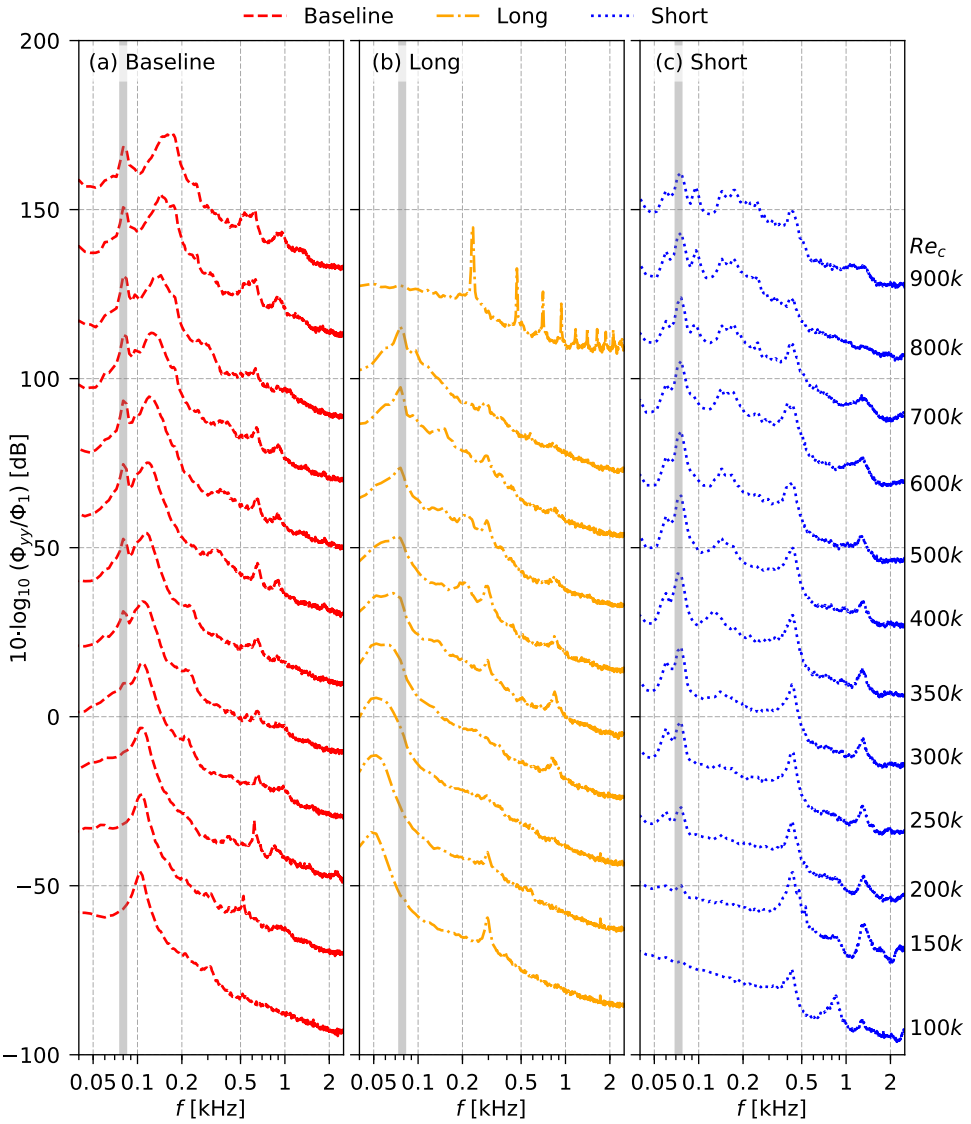


Figure 4.12: Spectra of the laser displacement measurements, (Φ_{yy}) normalised with a nominal $\Phi_1 = 1$ m^{2}s at $\alpha_g = 0°$ for variation in length.

hump is more or less identical for the baseline and short flaplets, with the shedding being slightly reduced for the longest flaplets.

In a subsequent experiment the motion of the flaplets was non-intrusively measured using a laser displacement sensor. Using this technique enlightens the motion of a single flaplet at the different tested Reynolds numbers; herein the results just at $\alpha_g = 0°$ are presented. Figure 4.12, shows the spectra of the motion of the flaplets as they oscillate in the flow. It should be noted here that a small vibration from the model could be detected and the frequency of this oscillation has been indicated on Fig. 4.12 as a vertical

grey bar at $f \approx 80$ Hz. The RMS of the model vibration (y_{rms}), measured at $x = 0.9$c and at $Re_c = 900,000$, was $y_{rms} = 0.015$ mm, and a maximum peak to peak vibration of $y = 0.1428$ mm. In comparison the corresponding y_{rms} of the baseline flaplets at the same condition was $y_{rms} = 0.060$ mm, and a maximum peak to peak of $y = 0.611$ mm. Fig. 4.12a, shows the results for the baseline flaplets, and it can be immediately seen that at the lowest Reynolds number there is a clear peak just above $f = 110$ Hz, and this corresponds to the Eigen frequency of the flaplets, as can be seen in Table 4.2. As the Reynolds number increases the flaplet oscillation persists, however it can be seen that the frequency of oscillation becomes more broadband and increases in frequency. It is also interesting to observe a smaller secondary peak at $f \approx 700$ Hz, which when referring back to Table 4.2, can be seen as the secondary bending mode frequency. At the highest two Reynolds numbers this peak becomes broader, which could indicate that the flaplets are close to their critical velocity, or close to flutter.

When looking at the long flaplets, Fig. 4.12b, the Eigen frequency peak can be clearly seen at $f \approx 50$ Hz. In a similar way as the baseline flaplets, the frequency of the oscillation increases with Reynolds number. Here it should be noted that the exact frequency of the oscillation at the higher Reynolds numbers cannot be clearly distinguished from the model vibration. Looking at the second peak, it is again coincident with the second bending mode frequency ($f = 284$ Hz) and it can be seen to persist with increasing Reynolds number. As was seen in the acoustic spectra, the long flaplets once again go into flutter at high Reynolds numbers. The frequency of the flutter here is measured to be $f = 230$ Hz, which is in reasonable agreement with the predicted flutter frequency ($f_f = 187$ Hz).

Finally in Fig. 4.12c, the short flaplets are also observed to oscillate at their Eigen frequency across all Reynolds numbers.

An interesting difference here is that the frequency of oscillation stays more or less constant throughout the entire Reynolds number range, which is in stark contrast to the other two lengths, which both increase their oscillation frequency with Reynolds number, as can be seen in Fig. 4.13. This could indicate that here the Eigen frequency

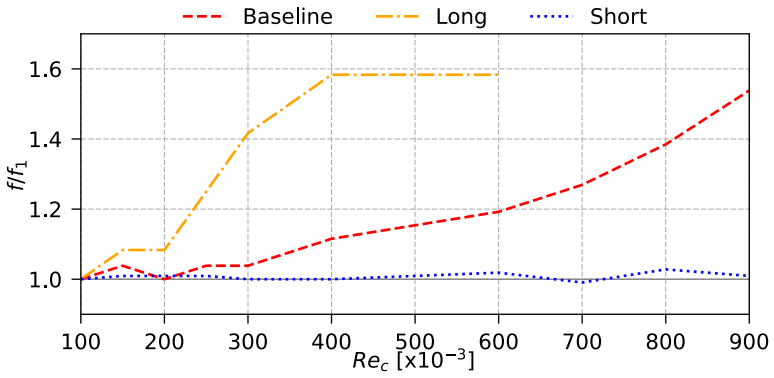


Figure 4.13: Normalised flapping frequency, with the respective Eigen frequency f_1, as Reynolds number increases at $\alpha_g = 0°$ for variation in length.

is too high to lock-in with structures in the flow, whereas the other length are able to lock-in with some low frequency structures in the flow.

4.3.3.2 Variation in Flaplet Width

The next parameter varied was the spanwise width of the flaplets. At $\alpha_g = 0°$, Fig. 4.14, it can be seen that for the cases up to Re_c=500,000 the low frequency reduction is most prominent when the wide flaplets are attached. This is followed by the baseline flaplet and then the narrow flaplets. For higher Reynolds numbers, the wide flaplets sound pressure level gradually increase above that of the reference case in the low frequency region, and then at Re_c = 700,000 the flaplets begin to flutter in a similar manner to the long flaplets. The frequency of the flutter heard in the acoustic spectrum here was in the f_c = 250 Hz band, which is in reasonable agreement with the predicted flutter frequency in Table 4.2, f_f = 343 Hz. When observing the high frequencies, the reverse of the low frequency effect is observed, where the wide flaplets show the largest noise increase, followed by the baseline and the narrow flaplets. This is assumed to be due to the narrow flaplets being able to more successfully disrupt the small scale structures (due to their geometrical size) and vice versa for the low frequency reduction and the wide flaplets.

At $\alpha_g = 10°$, the low frequency reduction of the wide flaplets is comparable to that of the baseline flaplets, whereas the high frequency increase for the wide flaplets is still higher than that of the baseline flaplets. When tonal noise occurs, it can be seen that all the cases cause a delay and once again show a reduction. It is important to note that

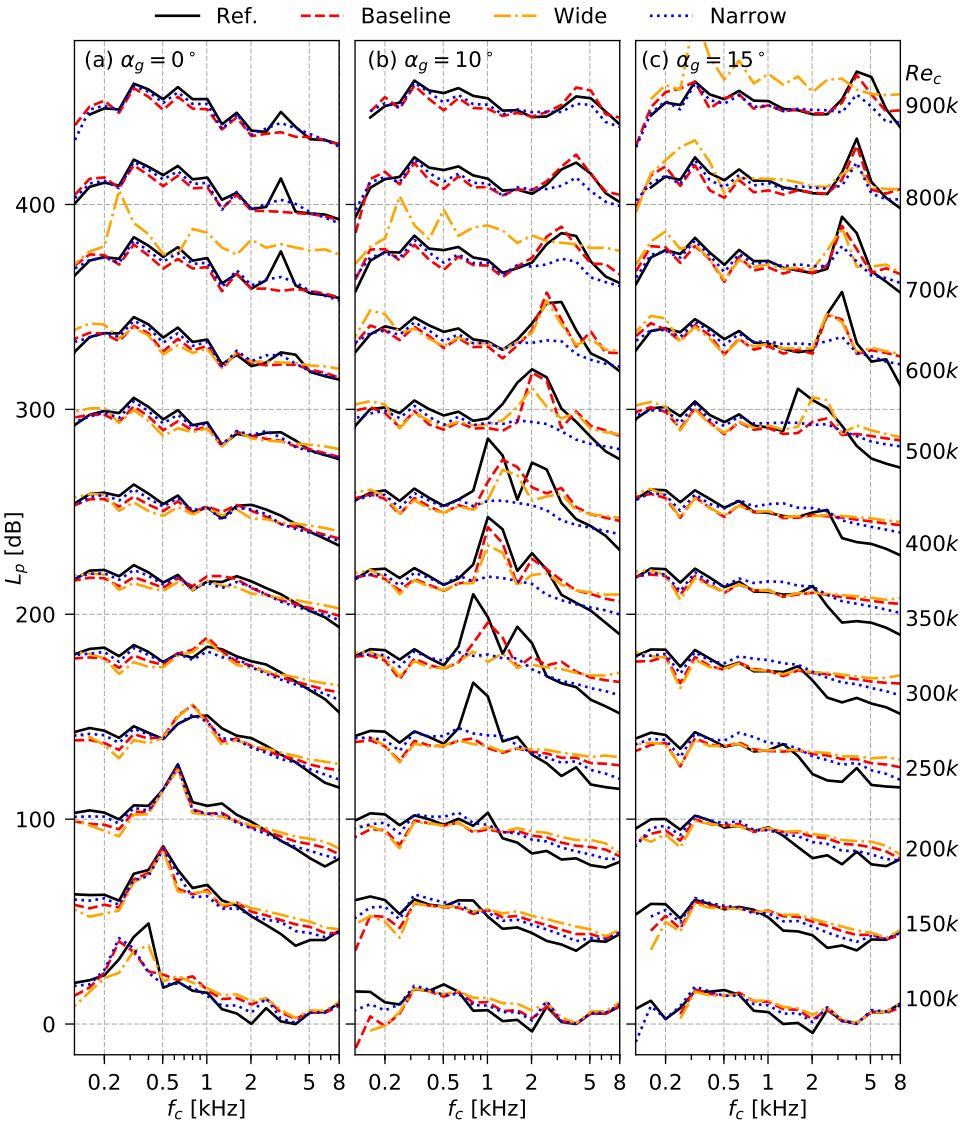


Figure 4.14: 1/3 Octave band acoustic spectra for variation in width. Each of the spectra are spaced with 35 dB from each other for clarity.

the narrow flaplets do not show any tonal noise across the whole Re_c range. This is indicating that the narrow elements severely disrupt the acoustic feedback loop and the instabilities within the boundary layer on the pressure side of the aerofoil. Increasing the angle to $\alpha_g = 15^\circ$ yields similar trends to those at lower angles. The exception is that the wide flaplets reach a higher Reynolds number before they go into flutter.

When looking at the ΔL_p contours in Figure 4.15, it can be seen that the regions of low frequency reduction are the same for all of the width cases at all angles of attack. The difference is that the magnitude of the reduction is clearly highest with the wide flaplets

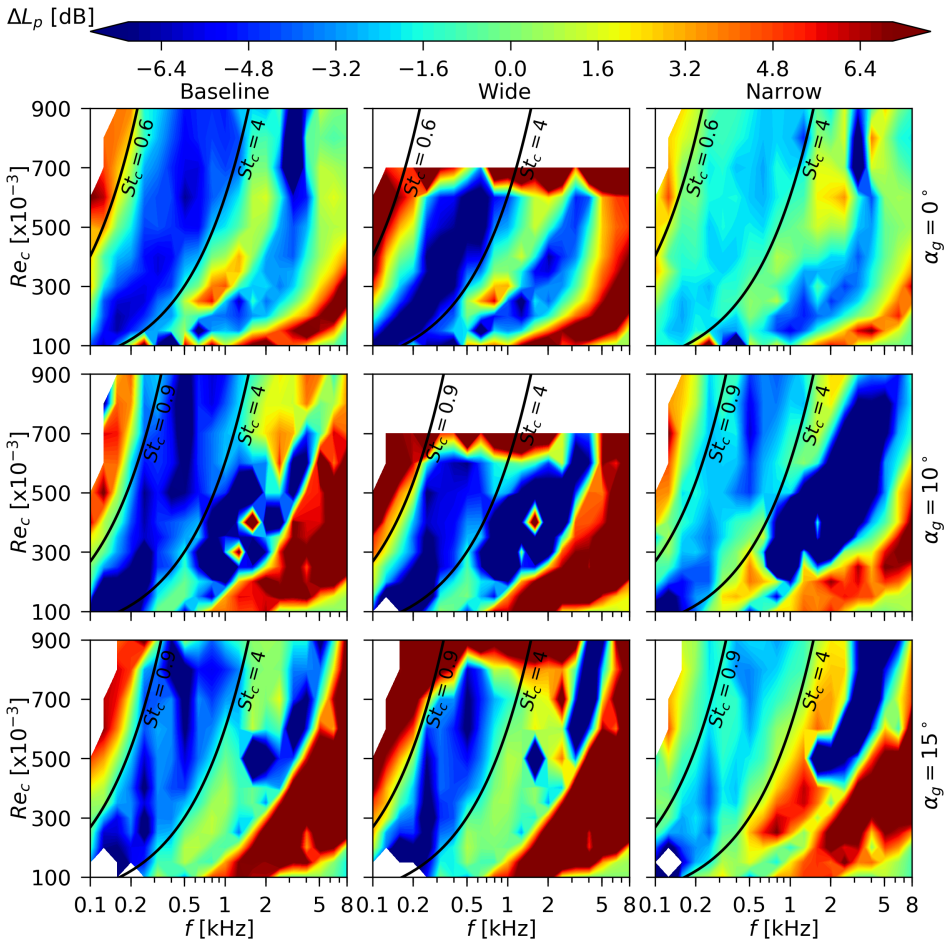


Figure 4.15: ΔL_p contours for variation in width, with the zone of maximum reduction indicated.

and lowest with the narrow flaplets. This is showing that the width plays a strong roll in the noise reduction at these low frequencies, whereas the length shifts the reduction zones as was seen in Fig. 4.7. This trend of increased magnitude of reduction when the width increases was also observed by the analytical model of Gruber, Azarpeyvand and Joseph (2010) for slitted serrations, hinting that indeed the geometry of the flaplets does indeed play a key role in this low frequency reduction.

When looking at the sound maps for this geometric variation, Fig. 4.16, at f_c=1 kHz the clear tonal noise reduction that was seen in Fig. 4.14b is seen with both the wide (c) and narrow (d) flaplets. The narrow flaplets show a significant reduction of up to 40 dB. At f_c=8 khz, it can be clearly seen that the width of the flaplets has a strong effect on the high frequency acoustic scattering. The wide flaplets (g) show a strong acoustic source across their surface, the strength of which decreases with reducing

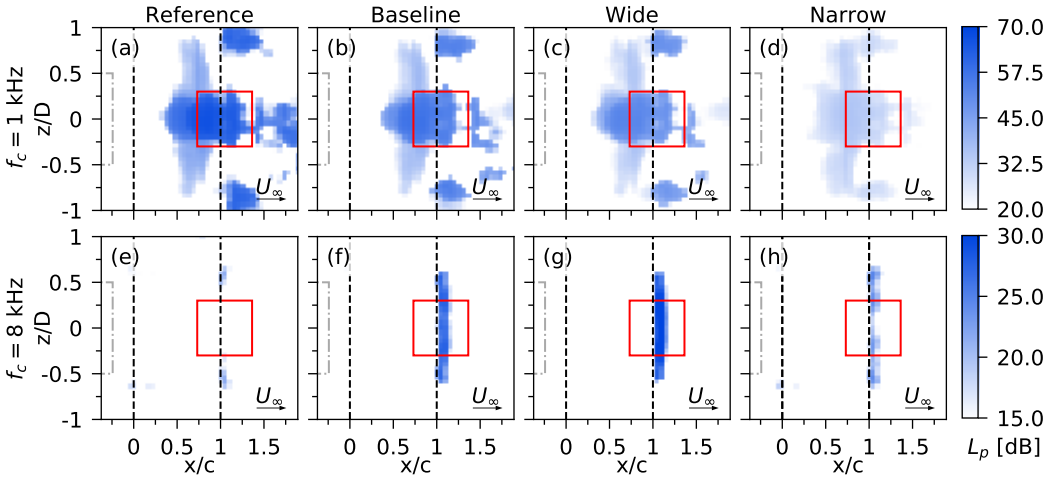


Figure 4.16: 2D sound maps as the width is varied, at Re_c=350,000 and $\alpha_g = 10°$. (a–d) shows the frequency band, f_c=1 kHz and (e–h) shows the frequency band, f_c = 8 kHz. (- - -) indicates the jet nozzle, (- - -) indicates the aerofoil, (——) indicates the interrogation region for acoustic spectra.

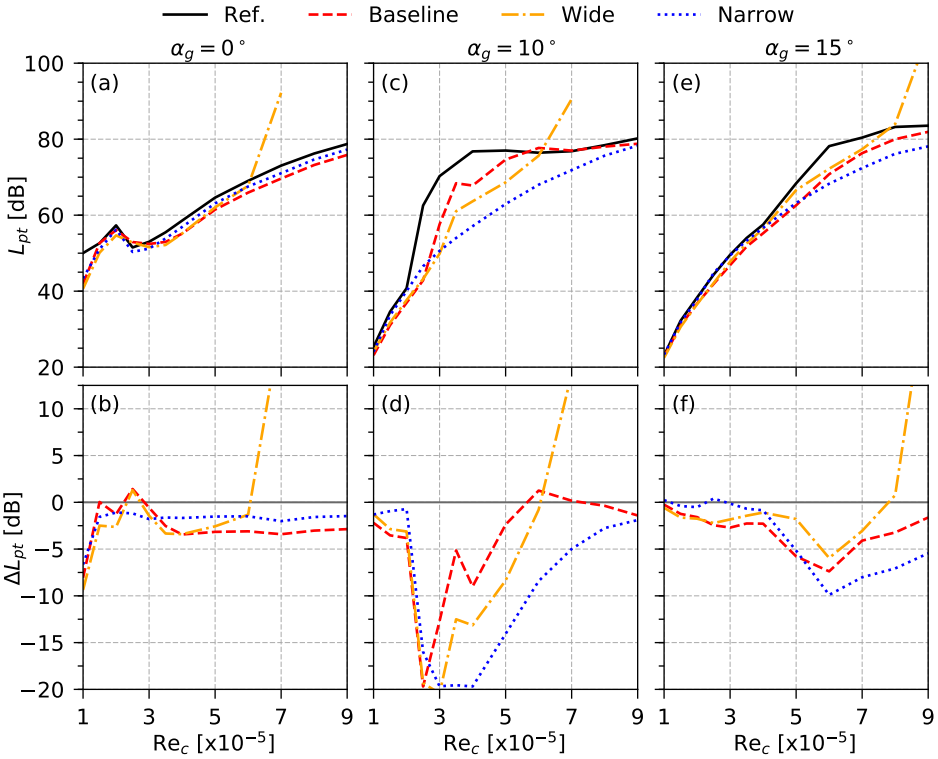


Figure 4.17: OSPL, denoted as L_{pt}, and Delta OSPL, ΔL_{pt}, for variation flaplet in width.

flaplet width, yielding a significantly lower acoustic source for the narrow flaplets (h) which is almost 15 dB lower than for the wide flaplets. This again is showing that this high frequency noise is a function of the flaplet surface area.

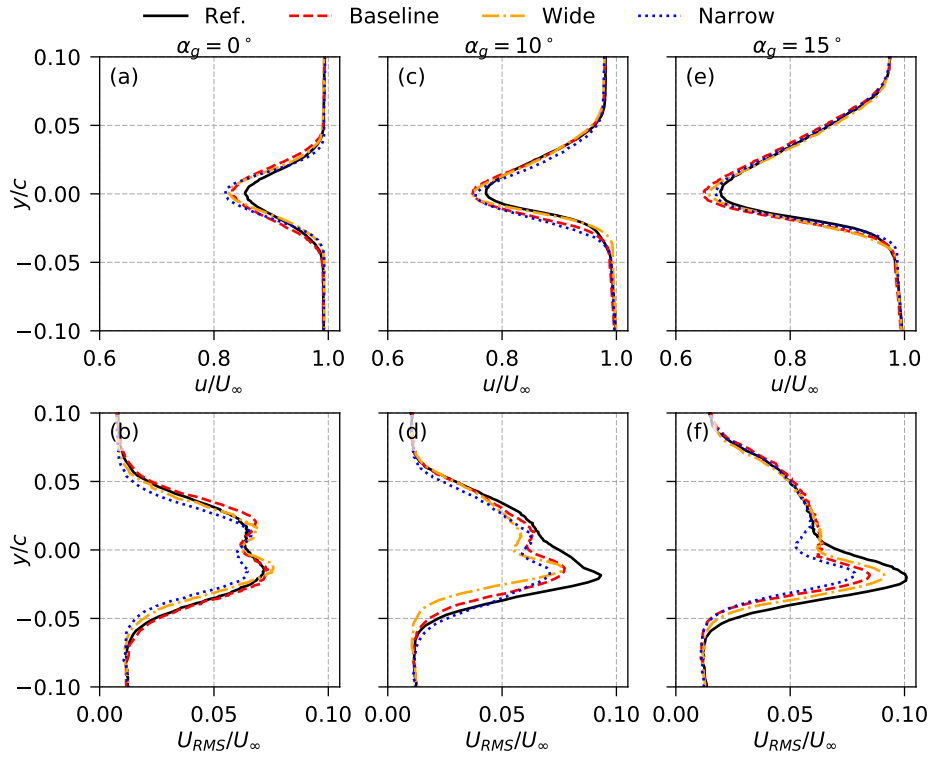


Figure 4.18: Mean and RMS wake profiles of the streamwise velocity component at Re_c = 200, 000 for variation in width.

When looking at the ΔOSPL at $\alpha_g = 0°$, Fig. 4.17b, the narrow flaplets show a constant reduction of 2 dB across most of the tested velocity range. The wide flaplets show a similar trend as the baseline flaplets, but at each Reynolds number below 400,000 there is more of a reduction. This corresponds to the greater low frequency reduction observed in Fig. 4.14a. Of course this trend ceases as the wide flaplets start to flutter. At $\alpha_g = 10°$, it can be seen that for the low Reynolds number cases, up to Re_c = 250,000, the narrow flaplets are not as efficient as the baseline and wide flaplets. However after this point, when tonal noise is present, the narrow flaplets significantly outperform all other flaplet cases, with maximum reductions in the order of 20 dB observed. As the tonal noise disappears for the reference aerofoil, the noise reduction tends towards 2.5 dB. Reductions of the OSPL can also be seen for the baseline and wide flaplets due to the slight suppression of the tonal noise component and low frequency reductions. As the angle increases further to $\alpha_g = 15°$, reductions can be seen for all flaplets, and again the maximum reductions are visible when tonal noise is present on the reference aerofoil.

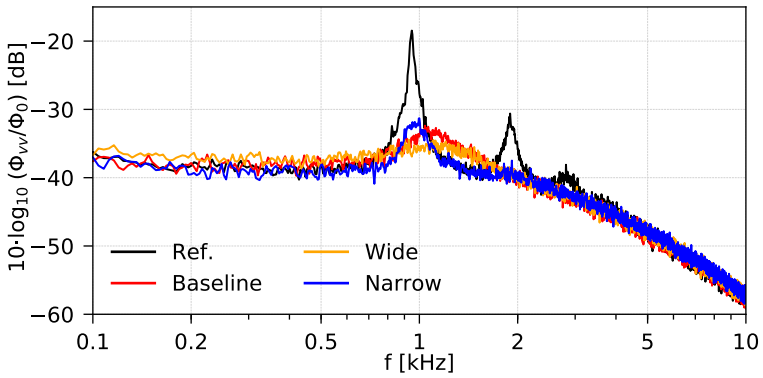


Figure 4.19: Fluctuating vertical velocity component, v', turbulence spectra (Φ_{vv}) normalised with a nominal $\Phi_0 = 1$ m^2/s at the peak RMS point in wake profiles at $\alpha_g = 15°$ and $Re_c = 200,000$ for variation in width.

When looking at the hot wire measurement results, the mean profiles in Figs. 4.18a-c-e show that the flaplets all lead to a similar wake deficit. Comparing the results with the wake deficit differences observed in Section 4.3.3.1 for the flaplets of varying length leads to the conclusion that the differences there are only due to the geometrical variation of the length and not of the width. When looking at the RMS velocity profiles in Figs. 4.18b-d-f, an interesting result can be seen in Fig. 4.18f, where there is a clear order of the magnitude of the RMS velocity on the pressure side of the aerofoil. It can be seen that the narrow flaplets dampen the turbulence in the wake most effectively, whilst the wide flaplets dampen the least. Nevertheless, there is still a moderate reduction in comparison to the reference aerofoil.

Figure 4.19 then shows turbulence spectra measured in the wake. A clear peak is visible at ≈ 0.95 kHz for the aerofoil with narrow flaplets. As the width of the flaplets is increased to the baseline width, it can be seen that the width of this peak increases as well, while the peak amplitude decreases. This trend continues, until the peak is almost completely removed for the aerofoil with wide flaplets. In order to get a more detailed understanding of the wake modification, the energy per mass unit associated with the vortex shedding, E_{vs}, will be compared for the different cases. This is simply done by calculating the integral of the velocity spectra for the frequency band that contains the peak according to:

$$E_{vs} = \int_{f_{vs,L}}^{f_{vs,U}} \Phi_{vv}(f)\ df, \tag{4.4}$$

where $f_{vs,U}$ and $f_{vs,L}$ are taken to be ± 200 Hz from the peak in the spectra and Φ_{vv} is the result of the fast Fourier transform (FFT).

It must be noted here that it is only feasible to compare the different flaplet cases with each other, but not with the reference aerofoil without flaplets. This is due to the fact that the distance between the hot wire measurement location and the point where the vortices are shed is different, as the distance from the solid trailing edge was kept constant and no additional offset was made for the flaplet length (by the same logic, the integral was not computed for the varying length case to avoid any incorrect conclusions).

The resulting energy associated with the vortex shedding is 0.158 m^2s^{-2} for the baseline flaplets, 0.107 m^2s^{-2} for the wide flaplets and 0.139 m^2s^{-2} for the narrow flaplets. As was expected, the energy is the lowest for the wide flaplets. However, the energy for the reference flaplets is higher than that of the narrow flaplets. This is due to the fact that the magnitude of the observed peak is approximately the same as that for the baseline flaplets, while the peak width is much greater for the baseline case. Thus, the energy is seen to be higher with the integration limits used. In total, all the flaplets effectively reduce the vortex shedding, and as the width of the peak is increased, the vortices seem to decay faster. A similar observation was made by Yu and Yang (2020) in their simulation.

When looking at the flaplet oscillation spectra, Figure 4.20, it can be seen that all the flaplets have a main peak at their Eigen frequency, which all are at $f \approx 110$ Hz for this geometric variation due to them all having the same length as each other. The main difference with these flaplets is the 1st torsional mode frequency, as seen in Table 4.2, where the wide flaplets have a much lower torsional frequency, $f_{1^{st}T} = 494$ Hz, in comparison to the baseline and narrow flaplets. This torsional frequency can be seen to emerge in Fig. 4.20b, from $Re_c = 350,000$ onwards. This frequency can be seen to increase as the Reynolds number is increased. In the acoustic spectra it was observed that the wide flaplets went into flutter at $Re_c = 700,000$, and the results in Fig. 4.20 show that the flutter here is due to the coupling of the torsional and bending modes. It must

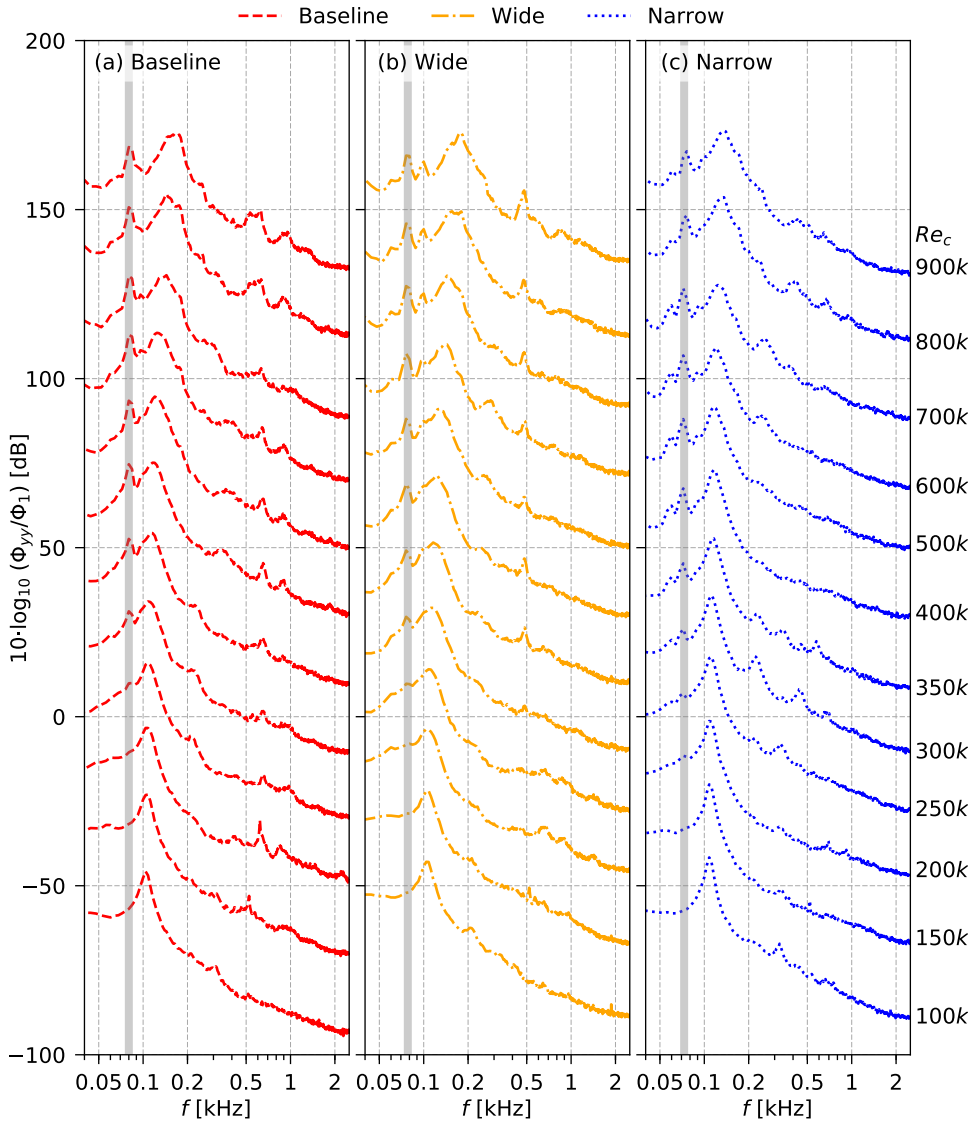


Figure 4.20: Spectra of the laser displacement measurements, (Φ_{yy}) normalised with a nominal Φ_1 = 1 m^{2}s at $\alpha_g = 0°$ for variation in width.

be noted here that the flutter was not observed in this experiment showing that this process of jumping to flutter is sensitive, and a possible reason for this could be due to a different mounting mechanism of the aerofoil for this experiment.

Another observation can be seen in Fig. 4.21 between the different flaplets is that the Eigen frequency of the narrow flaplets does not increase as much as the baseline and the wide flaplets as the Reynolds number increases. This finding alludes to the fact that the wide and baseline flaplets are better at locking in to the large scale structures in the wake and reducing the vortex shedding, as was observed in Fig. 4.19.

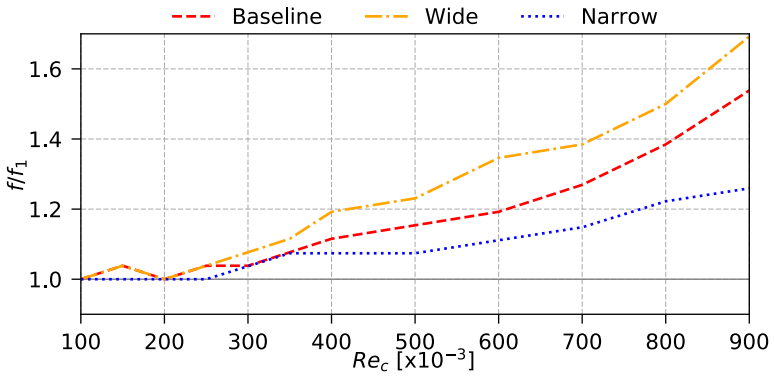


Figure 4.21: Normalised flapping frequency, with the respective Eigen frequency f_1, as Reynolds number increases at $\alpha_g = 0°$ for variation in width.

4.3.3.3 Variation in Flaplet Inter-Spacing

The variation of the inter-spacing of the flaplets is in effect a way to alter the 'porosity' of the flaplets. The changes in the spacing are detailed in Table 4.1, and it can be seen that the smallest spacing is that of the baseline flaplets (1 mm) followed by the medium spacing (3 mm) and large spacing (7 mm). The large spacing flaplets are spaced such that every other flaplet, from the baseline case, is removed. At $\alpha_g = 0°$, Fig. 4.22a, the flaplets generally behave in a similar manner to each other. However, it is clear that the smallest spacing (baseline) has the most reduction in the low frequency range, whereas the medium and the large spaced flaplets show only a small or no reduction in this range. As is seen with all other tested cases, the flaplets do lead to an increase of noise in the high frequency range, the largest spacing inducing the smallest increase.

Increasing the angle to $\alpha_g = 10°$ and $15°$ shows similar effects, and as in the previous geometric variations, the magnitude of the effects are enhanced.

The ΔL_p contours in Figure 4.23 again show that the reduction zone is dependent on the length only. The magnitude of the reduction zone shows that there is quite a large drop off in effectiveness when the inter-spacing is increased to the medium inter-spacing and again even further when the large spacing is used. The large drop off in effectiveness was also seen by Gruber, Azarpeyvand and Joseph (2010) once the spacing between the slitted serrations was increased.

The sound maps for the 1 kHz band shows very little difference between the different spacings. At 8 kHz, it can be seen that as the spacing increases from the smallest

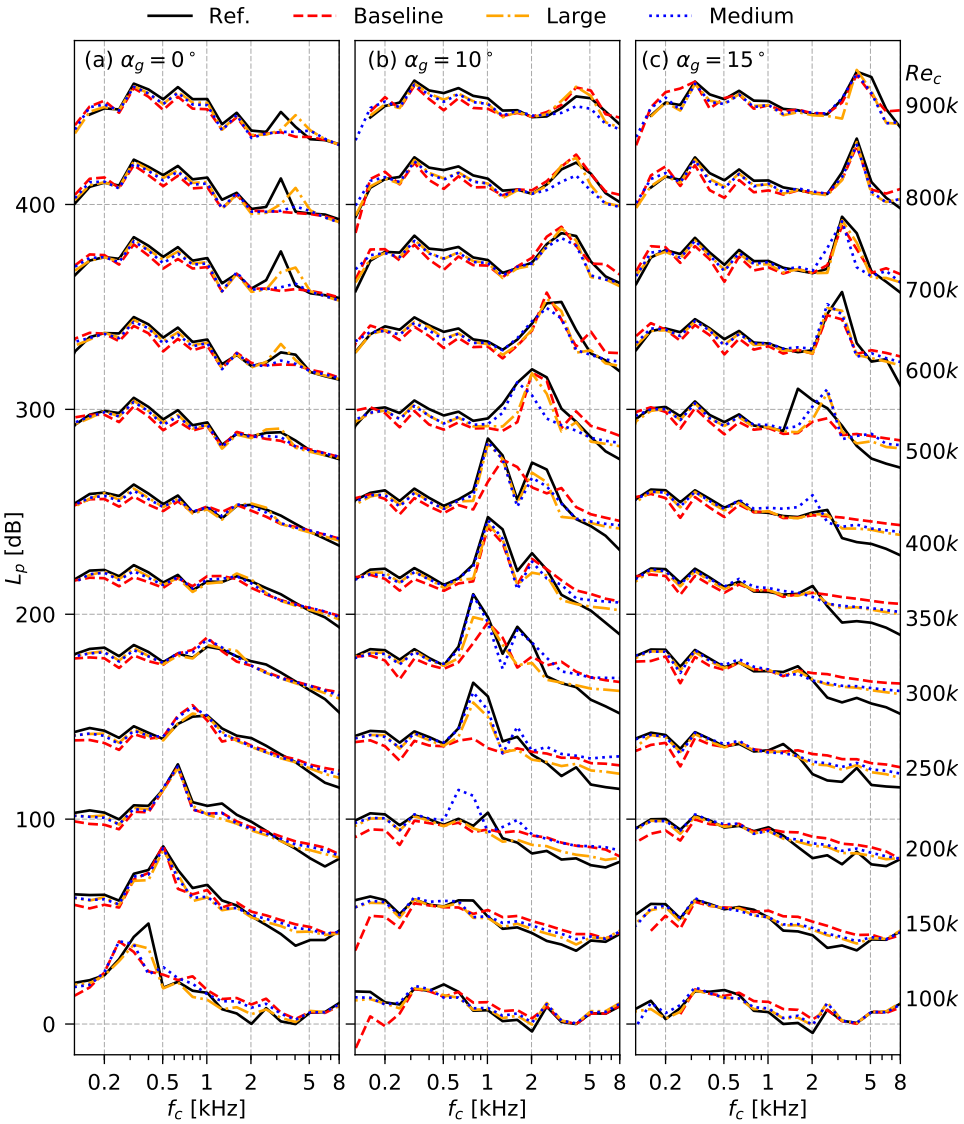


Figure 4.22: 1/3 Octave band acoustic spectra for variation in inter-spacing. Each of the spectra are spaced with 35 dB from each other for clarity.

(baseline case (f)) to the largest (g) the acoustic source located at the flaplets decreases in strength, again as with the other geometric variations this is due to the reduced flaplets surface area.

When looking at the OSPL and the ΔOSPL at $\alpha_g = 0°$, Fig. 4.25a-b, it is visible that at flow velocities for which tonal noise ceases to occur ($Re_c > 300,000$) there is a clear reduction of noise for all flaplets. Thereby, the magnitude of the reduction increases as the spacing is reduced. A 'steady' reduction of ≈ 3.5, 2.5 and 2 dB for each of the cases can be seen, in the order of inter-spacing distance. This shows that, although

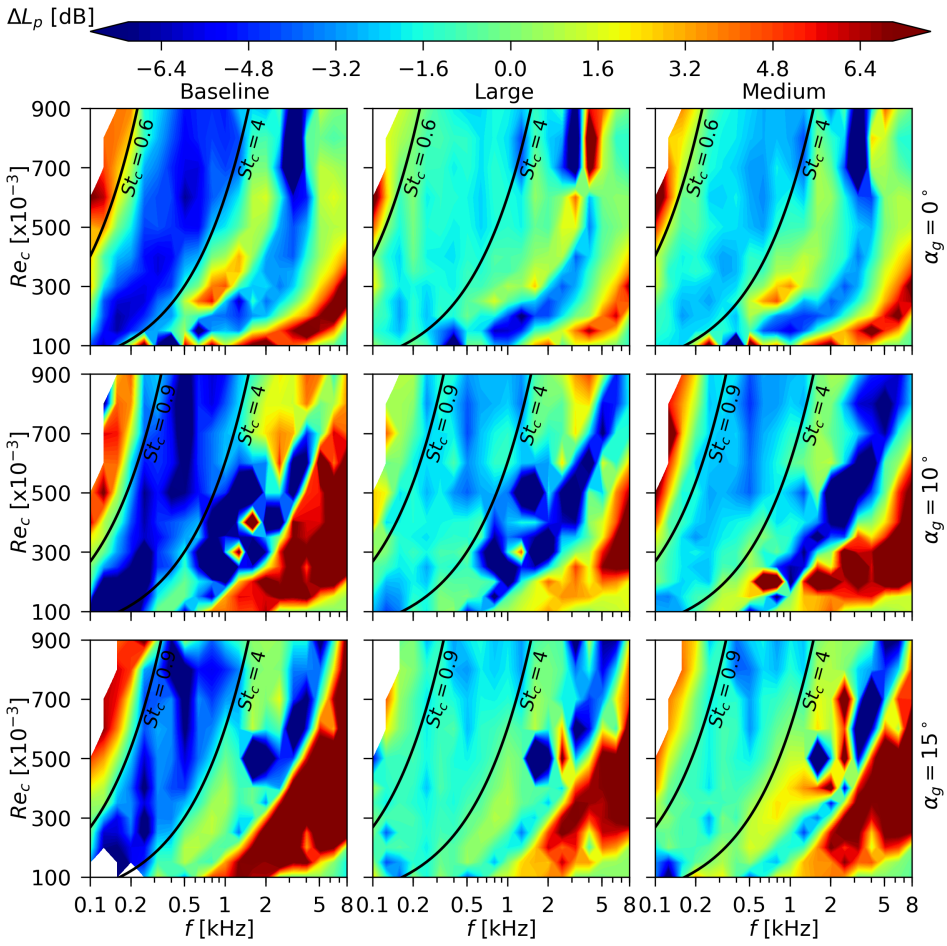


Figure 4.23: ΔL_p contours for variation in space, with the zone of maximum reduction indicated.

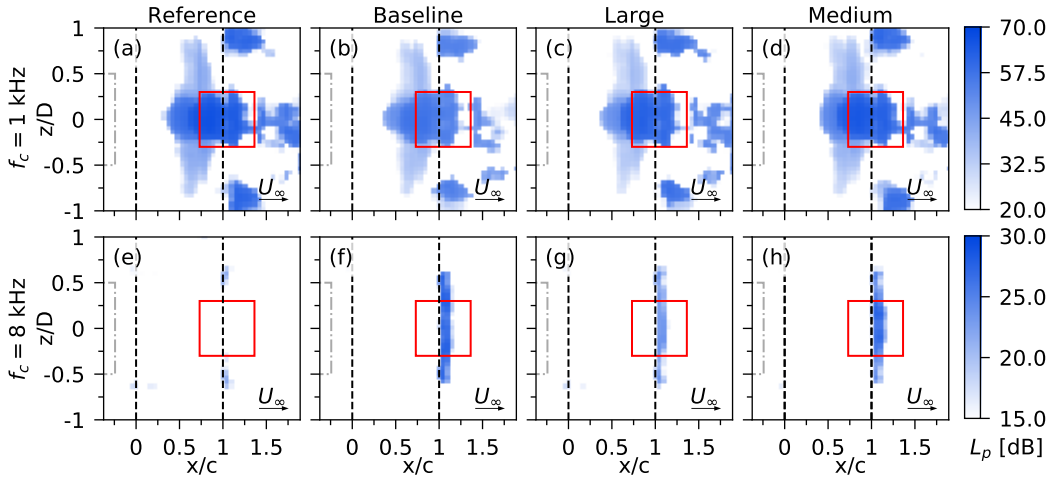


Figure 4.24: 2D sound maps as the inter-spacing is varied, at Re_c=350,000 and $\alpha_g = 10°$. (a–d) shows the frequency band, f_c=1 kHz and (e–h) shows the frequency band, f_c = 8 kHz. (- · - ·) indicates the jet nozzle, (- - -) indicates the aerofoil, (——) indicates the interrogation region for acoustic spectra.

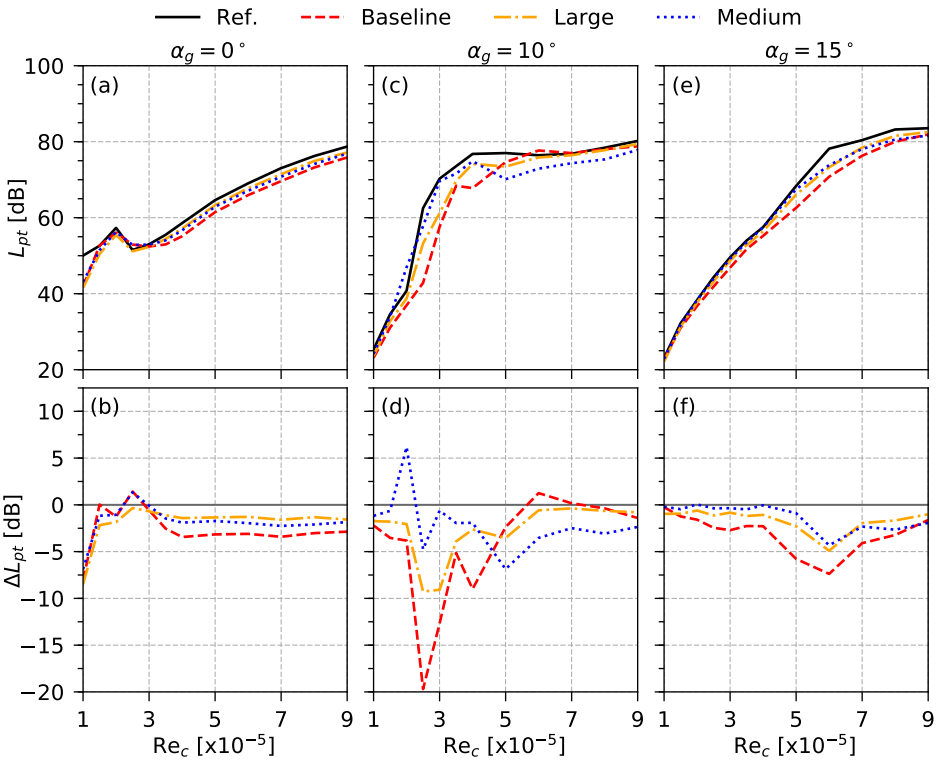


Figure 4.25: OSPL, denoted as L_{pt}, and Delta OSPL, ΔL_{pt}, for variation in flaplet inter-spacing.

the smallest spacing increases the high frequency noise the most, the low frequency noise reduction is sufficiently large enough to compensate and yield this moderate overall reduction. At $\alpha_g = 10°$, the tonal noise reduction is the dominant contribution to the overall noise reduction. Increasing the angle further shows an interesting result, where the medium spaced flaplets show no overall reduction until $Re_c = 500,000$ where the reduction is again due to the suppression of the tonal noise component. For this geometric constraint it can clearly be seen that, generally, the smallest spacing is the most efficient across all the tested cases.

Figure 4.26 shows the hot wire measurement results for this geometric variation. Again, as seen with the width variation, the difference in mean velocity observed is due to the elongation of the effective trailing edge. Looking at the RMS velocity profiles, again little difference is seen between inter-spacing at $\alpha_g = 0°$ and $10°$. However, further increasing the angle to $15°$ again shows a clear difference between the spacings, where the smallest spacing (baseline flaplets) leads to the smallest RMS values. As the spacing increases, the RMS velocity profile tends back towards that of the reference

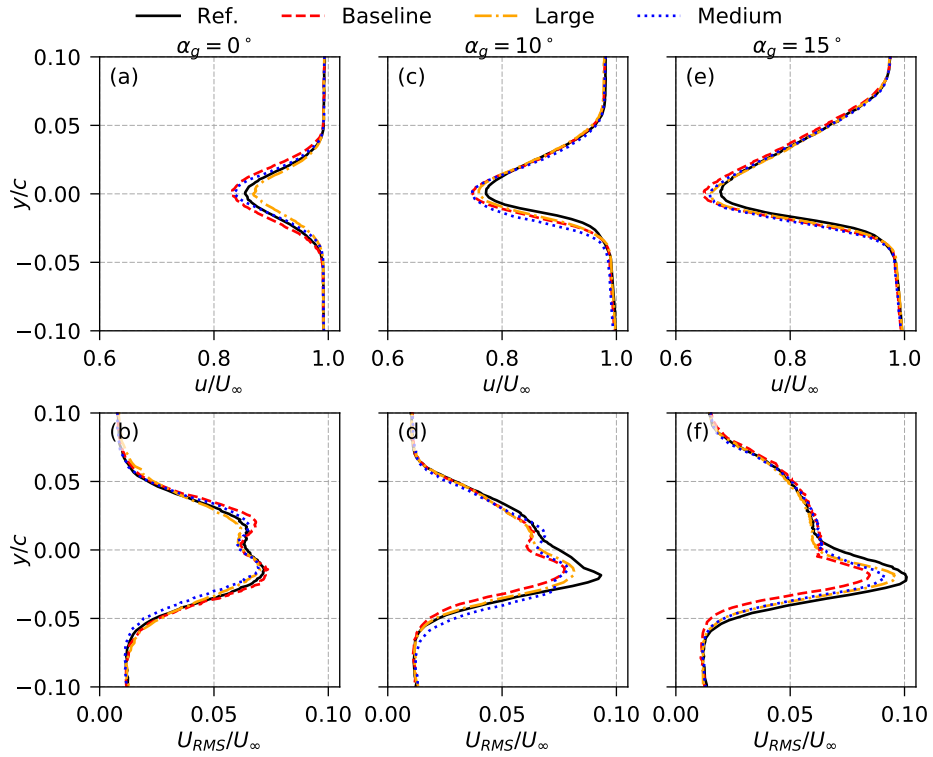


Figure 4.26: Mean and RMS wake profiles of the streamwise velocity component at $Re_c = 200,000$ for variation in inter-spacing.

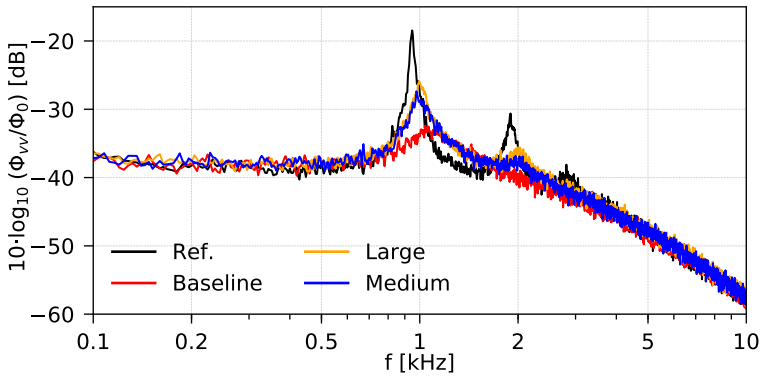


Figure 4.27: Fluctuating vertical velocity component, v', turbulence spectra (Φ_{vv}) normalised with a nominal $\Phi_0 = 1$ m^2/s, measured at the peak RMS point in wake profiles at $\alpha_g = 15^\circ$ and $Re_c = 200,000$ for variation in inter-spacing. Each spectrum is spaced by 10 dB for each other for clarity.

case, which is to be expected.

When looking at the turbulence spectra in the wake, shown in Fig. 4.27, it is immediately obvious that as the inter-spacing is increased, the spectral shape tends back towards that of the reference case without flaplets, as the vortex shedding peak

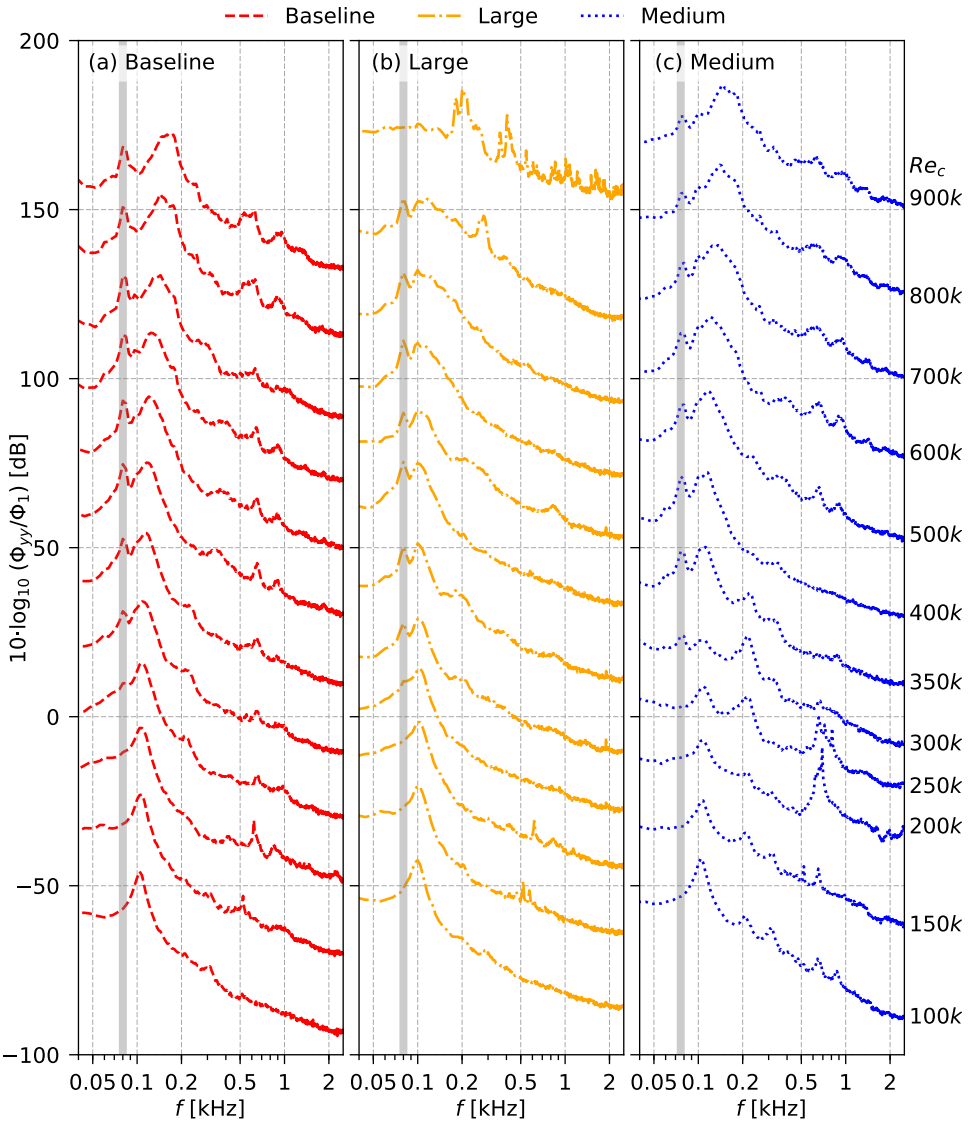


Figure 4.28: Spectra of the laser displacement measurements, (Φ_{yy}) normalised with a nominal Φ_1 = 1 m^{2}s at $\alpha_g = 0°$ for variation in inter-spacing.

increases. This is reflected in the resulting shedding energy calculation according to Eqn. (4.4), where the baseline flaplets yield a value of 0.158 m^{2}s^{-2}, the medium spacing 0.294 m^{2}s^{-2} and the large spacing 0.365 m^{2}s^{-2}. Therefore it can be further seen that the 'optimal' configuration of spacing is indeed the shortest spacing.

In the laser displacement spectra, again the Eigen frequency of the flaplets can be easily determined for each of the cases. An interesting result can be observed in Fig. 4.28b, where at $Re_c = 800,000$ a secondary peak at 280 Hz can be observed, and this does not corroborate with the first torsional or second bending mode, and is unclear what

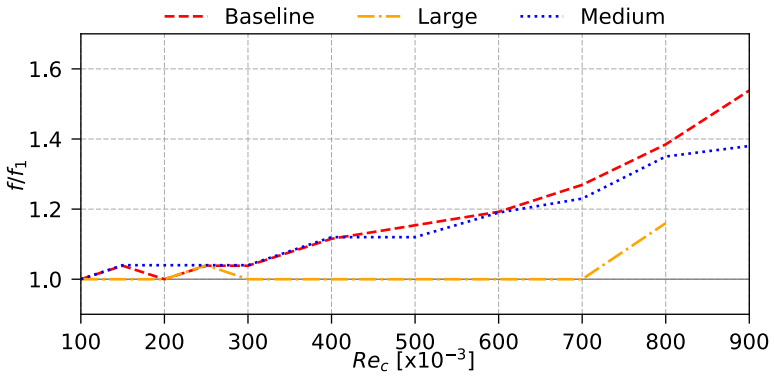


Figure 4.29: Normalised flapping frequency, with the respective Eigen frequency f_1, as Reynolds number increases at $\alpha_g = 0°$ for variation in inter-spacing.

this frequency represents. As the Reynolds number increases further to $Re_c = 900,000$ it was observed that the flaplets started to go into flutter. It should be noted here that the flutter at this testing condition was intermittent, and would periodically go in and out of flutter, therefore seems to be the limiting condition for this arrangement of flaplets. For the medium inter-spaced flaplets, Fig. 4.28c, at $Re_c = 200,000$ and $250,000$, the tonal noise frequency can be clearly seen to be attenuated in the vibration of the flaplets.

When looking at the frequency shift of the Eigen frequency peaks, Fig. 4.29, the shift of the flapping frequency of the medium spaced flaplets closely follows that of the baseline flaplets, until it starts to slightly drift at Reynolds numbers above 700,000. The large spaced flaplets oscillate at the Eigen frequency throughout the test range until $Re_c = 800,000$, where these is a sudden increase in the frequency, prior to flutter.

4.4 Conclusion

An extensive acoustic study has been carried out on the geometric optimisation of self-oscillating trailing edge flaplets to reduce aerofoil self-noise in a passive way. The effect of a variation of the free vibrating length, width and inter-spacing of these flaplets has been investigated against the reference case of a plain aerofoil. Basically, it has been shown that all flaplets oscillate and reduce the tonal noise to some extent. This has been attributed to the flaplets working as pacemakers, which keep the fundamental instabilities of the T-S waves in the boundary layer flow in their linear state via a lock-in mechanism (Talboys and Brücker, 2018). Measurements with a laser displacement

sensor showed the 1st flexural bending mode being dominant throughout the entire Reynolds number range. Furthermore, hot wire measurements of the flow in the wake demonstrated that the acoustic results are correlated to the peak levels of turbulence (RMS values of the velocity fluctuation) in the wake. Low turbulence levels mean less tonal noise and vice versa. In a recent study from Yu and Yang (2020) it was shown that an oscillating trailing edge fringe is able to reduce the strength and size of the shed vortices, similar as observed for an active oscillation of the trailing edge reported by Simiriotis et al. (2019). A similar wake-modification can be concluded from the hot wire measurements for the passive oscillators.

The most effective tonal noise reduction was seen with the narrow flaplets, where almost all tonal components were dampened out. Besides the narrow flaplets, the short flaplets were also extremely effective at $Re_c > 600,000$. The following list discusses the results for different parameter variations:

- Varying the free vibrating length: This has the most interesting effect, as it changes the natural frequency of the dominant flexural bending mode. When the long flaplets were tested (lower natural frequency), the noise level was reduced at a lower frequency range and vice versa for the short flaplets. Therefore, the range of frequencies where the most reduced noise level is achieved can be tuned by the length of the oscillators.

- Varying the width: Within the low frequency range the widest flaplets had the most effect while the narrow flaplets were least effective, albeit a slight reduction was still observed. It is hypothesized that this is due to the loss of spanwise coherence for the narrow flaplets, which are free to move independently from each other. When increasing the flow velocity (Reynolds number) the widest flaps show an increase in oscillation frequency. This let us conclude that the wider flaplets are locking in with the large scale structures in the wake, affecting the vortex shedding as was further alluded to with the hot wire measurements. In contrast, the motion of the smaller ones is rather prescribed by small-scale turbulent structures.

- Varying the inter-spacing: As has been seen already in previous studies by the authors (Talboys, Geyer and Brücker, 2019a; Talboys, Geyer and Brücker, 2019b), the flaplets with small inter-spacing show a clear low frequency noise reduction. In this case, the flaplets are effectively 'slit-trailing edge serrations'. A low frequency noise reduction was observed by Gruber, Azarpeyvand and Joseph (2010) with cardboard slit serrations, both experimentally and analytically. While the analytical approach was able to determine multiple frequencies that could be reduced, their experimental results revealed only a single zone where the reduction is observed, similar to the results herein. We would like to point out that it cannot be excluded from their experiments that small vibrations existed, especially as the herein observed acoustic effect is already visible for vibration amplitudes as small as 100-200 μm (compare also the study with active oscillating flaplets with a similar effect at similar oscillation amplitudes, see Simiriotis et al. (2019)). Furthermore, their noise reduction was focusing on the broadband noise while the flaplets herein clearly address the tonal noise components.

- Flaps going into flutter: An interesting feature was observed at high Reynolds numbers ($Re_c > 600,000$), where two of the geometries show a sudden massive increase in noise emission. This is attributed to the flaplets going past their critical velocity, at which the torsional bending mode or the second flexural bending mode is excited. Both frequencies could be identified in the spectra prior to the flaplets going into flutter. This causes flow separation and the flaps are no longer effective. Therefore, this constraint must be accounted for in future designs. This could be done either by modifying the flaplets geometry or via the use of non-isotropic materials to prevent the torsional mode.

Following this extensive study, it can be concluded that an optimal flaplet geometry might have a combination of both short and narrow flaplets to see if the benefits of both modifications will hold together and produce an even more effective flaplet configuration. A new practical integrated automated flaplet deployment system is currently in development at City, University of London such that the flaplet length, and

hence the Eigen frequency, can be tuned 'on-the-fly' depending on flight conditions. This new automated system is also being investigated with the integration of piezoelectric flaplets where the oscillation can be monitored in real time giving a 'live' view of the flaplets, with potential to view the spanwise interaction of the flaplets. The other benefit of this technology is the application for energy harvesting from the small scale fluctuations of the flaplets in the flow.

4.5 Critical analysis

4.5.1 Overview and study contributions

This study builds off the work in Chapter 3, where various different geometrical parameters of the flaplets were changed. Here the parameters that were changed are the spanwise width, the length (in the chordwise direction) and the inter-spacing between each flaplet. The aim was to see if there was an 'optimal' configuration of flaplet for different frequency bands. It was seen that a reduction in low frequency noise can be targeted by tuning the length of the flaplets. If one wanted to target a lower frequency band then a longer flaplets should be used and vice versa if a higher frequency band is targeted. In general, the smallest inter-spacing provided the best results for noise reduction.

4.5.2 Model Vibration

As was explained in the text in §4.3, the model was seen to vibrate in small amplitudes in the tunnel. In order to separate this effect from the flaplet vibrations we started to measure the plain airfoil with the laser displacement sensor. The sensor was positioned at a streamwise location $x = 0.9c$ such that we could observe the model vibrations near to the flaplet location. Looking at Fig. 4.30, the vibration of the model (reference aerofoil) is compared to the vibration of the flaplets at $\alpha_g = 0°$. It can be seen that indeed the model (Fig. 4.30a) is seen to vibrate at a distinct frequency, which is approximately $f \approx 80$ Hz. This frequency can be also seen in the baseline flaplet measurements (Fig. 4.30b) where it really starts to emerge at a $Re_c = 250{,}000$. When looking at how 'intense' the vibrations are, by looking at the RMS of the signal (Fig. 4.30c), it can be

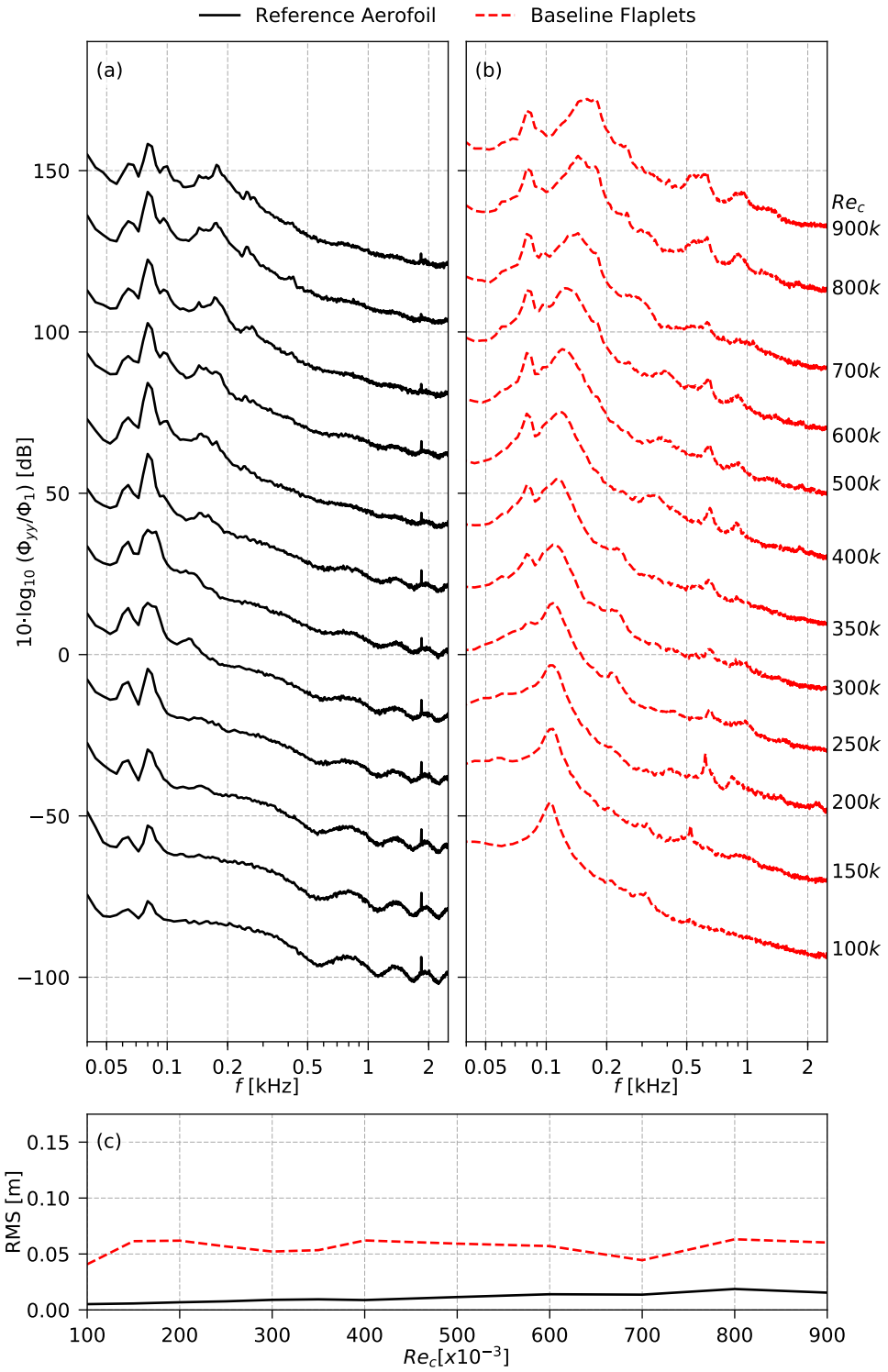


Figure 4.30: Comparison of the reference aerofoil vibration (a), the flaplets vibration (b) and the RMS of the vibrations (c) at $\alpha_g = 0°$.

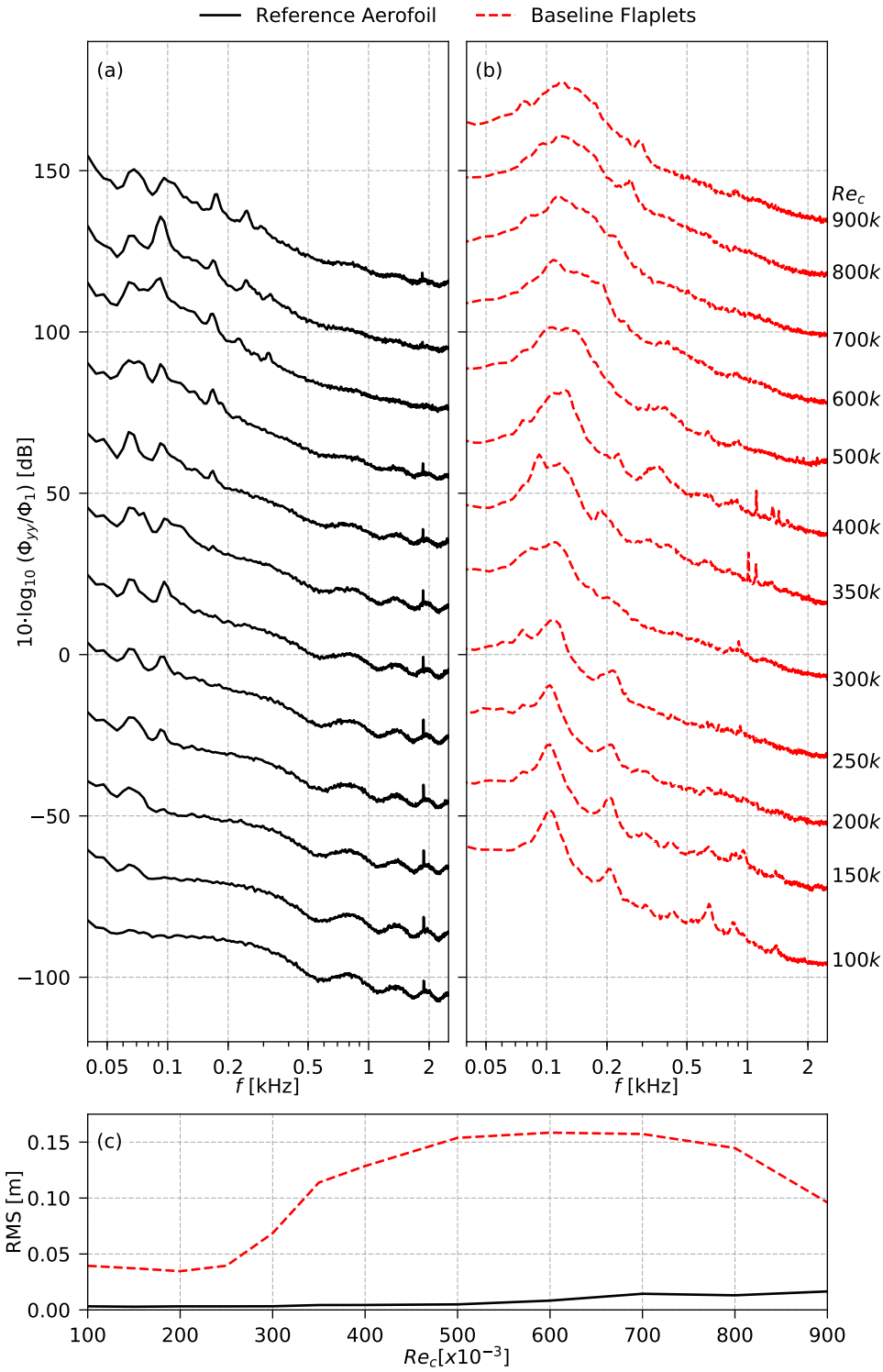


Figure 4.31: Comparison of the reference aerofoil vibration (a), the flaplets vibration (b) and the RMS of the vibrations (c) at $\alpha_g = 10°$.

seen that the RMS of the aerofoil vibration is low and increases slightly as the Reynolds number increases. In comparison, the magnitude of the RMS fluctuations of the flaplets is generally higher and rather constant across all Reynolds numbers.

When looking to increased $\alpha_g = 10^\circ$ (Fig. 4.31), there seems to be model vibration at $f \approx 70$ Hz and at $f \approx 100$ Hz. These peaks only started to become apparent at $Re_c = 200,000$ and persist also for the higher Re_c values. The flaplets were still seen to oscillate at their Eigen frequency across the entire range, however the location of the peak shifted towards higher frequency and became broader. Overall, the flaplets oscillations near their Eigen frequency are still the dominant peak in the spectrum.

In Fig. 4.31c, an interesting feature can be observed. Beyond a Reynolds number of $Re_c = 250,000$ the RMS of model vibrations suddenly rises and plateau's at $Re_c = 500,000$, raised by over three times the original value. The RMS level stays at this level until $Re_c = 700,000$ at which point, it interestingly, decreases again. The reason as to why this level decreases is unknown, and further investigation with piezoelectric flaplets should be carried out.

4.5.3 Beamforming Considerations

When carrying out the beamforming for this study, there are many considerations that need to be accounted for, some of which will be detailed here.

4.5.3.1 Beamforming models

In order to get the far field noise contributions, many beamforming models can be used. What follows here is an analysis of some of the most commonly used models and the reasoning as to why the DAMAS algorithm was selected for this study will be presented. Only a selection of beamforming models are chosen here, and a more extensive list of models and their applications can be found in the review by Merino-Martínez et al. (2019).

The most important aspect of the measurements is the acoustic spectra, hence this should be first investigated. Figure 4.32 shows the acoustic spectra of the reference aerofoil at a Reynolds number, $Re_c = 350,000$, and at a geometric angle of attack, $\alpha_g = 10^\circ$; where different beamforming algorithms have been used to see their suitability for this

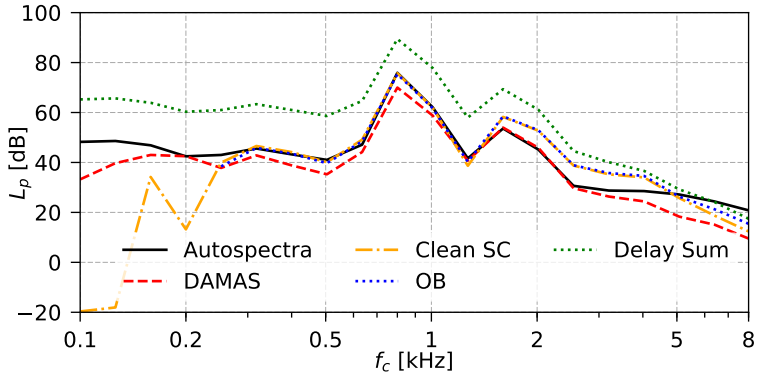


Figure 4.32: Comparison of different beamforming models for the reference aerofoil at $Re_c = 300,000$ and at $\alpha_g = 10°$.

study. It should be noted here that the 'Autospectra' is simply a weighted sum of the signals of each of the microphones and as such should act as a theoretical maximum. A brief overview of the algorithms used in Fig. 4.32 and 4.33, will be given below:

- Delay & Sum (Conventional beamforming): This is a very quick and efficient method that uses a steering vector which 'directs' the microphone array to an acoustic source. The steering vector is calculated from phase delaying each microphone in the array depending on the acoustic source location. The delay is added to the signal for each microphone, as such the microphones are now all in phase. The microphones can then be directed to each point in the interrogation grid and the signals from the microphones can be tested for noise source coherence.

- DAMAS (Brooks and Humphreys, 2006): DAMAS is a deconvolution algorithm, where the conventional beamforming result is 'post-processed' by removing the effects of the microphone array. DAMAS uses a synthetic point spread function (PSF) to remove the effects of the array. A PSF is effectively a map that shows the spatial response of the microphone array to a single point source at any point in the measurement zone. The resulting PSF will show the noise source as a clear point on the map, known as the main lobe, and it is then accompanied by some side lobes that encapsulate the main lobe at a reduced level. There are some downsides of using this type of map. One is that the width of the main lobe could be such that it overlaps two noise sources and therefore it will be interpreted

that only one source is present. The other is that weaker noise sources may be close to a larger noise source and as such will be masked; therefore may not be interpreted correctly or at all. So in order to obtain the a good PSF, the design of the microphone array needs to be carefully considered.

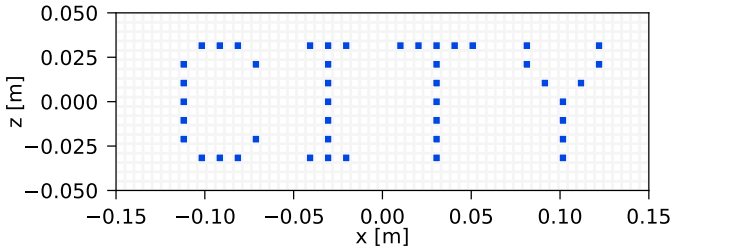
As mentioned, the way DAMAS works is to produce a synthetic PSF, but first the area that wants investigating should be split into a discrete grid. A PSF will then need to be created and assigned to each of the points on the grid, such that the response of the microphone array to a point source at any particular location can be determined. A system of equations, amounting to the amount of points that there are on the grid, is then formed and solved iteratively using a Gauss-Seidel method. Therefore the finer the grid resolution, the more computational resource is needed. This also is the case with the number of iterations needed to obtain a converged solution. The sensitivity of the results to the grid size and number of iterations will be discussed in §4.5.3.2.

- CleanSC (Sijtsma, 2007): This algorithm is also a deconvolution algorithm. However, this algorithm does not need a theoretical PSF so is computationally less intensive. CleanSC is an alternate of the original Clean algorithm that has been commonly used for Astrology. Clean is an algorithm that 'cleans' sound maps from conventional beamforming, which are dubbed as "dirty" sound maps, by iteratively removing PSF of peak noise sources from the sound maps. Once removed the PSF is replaced by a beam without side lobes, called a 'clean' beam. Whereas the CleanSC is based upon spatial source coherence. In this algorithm, source peaks are determined from the dirty map and then these coherent sources are subtracted from the map and replaced with a clean beam at the same location. This process of removing and replacing is carried out in an iterative manner until the convergence criteria is met. An issue with this algorithm is that if there are two sources close together, it will not be able to distinguish between them so will show up as one noise source with the sound level being the combined sum of the two sources.

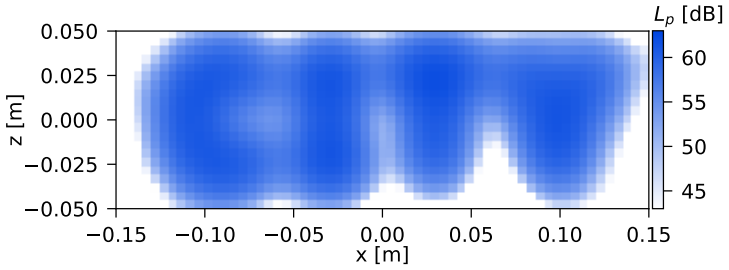
- Orthogonal Beamforming (OB) (Sarradj, 2010): OB is based off eigenvalue decomposition of the cross spectral matrix. Here the idea is that each of the eigenvalues is related a noise sources and the largest eigenvalues are related to the largest noise sources. Once the eigenvalues are determined, the sources are then mapped to the sound map. Where the largest eigenvalue is then assigned to the largest peak, second largest to the second largest peak and so on.

Now to look at how the algorithms compare with each other at measuring the acoustic spectra, Fig. 4.32. It can be immediately seen that the Delay and Sum (conventional beamforming) over-predicts the noise level by over 20 dB in the low frequency range and then at the higher frequencies, it over-predicts less and even slightly under-predicts at frequencies over 6 kHz. The CleanSC and OB algorithms at frequencies over 300 Hz, match the Autospectra very well with some slight over predictions at the second dominant peak. However it can be seen that they both perform poorly at $f_c < 300$ Hz. Both models seemed to struggle to identify low frequency sources and as such the noise level cannot be predicted well. Saying that, the CleanSC model did find some sources but when the signals were banded into the third octaves the level is negatively impacted by the other sources it could not find within the band. This is a known issue at low frequencies for the CleanSC model. When looking at the DAMAS model, it can be seen that across the entire range the spectra is well captured. There are some deviations at both the high and low frequencies. As such that data below $f_c < 200$ Hz should not be used as part of the analysis.

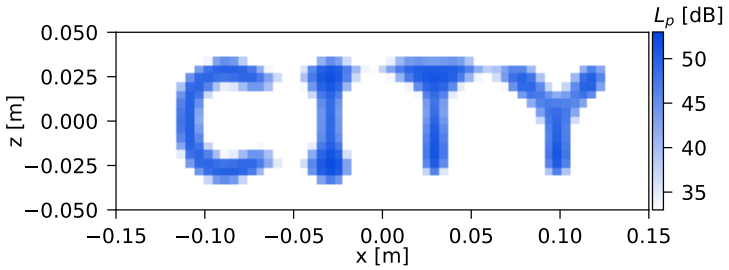
To check how each model responds to a known set of sound sources, a grid with some predetermined sources was set-up and a sound map for each of the models was calculated. The sources were set up in a pattern depicting the letters “CITY”, and the location of these sources can be seen in Fig. 4.33a. The first model that was the delay and sum, Fig. 4.33b, it can be seen that the this gives the general outline and location of the noise sources but is generally ‘blurred’. When using the DAMAS, remembering that it is a deconvolution algorithm that uses the conventional beamforming as a base, the source locations are now significantly clearer. Saying this there is still some blurring around the sources, and this is due to the synthetic PSF that is generated and used in this



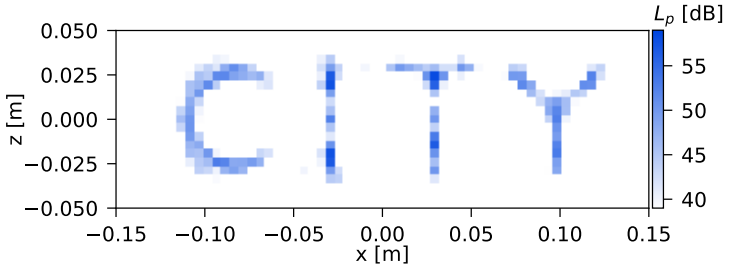
(a) Source locations



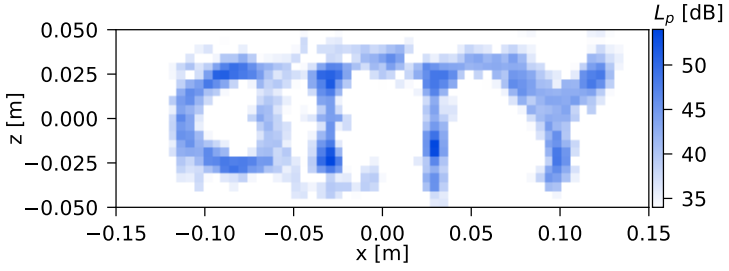
(b) Delay & Sum



(c) DAMAS, 400 iterations



(d) CleanSC



(e) Orthogonal beamforming, 54 Eigen modes

Figure 4.33: Comparison of sound maps produced by different beamforming algorithms at the third octave band, f_c = 8 kHz.

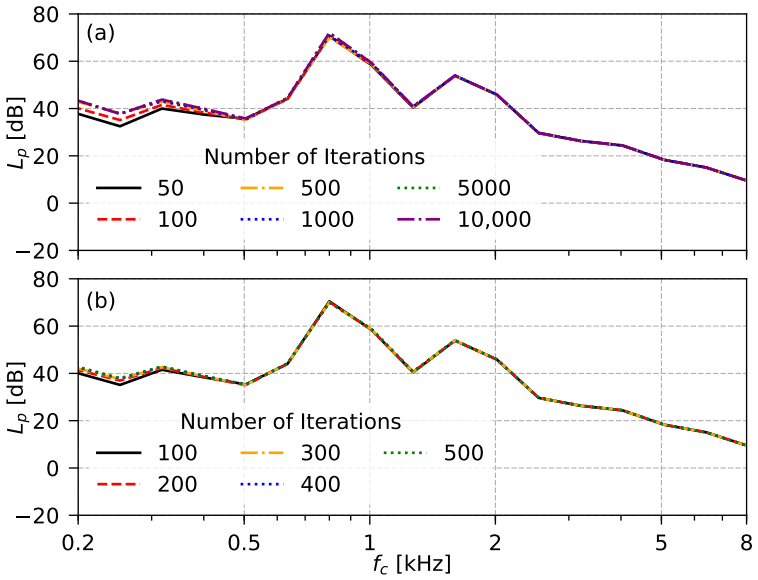


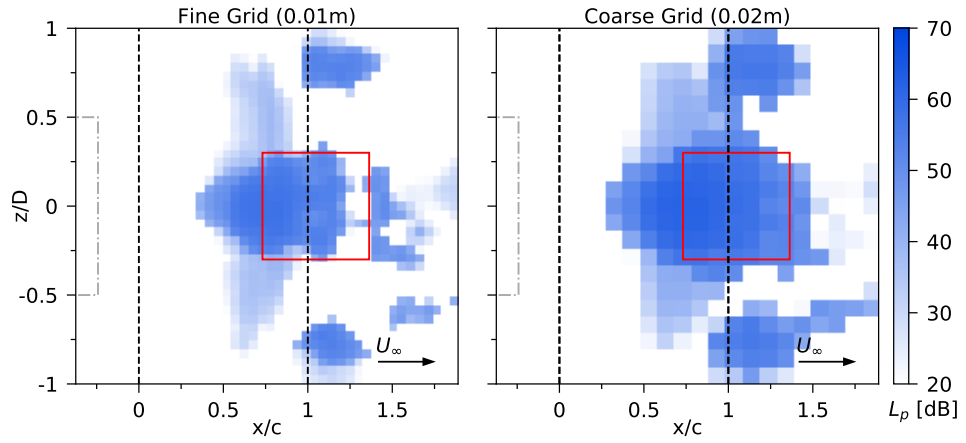
Figure 4.34: Comparison of the amount of iterations used for the DAMAS beamforming model for the reference aerofoil at $Re_c = 300,000$ and at $\alpha_g = 10°$.

model. The CleanSC model, Fig. 4.33d, arguable gives the clearest sound map, where most of the detailing of the letters are captured. Finally the OB algorithm, Fig. 4.33e, shows an improvement on the delay and sum sound map. But in general, there is a lot of additional sources that have not been cleaned up using this method.

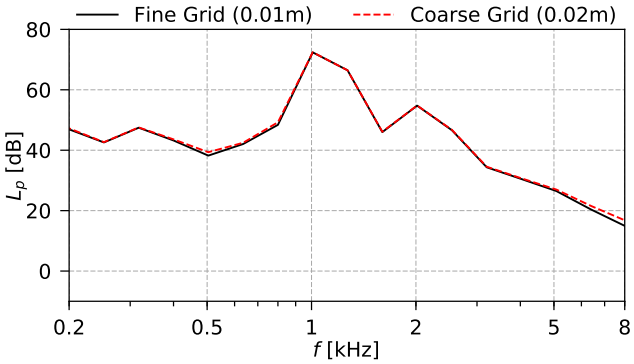
Taking everything into account, the decision was to use either the CleanSC or DAMAS algorithm for this study. Although the DAMAS solving is computational more expensive and the CleanSC soundmap is good, it was decided that the low frequency noise sources that can be obtained with DAMAS are superior to that of the CleanSC algorithm. Saying that, the DAMAS soundmap does still gives good clarity of the acoustic sources.

4.5.3.2 DAMAS considerations

Once the DAMAS model was selected, there were two major considerations that still need to be addressed. The first is the amount of iterations required for the solution to converge. Figure 4.34a, shows the acoustic spectra where a wide range of iterations have been used. It is interesting to see that beyond $f_c = 500$ Hz, no matter if 50 iterations or 10,000 iterations are used, the resulting spectra is approximately the same. The issues start to arise in the low frequency region, which is an important area for this study



(a) 2D sound maps at the frequency band, f_c = 1 kHz. (- · - ·) indicates the jet nozzle, (- - -) indicates the aerofoil, (——) indicates the interrogation region for acoustic spectra.



(b) 1/3 octave band acoustic spectra.

Figure 4.35: Comparison of fine (0.01 m) and a coarse (0.02 m) beamforming grid spacing

due to the observed reduction in Chapter 3. It can be seen that when 50 iterations are used, the level is noticeably lower than when more iterations are used. This is due to the lack of low frequency sources being detected with in these frequency bands. The same rationale applies to 100 iterations, albeit the level is closer. Once there is 500 or more iterations, there seems very little difference. So it is clear that there is a number between 100 and 500 iterations which is 'optimal' for computational time. Looking at Fig. 4.34b, this shows the iteration amounts in finer increment detail. As to be expected, as the iteration amount is increased the spectra the low frequency (f_c < 500 Hz) differences converge. Where it can be seen that at an iteration amount of 400, there is no longer any difference by increasing the iteration amount. Hence, this was the selected iteration amount for the study.

The second major consideration is the grid that is used to scan for acoustic sources

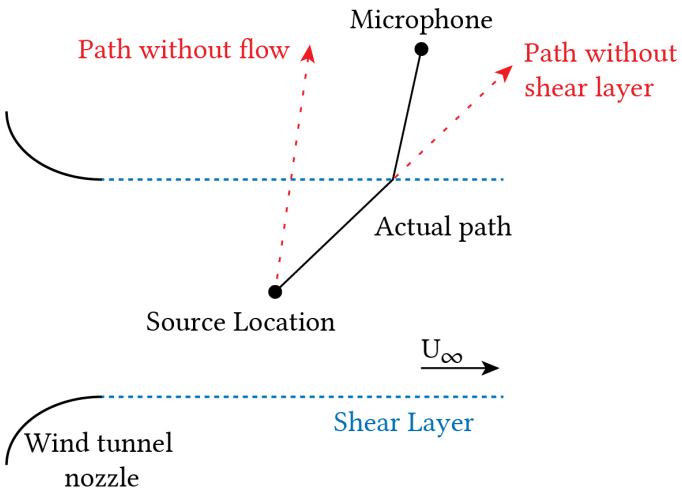
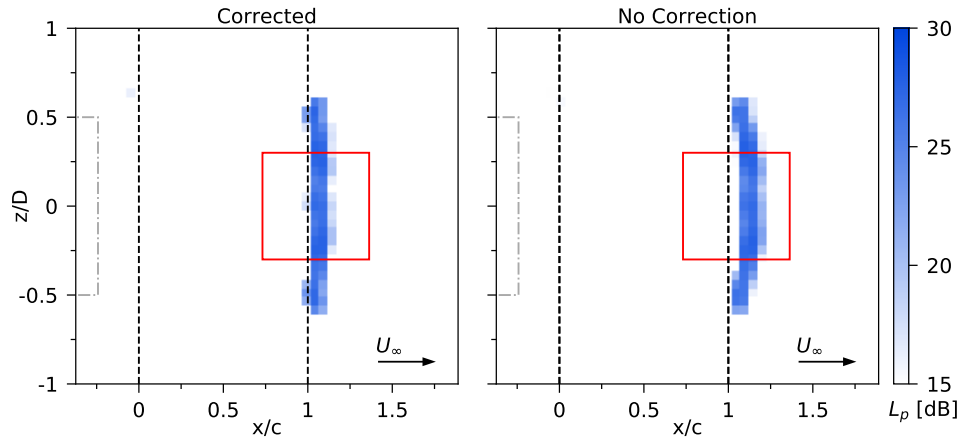
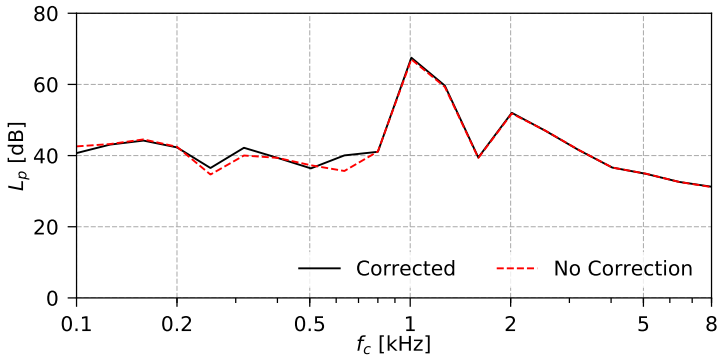


Figure 4.36: Diagram showing the effect of how the shear layer refracts the acoustic ray from a noise source in the core jet. This figure is adapted from Fig. 1.22 in Allen et al. (2002).

and the grid spacing. As if the spacing is double then the scan area is quadrupled, it would be a lot more computationally intensive. Saying this, benefits of having a finer grid might be important when presenting the 2D soundmaps as the higher resolution could give a better, more accurate, indication of the exact location of the acoustic sources. To this end, Figure 4.35 shows the effect of the grid spacing on both a 2D sound map and the acoustic spectra. Figure 4.35a is a comparison of the sound map with a fine grid spacing (left, 0.01 m) and a coarse grid (right, 0.02 m). Here it can be seen straight away the benefit of using a finer grid. There is much more resolution for the finer grid, where more details on the acoustic source location and level are given. When looking at whether the grid resolution is a contributing factor for the overall acoustic spectra, an integration of the highlighted sector in Fig. 4.35a needs to be carried out at each third octave band. Figure 4.35b shows the results of this integration, and interestingly there is very little effect from the grid resolution. In terms of computational time, the fine grid acoustic spectra took ~144 minutes whereas the coarse spectra took ~15 minutes. Therefore it was clear that for the study in Chapter 4 where 288 acoustic spectra were needed to be produced, a coarse grid was used to produce the acoustic spectra and the finer mesh was used just for specific third octave bands used for the sound maps.



(a) 2D sound maps at the frequency band, f_c = 8 kHz. (- - -) indicates the jet nozzle, (**- - -**) indicates the aerofoil, (——) indicates the interrogation region for acoustic spectra.



(b) Acoustic spectra for the whole interrogated frequency range.

Figure 4.37: Comparison of the baseline flaplets at Re_c=350,000 and α_g = 10°, with and without the shear layer corrections applied.

4.5.3.3 Open jet corrections

Another consideration that needs to be accounted for, regardless of the beamforming algorithm, is the effect that the open jet has on the acoustic path, between the noise source and the microphone. As the noise sources are situated within the core jet flow, they are prone to two effects that can cause errors in locating the noise source. A diagrammatic representation of this can be seen in Fig. 4.36. One is purely down to the fluid flow, where the sound is convected by the flow. This can be seen in Fig. 4.36, where the source is located in the centre of the core jet and the path of sound is tilted downstream due to the convection of the flow. The other is where the sound is refracted due to the shear layer, between the still air surrounding the core jet and the core jet itself. This effect can also be seen in the figure.

The method used herein to counter these effects is a ray casting method proposed by Sarradj (2017). This method is included within the open source beamforming package, Acoular, which was used for all the beamforming within this study. Figure 4.37a shows the results of the correction on the 2D soundmap. The case used here is the case used in the publication, with the baseline flaplets attached on the aerofoil at $Re_c = 350,000$ and $\alpha_g = 10°$. Immediately it can be seen that without the corrections, the trailing edge noise looks bowed. This bowing is due to the effects detailed above and it can be clearly seen that once the corrections are applied, the noise source becomes parallel to the trailing edge across the wetted span. When looking at the acoustic spectra, which is the integration of all noise sources within the highlighted red zone in Fig. 4.37a, it can be seen that there is actually very little difference between the correction and without the correction. This is due to the level not being effected by the shear-layer just the directionality of the acoustic rays.

4.5.4 Carbon fibre flaplets

To test the effect of the flaplets mobility and their oscillations amplitude on the sound emission spectra, a pair of flaplets were water-jet cut from carbon fibre sheets. The geometry of the flaplets was the baseline flaplet geometry (i.e. 5 mm width, 20 mm length and 1 mm inter-spacing). Two different thicknesses of carbon fibre were used, one had a comparable thickness to the original polyester flaplets, where h = 0.3 mm. The other set of carbon fibre flaplets were thicker at h = 0.5 mm. Therefore three different Eigen frequencies of flaplets, all of the same geometry could be tested and compared.

It must be noted here that, as the aerofoil was 3D printed, it had slightly warped over the time (over 1 year) between the results presented in the publication and the tests carried out with the carbon fibre flaplets. Hence, the results here cannot be directly compared to the results in the publication but can be compared with each other. The aerofoil here is also tripped, i.e. the boundary layer is turbulent and therefore there will be no tonal noise.

The first thing that should be checked is what vibrations are present with the new carbon fibre flaplets and measure their Eigen frequencies. For this study the Eigen

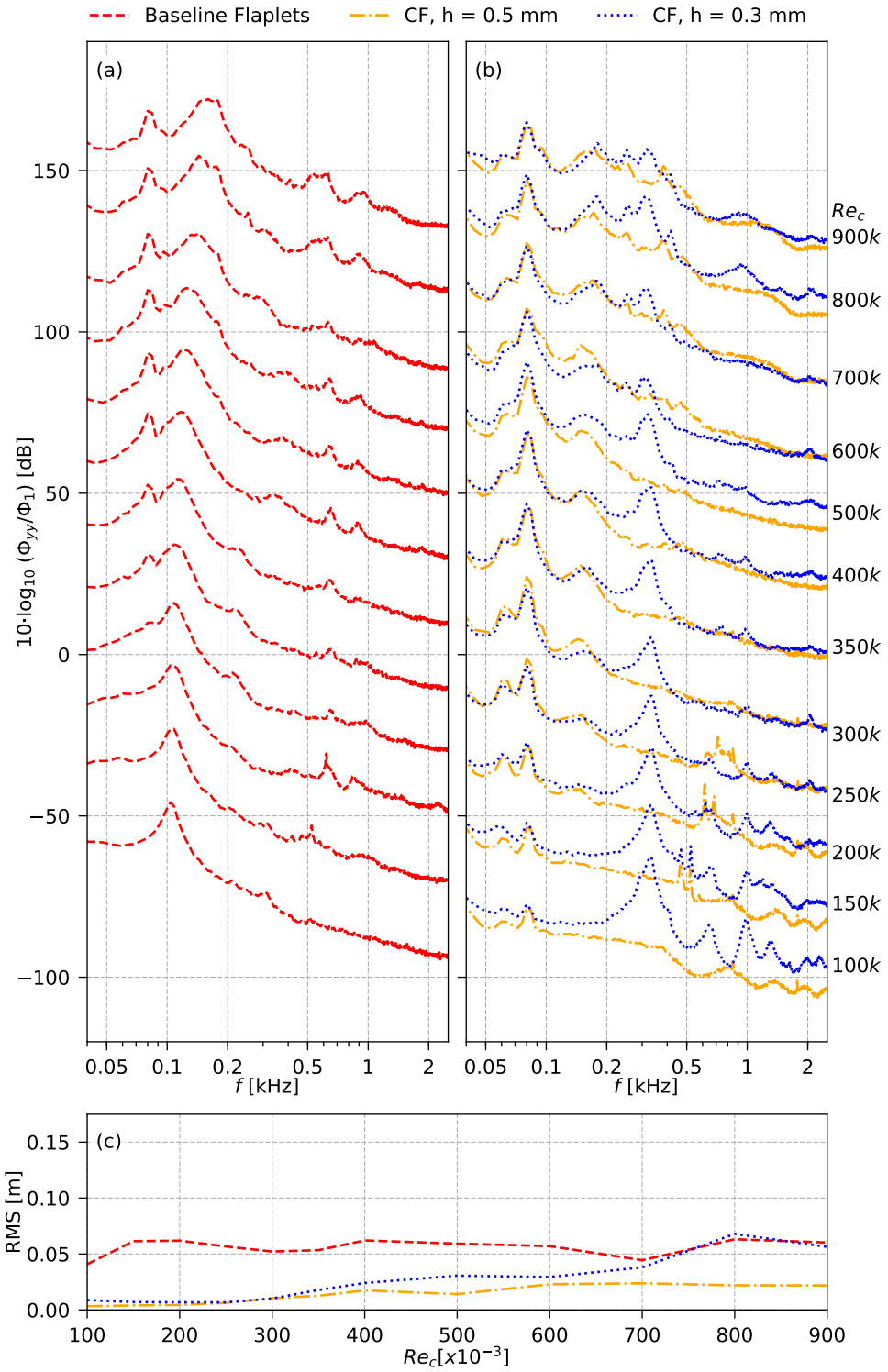


Figure 4.38: Comparison of the baseline flaplets vibration (a), the carbon fibre flaplets vibration (b) and the RMS of the vibrations (c) at $\alpha_g = 0°$.

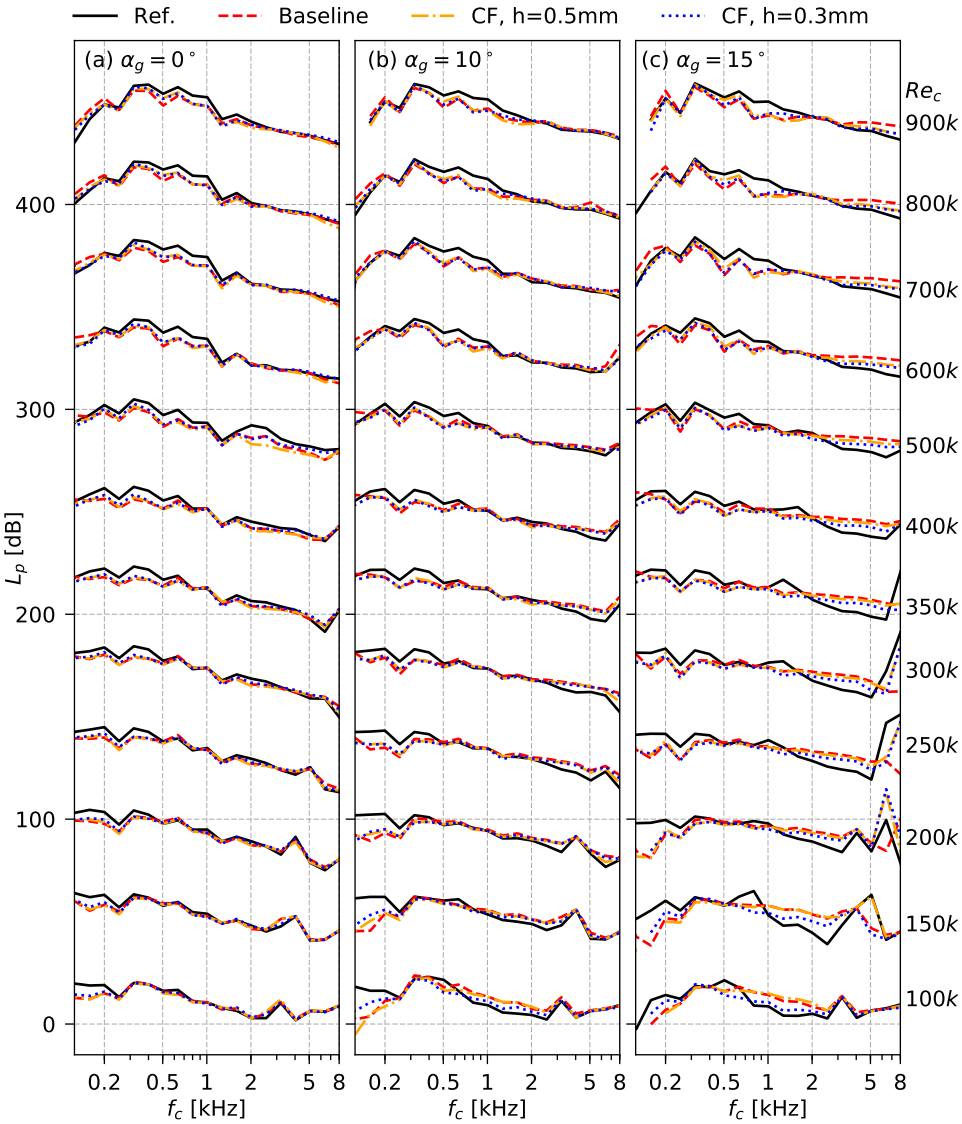


Figure 4.39: 1/3 Octave band acoustic spectra for flaplets of different thickness and material. Each of the spectra are spaced with 35 dB from each other for clarity.

frequency was measured in the same way as described in 4.3.1, and it was found that the Eigen frequency for the thin carbon flaplets was $f_1 = 330\ Hz$ and was $f_1 = 780\ Hz$ for the thick carbon flaplets. When looking at Figure 4.38a the spectra of the vibrations for the baseline flaplets can be seen, this is the same spectra as can be seen in §4.3. Figure 4.38b shows the response of the carbon flaplets, and the thin carbon flaplets (CF, h=0.3 mm) can be seen to be oscillating at the Eigen frequency. Whereas with the thicker set (CF, h=0.5 mm) the oscillation cannot be detected. For both cases, the aerofoil vibration can be detected as described in §4.5.2. When looking at the RMS of

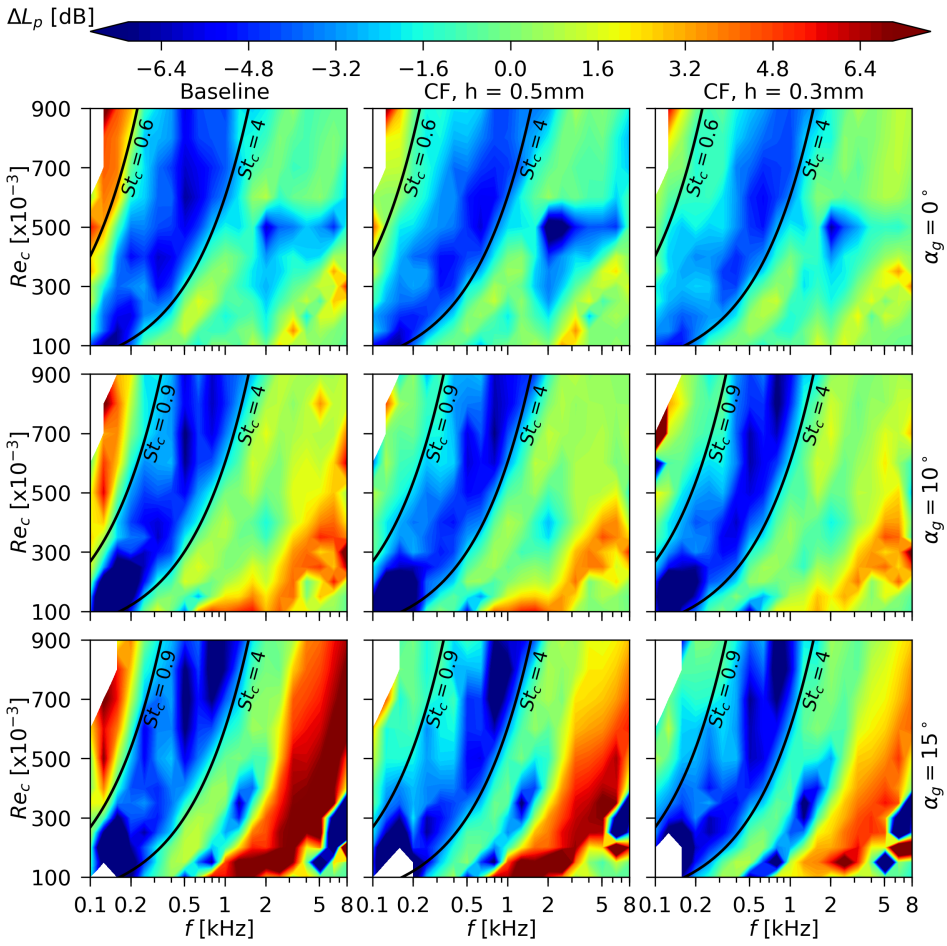


Figure 4.40: ΔL_p contours for flaplets of different thickness and material, with the zone of maximum reduction indicated.

the vibrations (Fig. 4.38c) it can be seen that at the lowest Reynolds numbers there is very small amount of vibrations from the carbon fibre flaplets, but as the Reynolds number increases the thin carbon flaplets tend to the RMS level of the polyester (baseline flaplets). Whereas the thicker carbon flaplets increase a little but still stays at a low level, similar to the level observed in Fig 4.30c for the baseline aerofoil. Showing that at they are more or less not oscillating within the tested range.

When looking at the acoustic spectra, Fig. 4.39, it can be first observed that the boundary layer was indeed sufficiently tripped to stop tonal noise from occurring. As was seen in the previous study, it can be seen that at all α_g and Reynolds number there is a reduction in noise in the low frequency range. What is interesting is that all of the flaplets, whether carbon fibre or polyester have the same range of reduction and

approximately the same magnitude in the reduction. This shows that it may not be necessary that the flaplets are oscillating to cause this acoustic reduction, rather it is the geometrical modification of the trailing edge that is causing this. Looking at the noise reduction contours, Fig. 4.40 which uses the single microphone recording rather than the beamformed results, there are clear regions of Strouhal number reduction. At $\alpha_g = 0°$, the Strouhal band of reduction is from $St_c = 0.6 - 4$. This can be seen for all of the flaplets tested here. In a similar way the bands are the same as each other as the angles is increased, where the only change is the lower limit is now $St_c = 0.9$. However, there does seem to be a slight difference. This is that for the flexible flaplets, at $St_c < 0.6$, there seems to be an increase in the noise level whereas with the rigid and semi-rigid flaplets there is either less of an increase or no increase at all. This is clearer at $\alpha_g = 10°$ and $15°$.

4.5.5 Flaplet porosity as a metric

Figure 4.41 shows the L_{pt} or OSPL against the flaplet 'porosity', where the porosity is defined as the ratio between flaplet surface area and the area of the gap between neighbouring flaplets. It should be noted here that the trailing edge porosity of the solid reference aerofoil case has been given a porosity of 0. A $Re_c = 500,000$ was chosen for this analysis as there was no tonal noise seen at $\alpha_g = 0°$ and was midway through the tested range. The general trend that can be seen in Fig. 4.41 is that when the flaplet 'porosity' increases, the OSPL decreases. Therefore the larger the flaplet surface area and the smaller the gaps in between each flaplet the better. However, this is a very tenuous trend, as the original flaplets show the lowest overall sound pressure level which does not fit this general trend. At other angles of attack for this Reynolds number, no trend could be seen. This was due to the presence of tonal noise at higher angles of attack, which dominate the OSPL plots. There could be merit in exploring this trend further but this should be done with a tripped aerofoil i.e. when no tonal noise is present over a wide range of test cases.

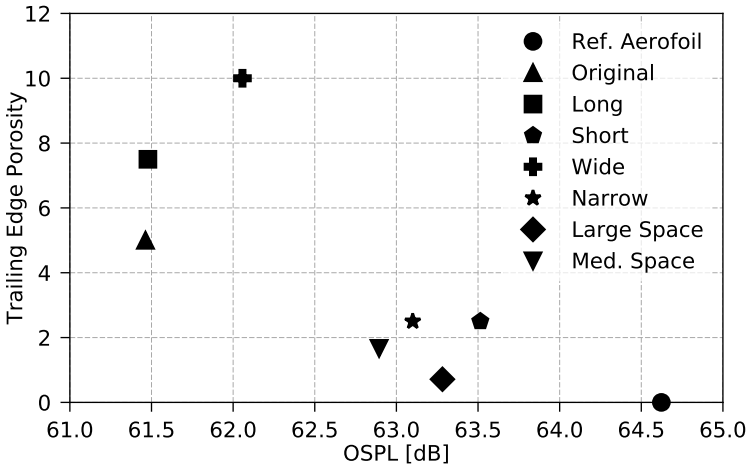


Figure 4.41: Flaplet porosity against Overall Sound Pressure Level at $Re_c = 500,000$ and at $\alpha_g = 0^\circ$.

4.5.6 Targeting certain Strouhal number noise reduction

One of the main conclusions of the work is the ability to target different Strouhal numbers and reduce the acoustic level in these Strouhal number regions by changing the flaplet length. Therefore, when looking at the average Strouhal number reduction (St_c^*), which is simply the average Strouhal number between the described limits in Fig. 4.7, and plotting these against the flaplet length, non-dimensionalised with the aerofoil chord, a linear trend can be seen. This linear trend goes with the proposed theory from Woodhead et al. (2019), where they said that the flaplets, or what they call slitted serrations, cause an acoustic destructive interference which is based upon the length of the flaplets. Where longer slitted serrations cause a destructive interference at lower frequencies and shorter serrations cause a destructive interference at higher frequencies. Figure 4.42, shows this trend clearly. However, it should be noted that more measurements with different length should be used to fully define the trend to see if it is linear as suggested here or more polynomial in nature.

4.5.7 Other considerations

4.5.7.1 How representative are the flaplets to the feather?

The flaplets are a very abstract simulation of the birds feathers and are more bio-inspired rather than bio-mimicked. The flaplets for this study are similar to those used in previous

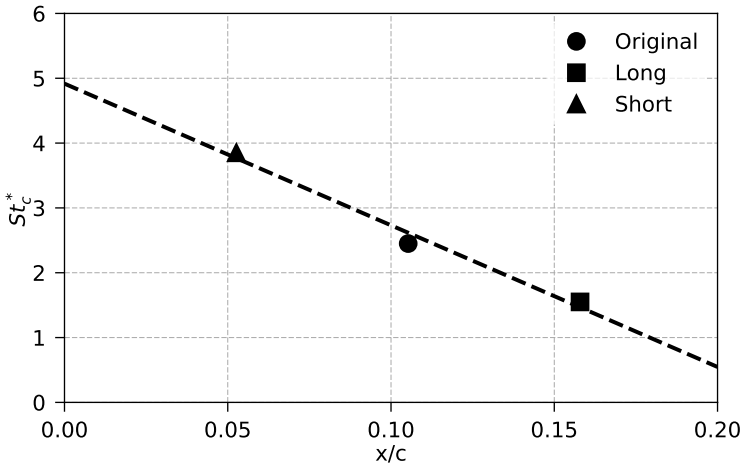


Figure 4.42: Average Strouhal number (St_c^*) of the reduced sections in Figure 4.7 against the length of the flaplet normalised with the chord length.

work where flaplets were attached on to the main body of an aerofoil to mimic 'pop-up' feathers (Brücker and Weidner, 2014). Those flaplets were more akin to pop-up feathers whereas the fringes at the trailing edge of the feather are quite narrow in relation to the feather as a whole. But are very flexible such that they are compliant within the flow. The abstract nature of the flaplets used here allows them to be easily modelled, whereby they are cantilevered beams so the response is well documented and as such the frequency of the oscillation can be easily tuned. If they were made more like the fringes of the feathers, i.e. similar to the brush-type extension in Herr and Dobrzynski (2005), then the modelling of the elements would be more difficult due to the mechanical interaction between each element.

4.5.7.2 What would happen if the flaplets were other geometries?

This question has two trains of thought depending on if we are looking at the aeroacoustics or the aerodynamics. From the acoustics side, it was seen that with the carbon fibre flaplets, the oscillatory behaviour does not effect the low frequency noise reduction, as such they act as slitted serrations (Woodhead et al., 2019). Therefore, it could be said that if the flaplets were in a sawtooth geometry, the results would be different and would yield similar results to the previous work on serrations. However, when concerning the fluid dynamics effect, if again we suppose they in a flexible sawtooth configuration, then we might see a similar stabilising effect as seen in §2 as they are still flexible cantilevered

elements from protruding from the trailing edge. But, how much of an effect would be difficult to say as the response is now more complex as the cross-sectional area changes in the chordwise dimension. So equation (2.1), which describes the frequency of the flaplets, could then no longer be applied in its current form. This work on flexible sawtooth serrations would be a very interesting extension of this project.

4.5.7.3 Are the tested Reynolds numbers representative?

The Reynolds numbers used throughout this work are typical small UAV drone or high altitude drone Reynolds numbers. Here practical limitations stopped us from reaching higher Reynolds numbers. In the PIV study the limitations was the need to achieve time resolved PIV therefore we could only go up to $Re_c = 150,000$ with the current camera / laser arrangement. For the acoustic study we did go up to much higher Re_c ($Re_c = 900,000$). However, we could not go higher as we were already close to the velocity limit of the wind tunnel. There were also practical limitations of the flaplets themselves. Where the flaplets went into resonance (flutter) at the highest tested Re_c, limiting any acoustic benefit. Saying this, a study with an actively controlled trailing edge, which oscillated at similar frequencies and amplitudes as our passive one, (Simiriotis et al., 2019) showed promising fluid dynamic results at higher Reynolds number than were test here. They tested on at a Reynolds number of 1 million and an angle of incidence of 10°, which corresponds to typical airliner take-off / landing conditions. Therefore it is reasonable to suggest that our passive flaplets would have benefits at higher Reynolds numbers also, given that flutter would not be an issue.

4.5.7.4 What if flexible strings were used instead of flaplets?

Long flexible strings have been investigated in previous studies (He, Guo and Wang, 2019). These studies are typically carried out at much lower Reynolds numbers than used here ($Re_c \sim 10,000-40,000$) and are almost always carried out in a water tunnel. By using a water tunnel, higher viscous forces within water, help to suppress the flexible string from going into flutter. So if flexible strings were to be used in a wind tunnel, with similar Re_c used for this study they would almost certainly be in a state of flutter. This would be extremely detrimental for the acoustics, as was seen with the long flaplets in Fig. 4.6.

4.5.7.5 Would the flaplets be able to prevent stall?

It has been shown that flaplets, when placed at the 0.8c position (Brücker and Weidner, 2014), act as 'pop-up' feathers and delay the onset of stall in a ramp up motion. Therefore it is a reasonable assumption that the flaplets attached to the trailing edge will also delay the onset of stall in a similar ramp up motion. However once the aerofoil is in stall it is expected that the flaplets will have little to no effect.

4.5.8 Future work

For future work, an aerofoil with retractable flaplets that have the ability to be dynamically monitored should be investigated. By having the retractable flaplets, the frequency reduction range can be tweaked on-the-fly and can be stored internally within the aerofoil if no flaplets are required. This coupled with the flaplets being piezoelectic, as was discussed in 2.5.8

Piezoelectic flaplets could be used to detect when flaplets might go into flutter by detecting the presence of the torsional mode or the 2^{nd} bending mode. If it is then seen that this mode is increasing then the flaplets can then be retracted, by a little or entirely, such that damage is not done to the flaplets and the acoustic performance is maintained. Alternatively, one can think of mechanical modifications of the flaplets that allow only bending in one plane, so that any torsional bending is prevented, even if flutter occurs. Further investigations should be carried out to look at whether flutter can be detected by looking at the spectra just prior to flutter to see if there is a significant change in frequency shift or if there is another indicator; such as an increase in the RMS of the raw flaplet signal.

Other work including simultaneous PIV-acoustic measurements should be taken to really diagnose where this low frequency reduction is from, and how it can be harnessed with retractable flaplets. This type of simultaneous measurement campaign has been carried out by Pröbsting, Serpieri and Scarano (2014) on trailing-edge serrations.

5 Conclusion

Contents

5.1 Conclusion **139**
5.2 Thesis novelty **140**
5.3 New literature **141**
5.4 Future Work **142**

5.1 Conclusion

The research has seen that trailing edge flaplets can have a positive effect on the aerodynamics and the aeroacoustics of a symmetric aerofoil. The first experiment was a time resolved PIV experiment focusing on the effect the flaplets have on the shear layer on the aft part of an aerofoil. The second and third experiments were acoustic experiments looking; firstly at what effect flaplets had on the acoustics and secondly looking at how the geometry of the flaplets can be optimised and what effect different parameters have.

The three studies carried out have shown the benefits of attaching this type of oscillator to the trailing edge of an aerofoil. When looking at the aerodynamics, they have shown to stabilise the shear-layer by dampening out the non-linear instabilities in the boundary layer which ultimately leads to a reduced boundary layer thickness and a

reduction in drag. Concerning the aeroacoustics, a low frequency noise reduction has been found and scales with the Strouhal number. The Strouhal number range which is reduced can be altered by tuning the flaplet length, where a higher Strouhal range can be targeted with shorter flaplets and vice-versa with long flaplets. The magnitude of this reduction can be increased with a larger width and small inter-spacing. However, with all flaplets there was an increase at higher frequencies, and here it was determined that the best way to mitigate this effect was with smaller width flaplets. All flaplets had an effect on the tonal noise of the aerofoil, whereby the magnitude was lower and delayed to a higher Reynolds number. The reduction in noise level is attributed to a slight delay in the separation bubble which was seen with a flow visualisation on the pressure side of the aerofoil.

5.2 Thesis novelty

This thesis comprises of a simple and novel trailing edge modification. It is the first study where passive oscillators have been attached to the trailing edge of an aerofoil and extensively investigated. A preliminary acoustic study was carried out by Kamps et al. (2017) with this type of oscillator, however this was a very brief overview. Therefore this was the start point. This work is the first fluid dynamical study and the first extensive aeroacoustic study looking at the effect of passive flexible oscillators attached to trailing edge of an aerofoil. This work is the first fluid dynamical study and the first extensive aeroacoustic study looking at the effect of passive flexible oscillators attached to trailing edge. Previous work has only focused on them being attached to the main body of the aerofoil (Brücker and Weidner, 2014; Rosti et al., 2017) and on the aft half of a cylinder (Geyer et al., 2019). Other works with similar trailing edge modifications have been active, whereby the oscillation of the trailing edge was controlled. Here the novelty is in the simplicity of how we can produce similar frequency and oscillation amplitude, by using such a simple and easily implementable solution. In addition, the proposed design of such pacemakers as deployable flaps from a slit in the trailing edge makes it an attractive feature of tunable oscillators, which allow tailored use for different flight situations such as take-off and landing in the whole envelope of flight mission.

5.3 New literature

Since the publication of the papers included herein, other authors have published new work. The first new work was a 2-D numerical simulation by Yu and Yang (2020). They used a S833 aerofoil equipped with, what they call, flapping trailing edge fringes (i.e. flaplets). Here they were primarily looking at the effect of the flaplet length and frequency on the lift and drag coefficient and the effect on the shed vortices. It should be mentioned here that, the flapping frequency was altered manually and not by altering the length or material properties. They found that if the flapping frequency was less than the shedding frequency, the vortices being shed were 'slowed down' due to the disruption of the fringe. This resulted in the reduction in the vorticity and the vortices were more easily dissipated. On the other hand, if the shedding frequency was higher than the vortex shedding frequency, they were either enhanced or maintained. This was due to the flaplets locking-in with the shed vortices, where the size of the vortices were reduced. Hence, the wake was then reduced leading to a reduction in drag. The Reynolds number that was used was much lower than the ones used in our study, $Re_c = 40,000$. But the fluid mechanics are predominantly the same; the flaplets, as long as the Eigen frequency of them is tuned correctly, can reduce the drag of an aerofoil.

The next publication is by Abdessemed, Bouferrouk and Yao (2021) where they looked at a harmonically oscillating trailing edge. This study was also a CFD simulation using a dynamic mesh to allow for the oscillating trailing edge. The aerofoil used was a NACA0012 at a Reynolds number = 620,000 and were looking at both the aerodynamic and aeroacoustic effects. When looking at the aerodynamic effects, in a similar way to Yu and Yang (2020), they saw a reduction in drag and this was attributed here to a modification in the wake structure. They found that the main tonal noise was modified by the harmonic motion, where it was reduced in magnitude and the frequency of it was also shifted.

5.4 Future Work

Future works has been discussed in each of the chapters however here the list is more focused:

- Piezoelectic flaplets - these have a twofold benefit, the first is for energy harvesting and the second is for live flaplet monitoring/tracking.
- Retractable flaplets - these would be such that the length could be altered 'on the fly' given the flight conditions. This means that different low frequencies / Strouhal number bands can be targeted as and when required, it also means that they can also be retracted all the way if needed.
- Additional measurements - an additional PIV campaign, focusing at the wake of the aerofoil to see the wake modification seen in other publications with a similar trailing edge modifications. This campaign could also be a simultaneous PIV-acoustic campaign to fully understand the mechanism behind the low frequency noise reduction. A final measurement campaign focusing on the lift/drag measurements across various angles of attack, leading to a more complete understanding of the flaplets on the key aerodynamic quantities.

Appendices

A

Uncertainty analysis

Contents

A.1 Hot wire anemometery 145
A.2 Force balance 147
A.3 Microphone array 148

A.1 Hot wire anemometery

The hot wire anemometer is a probe which is used to convert voltage to velocity, through heat transfer. The calibration of such a probe was explained in detail in §3.5.3.2 and here the uncertainties that are introduced through the calibration process will be detailed. There are three main areas in which uncertainty can be introduced, according to Jørgensen (2002); 1) instrumentation, 2) calibration equipment and 3) environmental conditions.

Jørgensen (2002) notes that commercially available probes, such as the one used in this study, have very little drift over time and as such the uncertainty pertaining to the probe itself will be very low and negligible.

For the uncertainties introduced within the calibration, there are many places this can be introduced. First is from the calibration device itself, i.e. the vane anemometer.

The vane anemometer was used in preference to the pitot static tube of the tunnel as the pitot tube, generally, has more associated uncertainty attached. These are from the atmospheric pressure reading, air density calculation and ambient temperature reading. Whereas the the vane anemometer is a calibrated piece of equipment which can give velocity as an output straightaway. For the vane anemometer used the uncertainty was $\Delta E_{U_\infty} = 0.05$ m/s. Secondly, the uncertainty introduced by the conversion and the linearisation of the voltage to velocity, using a curve fitting algorithm needs to be accounted for. Here, to work out the uncertainty the difference between set reference velocity and the velocity from the curve fit is calculated, as per equation (A.1).

$$\Delta E_{\text{lin}} = U_{\text{ref.}} - U_{\text{curve}} \tag{A.1}$$

When looking at the uncertainties introduced by the data acquisition system (DAQ), the resolution of the analogue to digital conversion should be investigated. For the current study the DAQ was a 24-bit National Instruments board, that runs off ±10 V. To work out this uncertainty, equation (A.2) is used.

$$\Delta E_{\text{res.}} = \frac{1}{U_{ref.}} \cdot \frac{V_{AD}}{2^n} \cdot \frac{\partial U}{\partial V} \tag{A.2}$$

where V_{AD} is the input voltage range, n is the resolution in bits, $U_{\text{ref.}}$ is the reference velocity and $\partial U/\partial V$ is the sensitivity of the system (i.e. the slope in Fig. 3.12).

For the uncertainty of the experimental conditions, the uncertainty in the orientation of the probe should be considered. This orientation is related to the how well aligned the probe is to the flow, in general this orientation can be positioned with an accuracy of $\theta = 1^\circ$ (Jørgensen, 2002). However, here I have allowed for a slightly higher value due to the difficulty of aligning the probe normal to the flow; $\theta = 3^\circ$. The equation to calculate the uncertainty can be seen in equation (A.3)

$$\Delta E_{\text{pos.}} = 1 - \cos(\theta) \tag{A.3}$$

Another source of uncertainty can be the temperature variation during the experiment. However to mitigate these effects, a thermocouple was used in conjunction to the HWA probe. The temperature corrections were then carried out automatically within the data capturing software, as such they will have a little effect on the results.

Uncertainty Source	ΔE_i
ΔE_{U_∞}	0.050 m/s
$\Delta E_{\text{lin.}}$	0.030 m/s
$\Delta E_{\text{res.}}$	$4.64\text{x}10^{-7}$ m/s
$\Delta E_{\text{pos.}}$	$1.37\text{x}10^{-3}$ m/s
$\Delta E_{\text{HWA, total}}$	0.058 m/s

Table A.1: Hot wire anemometery uncertainty, where the input data are; U = 19.7 m/s, V = 10 V, n = 24 bit, $\partial U/\partial V$ = 15.35 ms^{-1}/V and $\theta = 3°$.

Summing up all the uncertainties for the HWA, shows that the main overall uncertainty at a velocity of U_∞ = 19.7 m/s was ±0.058 m/s. This velocity was chosen as this is a calibration point that is close to the velocity of the presented wake profiles and turbulence spectra in §3. A summary of the uncertainties can be seen in Table A.1.

A.2 Force balance

When looking at the uncertainty of the force balance, the majority of this would come from the calibration of the system. The way the force balance works is by having six strain gauges positioned such that the three forces (lift, drag and side) and the three moments (yaw, roll and pitch) can be resolved. Where the forces/moments (**F**), can be found by solving the matrix **A** with the input voltages (**V**) from the six strain gauges, as seen in (A.5).

$$\mathbf{F} = \mathbf{A} \cdot \mathbf{V} \tag{A.4}$$

$$\begin{bmatrix} F_L \\ F_D \\ F_S \\ M_P \\ M_R \\ M_Y \end{bmatrix} = \mathbf{A} \cdot \begin{bmatrix} v_1 \\ v_2 \\ v_3 \\ v_4 \\ v_5 \\ v_6 \end{bmatrix} \tag{A.5}$$

Therefore it can be seen that **A** will be a 6x6 matrix, as such there will need to be 36 coefficients that need to be resolved before equating the measured voltages to measured forces/moments. The equation for each of the forces/moments will take the form:

$$F_1 = A_{1,1}v_1 + A_{1,2}v_2 + A_{1,3}v_3 + A_{1,4}v_4 + A_{1,5}v_5 + A_{1,6}v_6 \tag{A.6}$$

Uncertainty Source	ΔE_i
ΔE_M	$0.5\text{x}10^{-3}$ kg
ΔE_H	$0.5\text{x}10^{-3}$ m
$\Delta E_{A_{n,m}}$	$0.707\text{x}10^{-3}$ kg m
ΔE_{F_n}	$1.73\text{x}10^{-3}$

Table A.2: Force balance calibration uncertainty.

During the calibration procedure, explained in §3.5.3.3, 36 measurements are taken using weights at different heights and orientation. Therefore each of the coefficients will have an uncertainty related to the weight and height of the known applied force. So the uncertainty associated to the coefficients of A will be,

$$\Delta E_{A_{n,m}} = \sqrt{\Delta E_M^2 + \Delta E_H^2} \tag{A.7}$$

where ΔE_M is the uncertainty in the added mass and ΔE_H is the uncertainty in the height. Once the uncertainty is calculated for all the $A_{n,m}$, the overall uncertainty for each force/moment must be the sum of six lots of the uncertainty. Hence the total uncertainty for each for is 0.173%, as seen in table A.2.

A.3 Microphone array

The uncertainty from the microphone measurements comes from the calibration of the microphones. Therefore the calibrator should be investigated to see what effect the accuracy of this would have on the microphone measurements. From the manufacturers specification of the PCE-SC 41, the accuracy of the noise source generated by the calibrator was 94 ± 0.3 dB and the frequency was f = 1 kHz ±0.1%. The manufacturers also reported that the environmental conditions can effect emitted noise of the calibrator. The first condition that effects the calibrator is a change in atmospheric pressure, where there is a drift of ±0.1 dB per 50 mmHg (6.66 kPa). Therefore when looking at how the pressure drifted throughout the experimental campaign, the maximum atmospheric pressure was 99.88 kPa and the minimum was 98.97 kPa, as such the drift was 0.91 kPa (6.83 mmHg). Leading to an uncertainty of $\Delta E_{\text{P,atm}} = 0.014$ dB. So the atmospheric pressure changed observed will have a very minor effect on the calibration.

Uncertainty Source	ΔE_i
$\Delta E_{\text{cal.}}$	0.300 dB
$\Delta E_{\text{P,atm.}}$	0.014 dB
$\Delta E_{\text{temp.}}$	0.047 dB
$\Delta E_{\text{AC, total}}$	0.304 dB

Table A.3: Microphone calibration uncertainty.

The other effect is due to the temperature of the air, where the reported temperature drift is 0.01 dB/°C. During the experiments the maximum temperature observed was 28.2°C and the minimum was 23.5°C, so a temperature drift of 4.7°C. Leading to an uncertainty caused by the temperature of $\Delta E_{\text{temp.}} = 0.047$ dB.

Therefore the total uncertainty, taking into account the environmental and calibrator uncertainty effects is $\Delta E_{\text{AC, total}} \pm 0.304$ dB.

References

[1] Abdessemed, C., Bouferrouk, A. and Yao, Y. 'Aerodynamic and Aeroacoustic Analysis of a Harmonically Morphing Airfoil Using Dynamic Meshing'. In: *Acoustics* 3.1 (Mar. 2021), pp. 177–199.

[2] Allen, C. S. et al. *Aeroacoustic Measurements*. Ed. by Mueller, T. J. Vol. 53. 9. Berlin, Heidelberg: Springer Berlin Heidelberg, 2002, pp. 1689–1699. eprint: 978-3-662-05058-3 (10.1007).

[3] Arbey, H. and Bataille, J. 'Noise generated by airfoil profiles placed in a uniform laminar flow'. In: *J. Fluid Mech.* 134.-1 (Sept. 1983), p. 33.

[4] Arce León, C. et al. 'Effect of trailing edge serration-flow misalignment on airfoil noise emissions'. In: *J. Sound Vib.* 405 (Sept. 2017), pp. 19–33.

[5] Arce León, C. et al. 'Acoustic Emissions of Semi-Permeable Trailing Edge Serrations'. In: *Acoust. Aust.* 46.1 (Apr. 2018), pp. 111–117.

[6] Arcondoulis, E. et al. 'Airfoil dual acoustic feedback mechanisms at low-to-moderate Reynolds number'. In: *2018 AIAA/CEAS Aeroacoustics Conf.* Reston, Virginia: American Institute of Aeronautics and Astronautics, June 2018.

[7] Arcondoulis, E. et al. 'An investigation of airfoil dual acoustic feedback mechanisms at low-to-moderate Reynolds number'. In: *J. Sound Vib.* 460 (Nov. 2019), p. 114887.

[8] Atkin, C. 'Convergence of calculated transition loci during computational analysis of transonic aerofoils and infinite swept wings'. In: *29th Congr. Int. Counc. Aeronaut. Sci.* St. Petersburg, Russia, Sept. 2014.

[9] Bhushan, B. In: *Encyclopedia of Nanotechnology*. Ed. by Bhushan, B. Dordrecht: Springer Netherlands, 2012, pp. 2400–2411.

[10] Boutilier, M. S. and Yarusevych, S. 'Parametric study of separation and transition characteristics over an airfoil at low Reynolds numbers'. In: *Exp. Fluids* 52.6 (2012), pp. 1491–1506.

[11] Brooks, T. F. and Humphreys, W. M. 'A deconvolution approach for the mapping of acoustic sources (DAMAS) determined from phased microphone arrays'. In: *J. Sound Vib.* 294.4-5 (July 2006), pp. 856–879.

[12] Brooks, T. F., Marcolini, M. A. and Pope, D. S. 'Airfoil trailing edge flow measurements and comparison with theory, incorporating open wind tunnel corrections'. In: *9th Aeroacoustics Conf.* Reston, Virigina: American Institute of Aeronautics and Astronautics, Oct. 1984.

[13] Brooks, T. F., Marcolini, M. A. and Pope, D. S. 'Airfoil trailing-edge flow measurements'. In: *AIAA J.* 24.8 (Aug. 1986), pp. 1245–1251.

[14] Brooks, T. F., Pope, D. S. and Marcolini, M. A. 'Airfoil Self-Noise and Prediction'. In: *NASA Ref. Publ. 1218* (1989), pp. 1–142.

[15] Brücker, C. and Weidner, C. 'Influence of self-adaptive hairy flaps on the stall delay of an airfoil in ramp-up motion'. In: *J. Fluids Struct.* 47 (2014), pp. 31–40.

[16] Carruthers, A. C., Thomas, A. L. R. and Taylor, G. K. 'Automatic aeroelastic devices in the wings of a steppe eagle Aquila nipalensis'. In: *J. Exp. Biol.* 210.23 (2007), pp. 4136–4149.

[17] Chong, T. P. and Joseph, P. 'An experimental study of airfoil instability tonal noise with trailing edge serrations'. In: *J. Sound Vib.* 332.24 (2013), pp. 6335–6358.

[18] Chong, T. P., Joseph, P. and Gruber, M. 'An Experimental Study of Airfoil Instability Noise with Trailing Edge Serrations'. In: *16th AIAA/CEAS Aeroacoustics Conf.* Vol. 332. 24. Reston, Virigina: American Institute of Aeronautics and Astronautics, June 2010, pp. 6335–6358.

[19] Chong, T. P., Joseph, P. and Gruber, M. 'Airfoil self noise reduction by non-flat plate type trailing edge serrations'. In: *Appl. Acoust.* 74.4 (Apr. 2013), pp. 607–613.

[20] Chong, T. P., Joseph, P. and Kingan, M. J. 'An investigation of airfoil tonal noise at different Reynolds numbers and angles of attack'. In: *Appl. Acoust.* 74.1 (2013), pp. 38–48.

[21] Cummins, C. et al. 'A separated vortex ring underlies the flight of the dandelion'. In: *Nature* 562.7727 (Oct. 2018), pp. 414–418.

[22] Das, C. et al. 'An experimental investigation of flow-induced noise mechanism of a flexible flat-plate trailing-edge'. In: *Annu. Conf. Aust. Acoust. Soc.* 5.1 (2015), pp. 1–10.

[23] Desquesnes, G., Terracol, M. and Sagaut, P. 'Numerical investigation of the tone noise mechanism over laminar airfoils'. In: *J. Fluid Mech.* 591 (Nov. 2007), pp. 155–182.

[24] Dong, S. et al. 'A combined direct numerical simulation-particle image velocimetry study of the turbulent near wake'. In: *J. Fluid Mech.* 569 (2006), pp. 185–207.

[25] Dovgal, A. V., Kozlov, V. V. and Michalke, A. 'Laminar boundary layer separation: Instability and associated phenomena'. In: *Prog. Aerosp. Sci.* 30.1 (1994), pp. 61–94.

[26] Finez, A. et al. 'Broadband noise reduction with trailing edge brushes'. In: *Proc. 16th AIAA/CEAS aeroacoustics Conf.* (2010), pp. 1–13.

[27] Geyer, T. F., Sarradj, E. and Fritzsche, C. 'Measurement of the noise generation at the trailing edge of porous airfoils'. In: *Exp. Fluids* 48.2 (Feb. 2010), pp. 291–308.

[28] Geyer, T. F. and Sarradj, E. 'Self Noise Reduction and Aerodynamics of Airfoils With Porous Trailing Edges'. In: *Acoustics* 1.2 (Apr. 2019), pp. 393–409.

[29] Geyer, T. F. et al. 'Experimental Investigation of Leading Edge Hook Structures for Wind Turbine Noise Reduction'. In: *22nd AIAA/CEAS Aeroacoustics Conf.* (2016), pp. 1–13.

[30] Geyer, T. F. et al. 'Passive Control of the Vortex Shedding Noise of a Cylinder at Low Reynolds Numbers Using Flexible Flaps'. In: *23rd AIAA/CEAS Aeroacoustics Conf.* (2017), pp. 1–11.

[31] Geyer, T. F. et al. 'Silent owl flight: The effect of the leading edge comb'. In: *Int. J. Aeroacoustics* 16.3 (Apr. 2017), pp. 115–134.

[32] Geyer, T. F. et al. 'Vortex Shedding and Modal Behavior of a Circular Cylinder Equipped with Flexible Flaps'. In: *Acta Acust. united with Acust.* 105.1 (Jan. 2019), pp. 210–219.

[33] Graham, R. 'The silent flight of owls'. In: *Aeronaut. J.* 38.286 (1934), pp. 837–843.

[34] Gruber, M., Azarpeyvand, M. and Joseph, P. 'Airfoil trailing edge noise reduction by the introduction of sawtooth and slitted trailing edge geometries'. In: *Proc. 20th Int. Congr. Acoust. ICA* 10.August (2010), pp. 1–9.

[35] He, X., Guo, Q. and Wang, J. 'Extended flexible trailing-edge on the flow structures of an airfoil at high angle of attack'. In: *Experiments in Fluids* 60.8 (2019), pp. 1–22.

[36] Herr, M. 'Design Criteria for Low-Noise Trailing-Edges'. In: *13th AIAA/CEAS Aeroacoustics Conf. (28th AIAA Aeroacoustics Conf.* (2007), pp. 1–14.

[37] Herr, M. and Dobrzynski, W. 'Experimental Investigations in Low-Noise Trailing Edge Design.' In: *AIAA J.* 43.6 (June 2005), pp. 1167–1175.

[38] Ho, C.-M. and Huang, L.-S. 'Subharmonics and vortex merging in mixing layers'. In: *J. Fluid Mech.* 119 (1982), pp. 443–473.

[39] Horton, H. P. and Stock, H.-W. 'Computation of compressible, laminar boundary layers on swept, tapered wings'. In: *J. Aircr.* 32.6 (Nov. 1995), pp. 1402–1405.

[40] Howe, M. 'Aerodynamic noise of a serrated trailing edge'. In: *J. Fluids Struct.* 5.1 (Jan. 1991), pp. 33–45.

[41] Huang, R. and Lin, C. 'Vortex shedding and shear-layer instability of a cantilever wing at low reynolds numbers'. In: *33rd Aerosp. Sci. Meet. Exhib.* 33.8 (1995), pp. 1398–1403.

[42] Inasawa, A., Ninomiya, C. and Asai, M. 'Suppression of Tonal Trailing-Edge Noise From an Airfoil Using a Plasma Actuator'. In: *AIAA J.* 51.7 (2013), pp. 1695–1702.

[43] Jaworski, J. W. and Peake, N. 'Aerodynamic noise from a poroelastic edge with implications for the silent flight of owls'. In: *J. Fluid Mech.* 723 (2013), pp. 456–479.

[44] Jaworski, J. W. and Peake, N. 'Aeroacoustics of Silent Owl Flight'. In: *Annu. Rev. Fluid Mech.* 52.1 (2020), pp. 395–420.

[45] Jodin, G. et al. 'Dynamics of a hybrid morphing wing with active open loop vibrating trailing edge by time-resolved PIV and force measures'. In: *J. Fluids Struct.* 74 (2017), pp. 263–290.

[46] Jodin, G. et al. 'Electroactive morphing vibrating trailing edge of a cambered wing : PIV , turbulence manipulation and velocity effects'. In: *IUTAM Symp. Crit. flow Dyn. Involv. moving/deformable Struct. with Des. Appl.* Santorini, Greece, 2018.

[47] Jørgensen, F. *How to measure turbulence with hot-wire anemometers - a practical guide.* Skovlunde: Dantec Dynamics, 2002, p. 73.

[48] Kamps, L. et al. 'Vortex shedding noise of a cylinder with hairy flaps'. In: *J. Sound Vib.* 388 (2016), pp. 69–84.

[49] Kamps, L. et al. 'Airfoil self noise reduction at low reynolds numbers using a passive flexible trailing edge'. In: *23rd AIAA/CEAS Aeroacoustics Conf. 2017.* June. Reston, Virginia: American Institute of Aeronautics and Astronautics, June 2017, pp. 1–10.

[50] Kunze, S. and Brücker, C. 'Control of vortex shedding on a circular cylinder using self-adaptive hairy-flaps'. In: *Comptes Rendus - Mec.* 340.1-2 (2012), pp. 41–56.

[51] Lilley, G. M. 'A Study of the Silent Flight of the Owl'. In: *4th AIAA/CEAS Aeroacoustics Conf.* 1998, pp. 1–6.

[52] Lowson, M., Fiddes, S. and Nash, E. 'Laminar boundary layer aero-acoustic instabilities'. In: *32nd Aerosp. Sci. Meet. Exhib.* Reston, Virigina: American Institute of Aeronautics and Astronautics, Jan. 1994.

[53] McAlpine, A., Nash, E. and Lowson, M. 'On the Generation of Discrete Frequency Tones by the Flow around an Aerofoil'. In: *J. Sound Vib.* 222.5 (May 1999), pp. 753–779.

[54] Merino-Martínez, R. et al. *A review of acoustic imaging methods using phased microphone arrays: Part of the "Aircraft Noise Generation and Assessment" Special Issue.* Vol. 10. 1. Springer Vienna, 2019, pp. 197–230.

[55] Meyer, K. E., Cavar, D. and Pedersen, J. M. 'POD as tool for comparison of PIV and LES data'. In: *7th Int. Symp. Part. Image Velocim.* (2007), pp. 1–12.

[56] Miklosovic, D. S. et al. 'Leading-edge tubercles delay stall on humpback whale (Megaptera novaeangliae) flippers'. In: *Phys. Fluids* 16.5 (May 2004), pp. L39–L42.

[57] Moreau, S. et al. 'Analysis of Flow Conditions in Freejet Experiments for Studying Airfoil Self-Noise'. In: *AIAA J.* 41.10 (Oct. 2003), pp. 1895–1905.

[58] Moriarty, P. 'NAFNoise User ' s Guide'. In: (2005).

[59] Muthuramalingam, M. et al. 'Flow turning effect and laminar control by the 3D curvature of leading edge serrations from owl wing'. In: *Bioinspiration & Biomimetics* 16.2 (Dec. 2020), p. 026010.

[60] Oerlemans, S. et al. 'Reduction of Wind Turbine Noise Using Optimized Airfoils and Trailing-Edge Serrations'. In: *AIAA J.* 47.6 (June 2009), pp. 1470–1481.

[61] Osterberg, N. and Albertani, R. 'Investigation of self-deploying high-lift effectors applied to membrane wings'. In: *Aeronaut. J.* 121.1239 (2017), pp. 660–679.

[62] Paterson, R. W. et al. 'Vortex Noise of Isolated Airfoils'. In: *NACA Adv. Restricted Rept. 3G29 J. Aeronaut. Sci. J. Aircr. Low Adv. Ration J. Am. Helicopter Soci-ety J. Aircr.* 17.5 (1972), pp. 3–12.

[63] Perret, L. 'PIV investigation of the shear layer vortices in the near wake of a circular cylinder'. In: *Exp. Fluids* 47.4-5 (2009), pp. 789–800.

[64] Ponitz, B. et al. 'Diving-flight aerodynamics of a peregrine falcon (Falco peregrinus)'. In: *PLoS One* 9.2 (2014).

[65] Prasad, A. and Williamson, C. H. K. 'The instability of the shear layer separating from a bluff body'. In: *J. Fluid Mech.* 333 (1997), S0022112096004326.

[66] Pröbsting, S., Scarano, F. and Morris, S. C. 'Regimes of tonal noise on an airfoil at moderate Reynolds number'. In: *J. Fluid Mech.* 780 (2015), pp. 407–438.

[67] Pröbsting, S., Serpieri, J. and Scarano, F. 'Experimental investigation of aerofoil tonal noise generation'. In: *J. Fluid Mech.* 747.2 (May 2014), pp. 656–687.

[68] Raffel, M., Willert, C. E. and Kompenhans, J. *Particle Image Velocimetry.* Springer Berlin Heidelberg, 1998.

[69] Rajagopalan, S. and Antonia, R. A. 'Flow around a circular cylinder-structure of the near wake shear layer'. In: *Exp. Fluids* 38.4 (2005), pp. 393–402.

[70] Rodríguez, I. et al. 'Direct numerical simulation of a NACA0012 in full stall'. In: *Int. J. Heat Fluid Flow* 43 (2013), pp. 194–203.

[71] Rosti, M. E. et al. 'The PELskin project-part V: towards the control of the flow around aerofoils at high angle of attack using a self-activated deployable flap'. In: *Meccanica* 52.8 (2017), pp. 1811–1824.

[72] Sarradj, E. 'A fast signal subspace approach for the determination of absolute levels from phased microphone array measurements'. In: *J. Sound Vib.* 329.9 (2010), pp. 1553–1569.

[73] Sarradj, E. 'A fast ray casting method for sound refraction at shear layers'. In: *Int. J. Aeroacoustics* 16.1-2 (2017), pp. 65–77.

[74] Sarradj, E. et al. 'Acoustic and aerodynamic design and characterization of a small-scale aeroacoustic wind tunnel'. In: *Appl. Acoust.* 70.8 (2009), pp. 1073–1080.

[75] Sataloff, R. T., Johns, M. M. and Kost, K. M. *Handbook of Experimental Fluid Mechanics*. Ed. by Tropea, C., Yarin, A. L. and Foss, J. F. Berlin, Heidelberg: Springer Berlin Heidelberg, 2007.

[76] Schlanderer, S. C. and Sandberg, R. D. 'DNS of a Compliant Trailing-Edge Flow'. In: *19th AIAA/CEAS Aeroacoustics Conf.* Reston, Virginia: American Institute of Aeronautics and Astronautics, May 2013, pp. 1–18.

[77] Schluter, J. U. 'Lift Enhancement at Low Reynolds Numbers Using Self-Activated Movable Flaps'. In: *J. Aircr.* 47.1 (2010), pp. 348–351.

[78] Semeraro, O., Bellani, G. and Lundell, F. 'Analysis of time-resolved PIV measurements of a confined turbulent jet using POD and Koopman modes'. In: *Exp. Fluids* 53.5 (2012), pp. 1203–1220.

[79] Sijtsma, P. 'CLEAN Based on Spatial Source Coherence'. In: *Int. J. Aeroacoustics* 6.4 (2007), pp. 357–374.

[80] Simiriotis, N. et al. 'Morphing of a supercritical wing by means of trailing edge deformation and vibration at high Reynolds numbers: Experimental and numerical investigation'. In: *J. Fluids Struct.* 91 (Nov. 2019), p. 102676.

[81] Stanek, F. J. *Free and Forced Vibrations of Cantilever Beams With Viscous Damping*. Tech. rep. June. Washington DC: National Aeronautics and Space Administration, 1965.

[82] Talboys, E. and Brücker, C. 'Upstream shear-layer stabilisation via self-oscillating trailing edge flaplets'. In: *Exp. Fluids* 59.10 (Oct. 2018), p. 145.

[83] Talboys, E., Geyer, T. F. and Brücker, C. 'The Aerodynamic And Aeroacoustic Effect Of Passive High Frequency Oscillating Trailing Edge Flaplets'. In: *IUTAM Symp. Crit. flow Dyn. Involv. moving/deformable Struct. with Des. Appl.* Santorini, Greece, 2018.

[84] Talboys, E., Geyer, T. F. and Brücker, C. 'An aeroacoustic investigation into the effect of self-oscillating trailing edge flaplets'. In: *J. Fluids Struct.* (Feb. 2019), pp. 1–13.

[85] Talboys, E., Geyer, T. F. and Brücker, C. 'Influence of self-oscillating trailing edge flaplets on turbulent boundary layer – trailing edge noise .' In: *23rd Int. Congr. Acoust.* Aachen, 2019.

[86] Talboys, E. et al. 'A parametric study of the effect of self-oscillating trailing-edge flaplets on aerofoil self-noise'. In: *Appl. Acoust.* 177 (June 2021), p. 107907.

[87] Tam, C. K. W. 'Discrete tones of isolated airfoils'. In: *J. Acoust. Soc. Am.* 55.6 (June 1974), pp. 1173–1177.

[88] Thomareis, N. and Papadakis, G. 'Effect of trailing edge shape on the separated flow characteristics around an airfoil at low Reynolds number: A numerical study'. In: *Phys. Fluids* 29.1 (Jan. 2017), p. 014101.

[89] Welch, P. 'The use of fast Fourier transform for the estimation of power spectra: A method based on time averaging over short, modified periodograms'. In: *IEEE Trans. Audio Electroacoust.* 15.2 (June 1967), pp. 70–73.

[90] Woodhead, P. C. et al. 'On the Double-Rooted Trailing Edge Serration'. In: *25th AIAA/CEAS Aeroacoustics Conference*. 2019.

[91] Xin, Z. et al. 'Flutter frequency based on bending - torsion coupling theory'. In: *8th Int. Conf. Comput. Methods*. Guilin, Guangxi, China, 2017.

[92] Yarusevych, S., Sullivan, P. E. and Kawall, J. G. 'On vortex shedding from an airfoil in low-Reynolds-number flows'. In: *J. Fluid Mech.* 632 (2009), p. 245.

[93] Yu, H. and Yang, Z. 'A Numerical Simulation on the Airfoil S833 Equipped with Flapping Trailing Edge Fringes'. In: *J. Appl. Fluid Mech.* 13.2 (Mar. 2020), pp. 571–582.